ANALYTICAL AND NUMERICAL INVESTIGATION OF AN AIR ENTRAINING HYDRAULIC JUMP

A DISSERTATION
SUBMITTED TO THE FACULTY OF
UNIVERSITY OF MINNESOTA
BY

ADAM MATTHEW WITT

IN PARTIAL FULFILLMENT OF THE REQUIREMENTS
FOR THE DEGREE OF
DOCTOR OF PHILOSOPHY

DR. JOHN S. GULLIVER, Adviser
DR. LIAN SHEN, Adviser

October 2014

Acknowledgements

This dissertation represents the combined efforts of numerous individuals who deserve acknowledgement.

I am eternally grateful for the guidance, support, and advice of my advisor Dr. John Gulliver. Through uncommon personal effort and dedication, Dr. Gulliver devoted himself to my advancement, and to the completion of this dissertation. His commitment to my education has been inspiring and humbling.

The insights and direction from my advisor Dr. Lian Shen were pivotal in shaping this dissertation, and to him I express my utmost appreciation. My intellectual growth would not have been possible without his attentive and persistent leadership.

I owe a debt of gratitude to the U.S. Department of Energy and its Office of Energy Efficiency and Renewable Energy Water Power Program, who funded this dissertation through a graduate research fellowship awarded and managed by the Hydro Research Foundation. The professional guidance and personal advocacy from Deborah Linke and Brenna Vaughn are especially noteworthy. I am tremendously thankful for the opportunities they presented me throughout my graduate student experience.

I also gratefully acknowledge financial support from the University of Minnesota Department of Civil Engineering, Saint Anthony Falls Laboratory, and from the University of Minnesota Supercomputing Institute.

It has been inspiring to witness the collaborative effort of the Water Resources Engineering community at large. I owe a special thanks to Dr. Frédéric Murzyn for

providing valuable experimental data. The creators and proprietors of OpenFOAM also deserve recognition. Their belief in an open source philosophy and a free exchange of information has enabled me to explore the mysteries of fluid motion and fulfill a lifelong dream.

I would like to thank my fellow graduate students and the faculty and staff of the Saint Anthony Falls Laboratory for their kindness and support. Shafayat Jamil was an invaluable resource in teaching me the ins and outs of OpenFOAM. Intellectually stimulating conversations with Jon Schwenk and Mohammad Hajit will be sorely missed.

The support of my family and friends during these years has been truly motivating. The constant love and encouragement from my parents, siblings, extended family, and in-laws helped more than they know.

Finally, I am grateful beyond words to my wife Kasey. She has been my universal constant throughout this experience, pushing me, motivating me, encouraging me. Through all the turbulence she has listened, and shown me unwavering faith. I appreciate you, I love you.

Dedication

To my parents, Michael and Diane Witt. I see you working through me in everything I do. This is for you, from you, and because of you.

To Kasey. Pura Vida.

Disclaimer

The information, data, or work presented herein was funded in part by the Office of Energy Efficiency and Renewable Energy (EERE), U.S. Department of Energy, under Award Number DE-EE0002668 and the Hydro Research Foundation.

Table of Contents

List of Tables

List of Figures

1. Introduction

1.1. Background

The United States has a long and storied history of producing clean power from water, dating back to 1882 when the first hydroelectric facility in the world was constructed on the Fox River in Appleton, Wisconsin. The power generated from this plant, 12.5 kilowatts, was used to light a single home, a single business, and the hydropower plant itself (Library of Congress). Since that time, construction of over 2,500 hydroelectric dams has led to installed capacity of over 78 gigawatts, enough to power over 31 million homes (Hadjerioua et al., 2012).

Hydropower dam infrastructure is generally maintained under two specific operating conditions: power generating and non-power generating. Under power generating conditions, water is passed from the reservoir, via the penstock, to a hydropower turbine (Figure 1.1). The turbine is attached to a generator, which converts the mechanical energy of the spinning turbine into electrical energy. Power generating capacity is dependent upon the volume of water passed through the turbine and the hydraulic head, or the difference between the reservoir surface elevation and the turbine elevation. When power generation is not desired, flow is passed over the spillway into the stilling basin (Figure 1.2). The intersection of the spillway flow and the tailwater is characterized by strong turbulence and energy dissipation. As a result, pockets of atmospheric gases are captured and pulled into the flow where they are sheared to small bubbles. These bubbles have the potential to significantly increase dissolved gas levels in the tailwater through interfacial gas transfer.

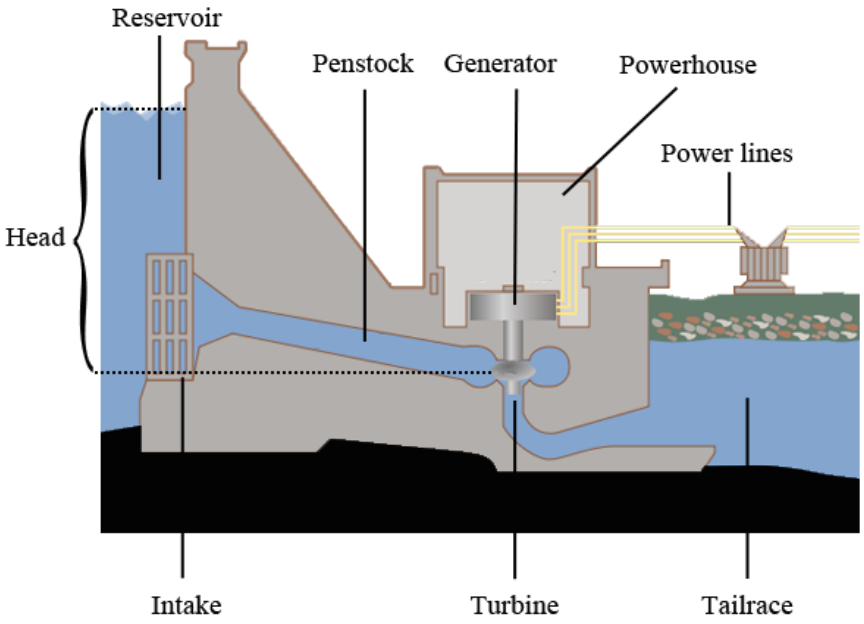

Figure 1.1. Simplified depiction of the power generating infrastructure at a hydroelectric dam. Adapted from Tennessee Valley Authority.

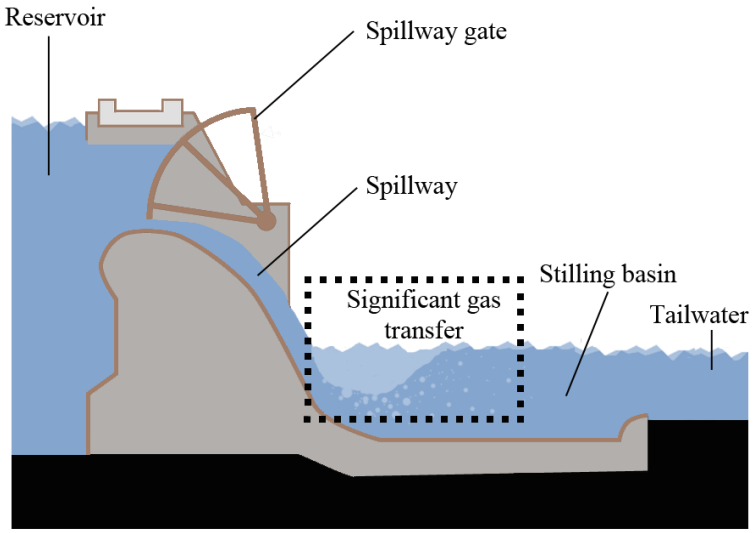

Figure 1.2. Flow over a gated spillway. Enhanced gas transfer occurs due to air entrainment. Adapted from Army Corps of Engineers.

A significant environmental consideration associated with hydropower electricity generation is the effect of operations on water quality. Of particular interest is the need to maintain appropriate concentrations of dissolved oxygen (DO) in water passed through or over the dam. Sufficient DO concentrations are required to preserve the assimilative capacity of the river, and help to promote stable aquatic ecosystems downstream (Railsback et al., 1991). In dam reservoirs, thermal stratification during warmer months produces two distinct layers of fluid (Figure 1.3). The upper, warmer layer (epilimnion) is generally well mixed by atmospheric processes and retains higher levels of DO due to interactions between surface turbulence and the diffusive boundary layer, and from photosynthesis. The lower, cooler layer (hypolimnion) is not well mixed, and experiences a depletion of DO due to the combined action of plant and animal respiration and biochemical oxygen demand. To maximize hydraulic head, i.e. electricity generation, the hydropower turbine intake is located near the bottom of the reservoir. When the turbine is operating, low DO water is pulled from the hypolimnion and passed into the tailrace. This may have fatal consequences for fish and other aquatic biota located downstream.

This problem is exacerbated on rivers with multiple dams, locks, and other navigation structures. Several river miles are typically needed for substantial gas transfer to occur between structures (Progress Energy, 2005). If low DO water reaches a downstream dam before it has achieved substantial reaeration, further DO depletion may occur in the downstream reservoir.

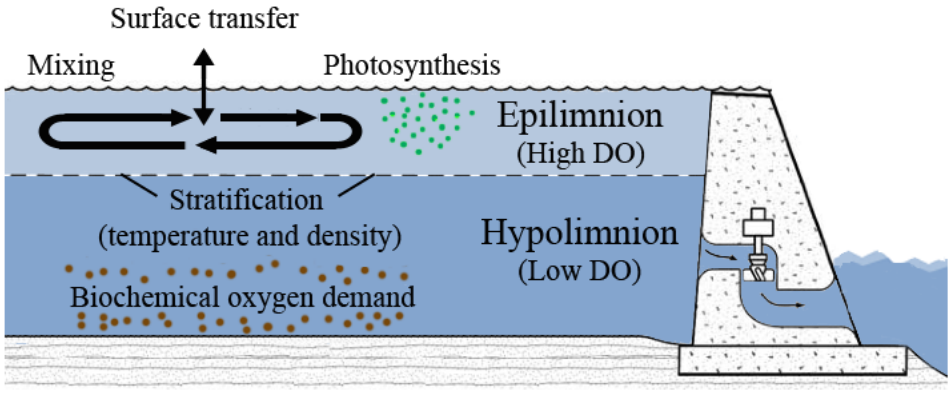

Figure 1.3. Thermal stratification of a hydropower reservoir, adapted from Peterson et al. (2003). The turbine intake is located in the hypolimnion, which is typically devoid of oxygen in summer months.

Numerous techniques are available to increase DO concentrations in the tailwater. These can be divided into four main categories: reservoir aeration, tailrace aeration, powerhouse aeration, and operational adjustments (EPRI, 1990). Of these, the least expensive and most often utilized is the operational technique of adjusting spillway flows (Sale et al., 1991). By spilling water from the epilimnion, increased DO levels are manifest downstream in two ways: (1) high DO water from the epilimnion is mixed with low DO water from the tailwater, resulting in a net increase of DO downstream, and (2) atmospheric gases are transferred into the flow through air entrainment in the stilling basin. When the reservoir is fully depleted of DO, (1) is not effective, and (2) becomes the best option for meeting state water quality standards.

Gas transfer in the stilling basin is significantly greater than that occurring naturally along the river. At low-head dams, this is due to the rapid transition from supercritical flow to subcritical flow known as the hydraulic jump. The hydraulic jump is a common energy dissipation mechanism employed in the stilling basin, effectively transferring the kinetic energy of the inflow into turbulence. It is characterized by an abrupt rise in free surface elevation, a turbulent shear layer, and a recirculating roller that cascades back upon itself (Figure 1.4). These processes combine to entrain a significant volume of air as bubbles at the impingement point of the spillway flow and tailwater.

Large air bubbles experience breakup immediately, producing smaller bubbles with a greater surface area to volume ratio than the original bubble. The diffusive flux of oxygen across the air-bubble interface is directly proportional to the surface area of the bubble in contact with water; hence, as more bubbles are generated through breakup, the potential for gas transfer is increased. Since oxygen gas in bubbles is in constant flux with the surrounding fluid, substantial mass transfer is expected when the residence time of bubbles in the stilling basin is sufficient. Additionally, the compression of bubbles due to hydrostatic pressure increases the DO concentration in the bubble, driving further mass transfer into the liquid phase.

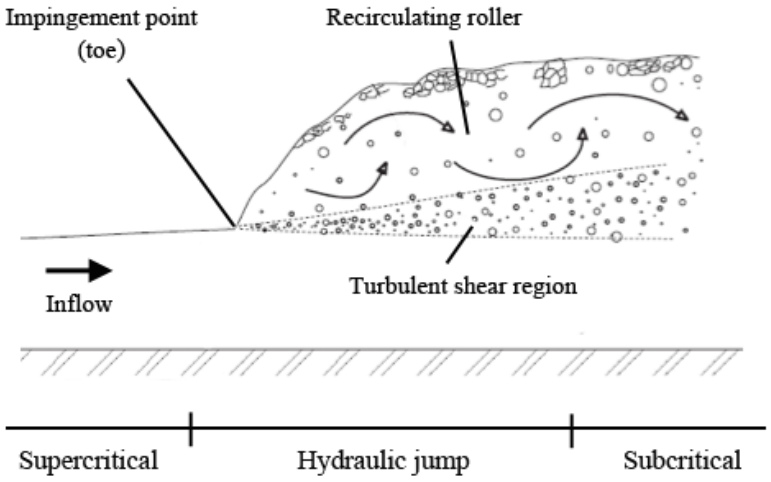

Figure 1.4. Typical hydraulic jump, adapted from Chanson (2010). Air entrainment at the toe results in large population of bubbles downstream.

This process occurs quickly and consistently within the existing energy dissipation infrastructure of the stilling basin, making hydraulic jump aeration an extremely cost effective DO mitigation technique. However, the loss of power generating revenue due to spilling is economically limiting. The volume of water necessary to increase DO in the tailwater is substantial (EPRI, 1990), and can quickly deplete the storage potential of the reservoir while reducing the discharge of power generating flow through the turbine. Dam owners may need to cease power generating

activities altogether if they are not able to meet the flow requirements outlined in their operating license. Additionally, the demands of competing stakeholders (recreation, fish and wildlife, navigation, government, etc.) may necessitate a specific reservoir or tailwater elevation, or a minimum discharge downstream, which can only be met by spilling flows at certain times. Under these conditions, there is no guarantee that spilling will achieve the desired or expected DO improvements.

Improved certainty regarding the effects of spillway releases is strongly desired within the hydropower industry, and could help reduce the financial impacts associated with altering flow schedules. A survey of several Army Corps of Engineers field offices (Wilhelms, 1988) identified the top DO concern at low-head dams as the lack of an ability to predict release DO. Dissolved oxygen profiles are extremely sensitive to largely unknown initial and boundary conditions. Consequently, the best method of quantifying aeration potential at a site is through field measurements of DO profiles upstream and downstream of the stilling basin, carried out under numerous flow conditions and for several gate openings (Urban et al., 2001). Under controlled conditions, the physical processes responsible for aeration can be related to the geometric and hydraulic conditions at a dam, resulting in constitutive relationships for gas transfer. However, field measurements are expensive, they are required at each individual structure to quantify the aeration potential, and there is no guarantee that the testing day is representative of the most commonly encountered flow scenario.

Many attempts to characterize gas transfer at prototype structures have coupled analysis of field data with predictive equations for flow parameters to develop an integrated model. These models fall into three general categories. The first predict gas transfer using a material control volume approach. A phenomenological relationship is proposed relating inflow parameters to the upstream DO concentration, a constitutive equation is established to solve for a representative downstream DO concentration, and model parameters are calibrated using field data (Wilhelms, 1988; Gulliver and Rindels, 1993; Geldert et al., 1998). A second approach applies a multi-control volume computational method to model gas concentration in specific sections of the spillway

using the general mass transport equation. These models have been developed in 1D (Urban et al., 2008) and 2D (Orlins and Gulliver, 2000) and require calibration with physical model data or field measurements. A third and increasingly viable modeling alternative is the use of a computational fluid dynamics (CFD) solver to simulate fluid motion on a small scale (Weber et al., 2004; Politano et al., 2007, 2009). The liquid flow field is resolved across the full structure, and then coupled to transport equations for bubbles and mass transfer. However, these models are highly sensitive to the bubble size distribution and void fraction specified at the inlet, which is largely unknown.

An improved understanding of the air-water boundary conditions at a hydropower facility would reduce the need for field calibration, and a fully validated numerical model could be easily extended to a variety of flow conditions. Current capabilities in numerical modeling of dissolved gas assume air entrainment is a known inlet boundary condition, and prescribe an initial bubble velocity, void fraction, and bubble diameter based on a trial and error calibration process where simulation results are compared with field measurements of total dissolved gas (Politano et al., 2009; Politano et al., 2012). Other models assume bubble size is inversely proportional to turbulence properties of the fluid (Orlins and Gulliver, 2000; Urban et al., 2008), though this technique may under predict bubble size at the point of entrainment, where turbulence is at a maximum yet large pockets of air are gulped into the jump. There is a strong need for an improved technique to simulate bubble size distributions and void fraction at the inlet boundary condition of gas transfer models. The investigation and refinement of novel predictive computational methods for gas transfer and air entrainment is the subject of this thesis.

1.2. Thesis overview

The purpose of this thesis is to investigate the air entrainment that occurs downstream of low-head hydropower dams. Low-head in this sense refers to dams that employ a hydraulic jump as an energy dissipater in the stilling basin. The investigation is carried out in two parts: (1) development of a predictive equation for gas transfer at low-head gated sills, and (2) numerical simulations of an air entraining hydraulic jump.

In Chapter 2, the field measurements of Urban et al. (2001) and Wilhelms (1988) are analyzed to develop a dimensionless relationship between inflow conditions, dam geometry, and oxygen transfer efficiency. A design parameter for gated sill dams provides a relationship between gate opening and oxygen transfer efficiency. This work was published in the Journal of Hydraulic Research Vol. 50, No. 5, (2012), pp. 521-531.

Chapter 3 describes the development and investigation of numerical simulations of the hydraulic jump. Three separate Froude number hydraulic jumps are simulated using an unsteady RANS, realizable k-ε turbulence model, with a Volume of Fluid treatment for the free surface. An analysis of three-dimensional vorticity reveals the complex interactions between spanwise and streamwise vortical structures and entrained air bubbles. The simulations are the first reported in the literature to capture void fraction and bubble size in a hydraulic jump without the use of an air entrainment subgrid model.

Chapter 4 further explores the numerical simulations in terms of bubbles and turbulence. Shear layer instabilities are better characterized, and the relationship between vortices and free surface fluctuations is analyzed. A new method for analyzing bubble clusters is presented, leading to a discussion of bubble clustering mechanisms.

A summary and conclusions are offered in Chapter 5.

2. Predicting oxygen transfer efficiency at low-head gated sill structures

This is the authors accepted manuscript of an article published as the version of record in the Journal of Hydraulic Research.
http://www.tandfonline.com/doi/full/10.1080/00221686.2012.729163#

2.1. Introduction

Predictions of oxygen transfer at gated dams are used to alter flow schedules to meet oxygen concentration requirements. Gated sills at low-head dams can, under some conditions, aerate flow to higher levels of dissolved oxygen. When water is passed under the gate, it forms a hydraulic jump as the supercritical upstream jet transitions into subcritical flow in the stilling basin. This flow regime is highly turbulent, leading to energy dissipation, air entrainment, bubble formation and oxygen transfer governed by inflow conditions and dam geometry. The combination of these processes results in a change of dissolved oxygen levels toward the local saturation concentration.

As shown in Figure 2.1, hydraulic jumps at gated sills are considered submerged or unsubmerged based on tailwater depth, y_3, and the approach flow Froude number $F = V_2/(gy_2)^{0.5}$ where V_2 = velocity of the approach flow and y_2 = depth of the approach flow. A submerged hydraulic jump occurs when discharge under a gate opening of depth y_g is overlaid by the static tailwater, y_{3S}. The issuing jet does not immediately have contact with the atmosphere and air entrainment is minimal. As y_g increases, the pressure difference determined by headwater depth, or y_1, drives discharge through the gate. If a sill is present, the pressure difference is determined by the static headwater, or y_{1S}. At a given discharge, the issuing jet has enough momentum to push the tailwater downstream, creating a supercritical flow of depth y_2 exposed to the atmosphere. An unsubmerged hydraulic jump is formed as this jet encounters y_{3S} (Figure 2.1). Intense turbulence in the

recirculating roller region entrains air pockets which are sheared into small bubbles. A decrease in bubble diameter leads to an increase in interfacial surface area and the potential for gas transfer (Gulliver at al. 1990).

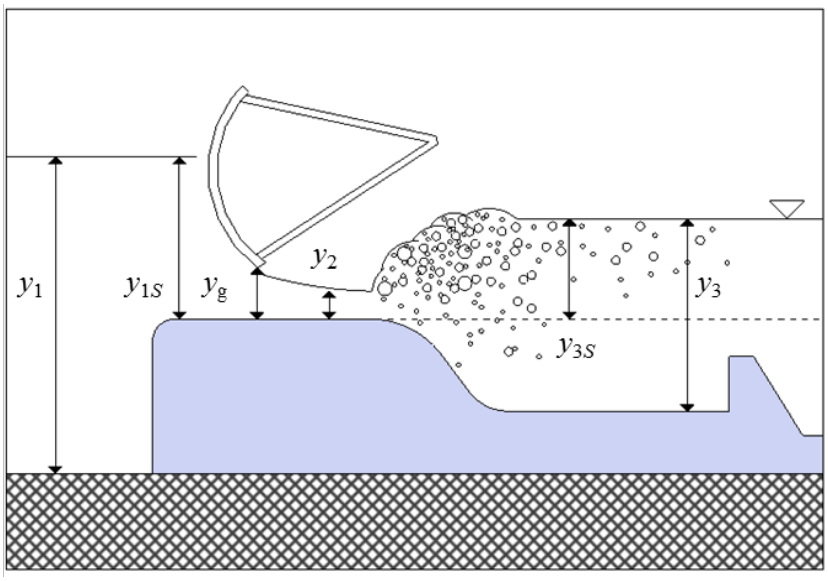

Figure 2.1. Typical gated sill and resulting hydraulic jump.

Previous work on gas transfer at hydraulic jumps has employed model flume data to calibrate and test predictive equations using upstream flow parameters (Holler 1971, Apted and Novak 1973, Avery and Novak 1978, Wilhelms et al. 1981, Chanson 1995, Kucukali and Cokgor 2009), with good agreement at the low Reynolds numbers that are typical of flumes. However these models do not scale to prototype structures, as bubble population, size, and air-water interfacial area do not scale with Froude number (Chanson 2007). Gas transfer measurements at full-scale gated sills have therefore been used to generate empirical fits of transfer efficiency to various hydraulic parameters (Preul and Holler 1969, Holler 1971, Tsivoglou and Wallace 1972, Foree 1976, Wilhelms 1988, Rindels and Gulliver 1991). These equations are valid at the tested site, but do not apply as well across multiple structures. An analysis by Gulliver et al. (1998) showed an

average standard error in transfer efficiency of 4 on a scale from 0 to 1 when these predictive equations were applied to measurements at five gated sill dams.

In this paper, gas transfer field measurements from six gated sill dams in the Ohio River watershed (Urban et al. 2001) and two on the Ouachita River (Wilhelms 1988) will be used to develop a set of predictive equations for oxygen transfer efficiency. Scaling relationships for bubble behavior in turbulent flows are used to develop a dimensionless relationship between oxygen transfer efficiency and site-specific hydraulic parameters. Model predictions are compared to field measurements at an additional field site adjusted for temperature and effective saturation concentration.

2.2. Gas transfer at hydraulic structures

The flux of any gas such as oxygen at an air-water interface is given as

$$\frac{\mathrm{d}C}{\mathrm{d}t} = k_L \frac{A}{\forall} (C_S - C), \tag{2.1}$$

where C = concentration of oxygen in water, t = time, k_L = liquid film coefficient, A = surface area of bubbles, $\forall$ = volume of water in which C and A are measured, and C_S is the saturation concentration of oxygen in water. The variables A and k_L are functions of time, and vary as the flow travels downstream. Utilizing their weighted-mean contributions to oxygen transfer across a structure allows the liquid film coefficient to be expressed as a bulk value K_L, and the average bubble surface area to be expressed in terms of the specific interfacial area $a = A/\forall$. Assuming C_S stays constant from upstream to downstream of a hydraulic structure, the integration of Eq. (2.1) gives

$$\frac{C_S - C_D}{C_S - C_U} = \exp(-K_L a t), \tag{2.2}$$

where C_D = downstream concentration of oxygen and C_U = upstream concentration of oxygen.

In order to relate the change in oxygen concentration to the initial oxygen deficit, transfer efficiency E is given as (Gameson 1957)

$$E = 1 - \exp(-K_L at) = \frac{C_D - C_U}{C_S - C_U}, \tag{2.3}$$

The parameter E is the primary indicator of oxygen transfer. A transfer efficiency of E = 1 means the hydraulic structure has transferred oxygen into the flow such that downstream concentrations of dissolved oxygen are equal to the local saturation concentration.

It is convenient to index all transfer efficiency values to a common temperature for comparison. Gulliver et al. (1990) developed an indexing relationship between the measured transfer efficiency of oxygen and the value at 20^{O}C as

$$E_{20} = 1 - (1-E)^{f_i}, \tag{2.4}$$

where E_{20} = transfer efficiency of oxygen at 20^{o}C and f_i is an indexing parameter, estimated for oxygen between 1 and 40^{O}C as $f_i = 1.0 + 0.02103\ (T-20) + 8.261 \times 10^{-5}\ (T-20)^2$ where T is water temperature in degrees Celsius. All measurements of E_{20} used in this paper have been indexed using Eq. (2.4).

2.3. Existing predictive equations for oxygen transfer efficiency

A prominent design feature of a gated dam is the hydraulic jump. At a typical gated sill structure, the hydraulic jump is the principal aerating mechanism and is assumed to be the main contributor to oxygen transfer. When available, field testing at a given structure is the most accurate means of developing a predictive equation for that site. Economic restrictions often preclude this option, and predictive models based on flume scale studies of hydraulic jumps are sometimes applied.

2.3.1. Unsubmerged hydraulic jumps in flumes

Froude numbers observed at prototype structures are typically on par with those in model flumes, and geometric scaling of hydraulic jumps is carried out with Froude number similitude. Viscosity and surface tension effects are also factors in the air entrainment and bubble formation processes, corresponding with Reynolds and Weber number similitude, respectively. The small scale of model flumes limits Reynolds and Weber numbers to the order of $10^4$and 10^3, respectively, while the prototype hydraulic jumps observed by Urban et al. (2001) and Wilhelms (1988) exhibit Reynolds and Weber numbers on an order of $10^7$and 10^6, respectively. In addition, geometric scaling of entrained bubble size is typically not possible, and significant scale effects have been observed in air bubble count rate and void fraction profiles when Froude similitude is maintained at various Reynolds numbers (Murzyn and Chanson 2008). With multiple forces important to the aeration potential of the hydraulic jump, a true dynamic similarity of dimensionless numbers is not possible (Chanson 2007). Thus, flumes developed strictly with Froude similitude will not capture the physics of oxygen transfer at prototype structures.

In laboratory flumes, increasing discharge typically leads to higher Froude numbers and increasing transfer efficiencies (Apted and Novak 1978, Wilhelms et al. 1981). At prototype structures, the pressure difference driving velocity under the gate remains relatively constant or decreases with gate opening, and the velocity of the issuing jet changes minimally with discharge. Concurrently, the gate opening and subsequent jet depth can increase an order of magnitude in the course of operation. The field measurements of Urban et al. (2001) and Wilhelms (1988) at unsubmerged hydraulic jumps show F calculated with a characteristic length of y_2 decreases as discharge increases (Figure 2.2). Predictive equations with a dependence on F will generally lead to decreasing transfer efficiency with increasing discharge at gated dams. This conflicts with field measurements, which suggest transfer efficiency increases with discharge at some structures (Figure 2.3).

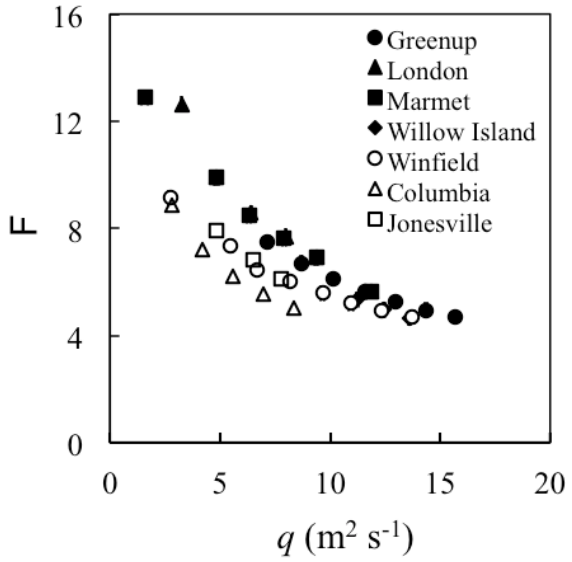

Figure 2.2. Comparison of Froude number of issuing jet and specific discharge.

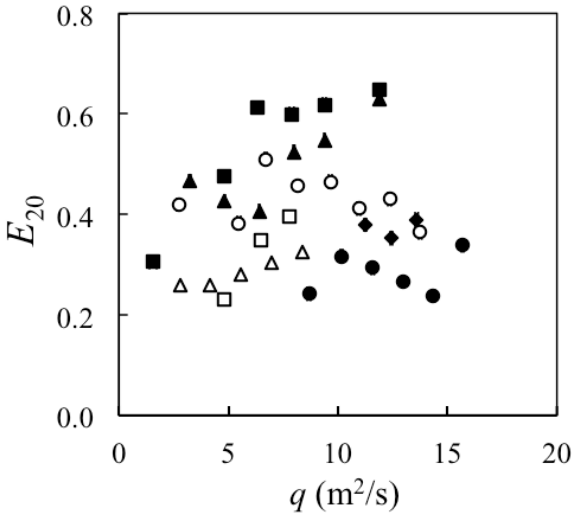

Figure 2.3. Comparison of oxygen transfer efficiency and specific discharge. Symbols see Figure. 2.2.

The importance of bubble physics on oxygen transfer is largely ignored in predictive equations developed from model flume experiments. As the roller descends upon the upstream jet, heavy turbulence captures large pockets of air which are sheared into small bubbles through the turbulent shear layer (Rajaratnam 1967). Experimental results from Resch and Leutheusser (1972) and Liu et al. (2004) show turbulent intensity and kinetic energy dissipation are predominant in the roller. Mean bubble diameter and bubble count are at respective minimum and maximum values in this region (Resch and Leutheusser 1974). Since turbulence decreases resistance to gas transfer, the liquid film coefficient will increase in the turbulent region (Azbel 1981). The combination of these processes contributes significantly to increasing the interfacial area for gas transfer. An accurate predictive model should include the effects of turbulence and kinetic energy dissipation on bubble behavior.

2.3.2. Unsubmerged hydraulic jumps at low-head dams

Historically, predictive equations for oxygen transfer efficiency at low head dams have been developed from field measurements at one site, or from measurements of one hydraulic parameter at multiple sites. Data are then plotted against an empirical formulation and a regression provides coefficients fitted to the specific structure or parameter. The predictive ability of these equations, illustrated in Figure 2.4, has limited application across multiple structures.

In a typical field investigation of oxygen transfer efficiency, headwater and tailwater elevations are assumed constant after the initial measurement, and total head across the structure does not change with gate opening. Early prototype-based predictive equation relied strictly on head loss to predict aeration efficiency, giving a constant transfer efficiency regardless of gate opening or discharge through the gate (Tsivoglou and Wallace 1972, Foree 1976). The transfer efficiency may be accurate for a single gate opening but cannot be applied to multiple gate openings at a single structure. Later

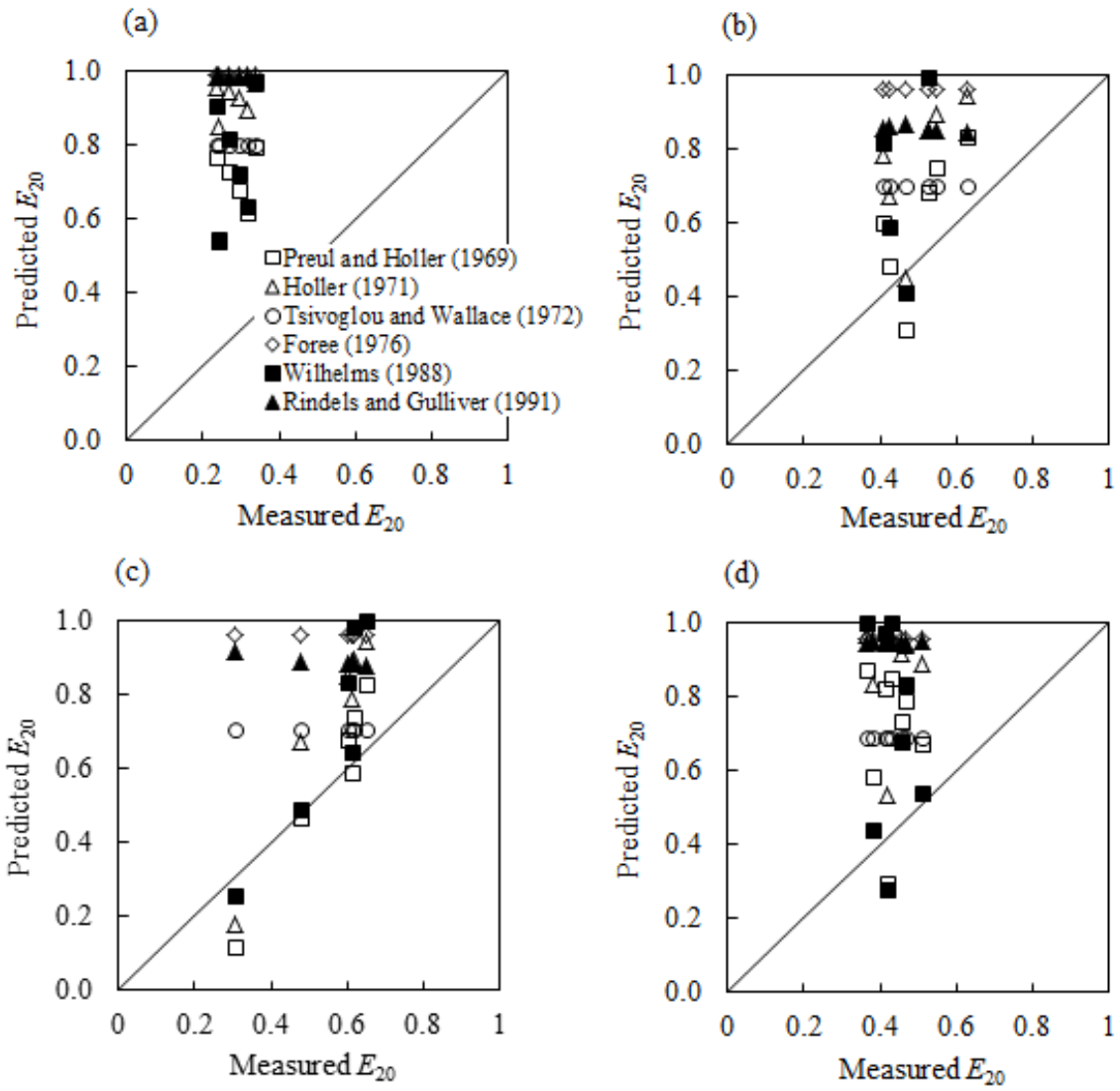

Figure 2.4. Comparison of measured and predicted oxygen transfer efficiency at (a) Greenup, (b) London, (c) Marmet and (d) Winfield (Urban et al. 2001). 1:1 slope denotes perfect agreement.

developments of predictive equations included both head and discharge through the gate (Wilhelms 1988, Rindels and Gulliver 1991), although there is disagreement as to whether transfer efficiency is directly or inversely proportional to discharge (Figure 2.3).

The formulation proposed in this paper utilizes the transfer efficiency data of Urban et al. (2001) and Wilhelms (1988), which includes field measurements at various gate openings from six dams with gated sills on the Ohio River watershed and two on the Ouachita River, respectively. The model provides gated sill operators an improved ability to apply predictive equations across multiple sites.

2.4. Adjustment for effective saturation concentration

The saturation concentration in the bubbles needs to be adjusted for the pressure of the bubbles. When oxygen is measured directly in most natural waters the saturation concentration is assumed constant to simplify the integral calculation of Eq. (1). For turbulent flow at hydraulic structures, entrained oxygen bubbles experience greater hydrostatic and dynamic pressures as they descend into the tailwater, increasing the partial pressure of oxygen in the bubble. For example, a hydrostatic pressure distribution with depth implies that a bubble three meters beneath the surface experiences a saturation concentration that is 129% of atmospheric saturation. This increase in local saturation concentration would influence oxygen transfer, and thus the downstream dissolved oxygen concentration.

Consequently, the saturation concentration felt by the bubbles cannot be assumed equivalent to the local atmospheric saturation concentration, and a correction is required when oxygen transfer efficiency is computed directly from oxygen measurements. One proposed method of correction is that of Gulliver et al. (1997), who introduced an effective saturation concentration ratio given as

$$\frac{C_{SE}}{C_S} = \frac{1}{C_S}\left(\frac{C_D - C_U}{E_{O_2CH_4}} + C_U\right), \tag{2.5}$$

where C_{SE} = effective saturation concentration and $E_{O_2CH_4}$ is the transfer efficiency of oxygen indexed from methane. Gulliver et al. found that methane exists in most rivers in sufficient quantities to be used as an in-situ tracer gas to estimate oxygen transfer efficiency. Because the saturation concentration for methane in most natural waters is close to zero, the integral of Eq. (2.1) for methane results in Eq. (2.3) with $C_S = 0$, allowing for the development of Eq. (2.5).

The effective saturation ratio, or C_{SE}/C_S, is used to estimate an effective bubble depth, d_{eff},

$$\frac{C_{SE}}{C_S} = \frac{\gamma d_{eff}}{p_{atm}} + 1, \tag{2.6}$$

where p_{atm} = local atmospheric pressure and γ = specific weight of water. The effective bubble depth represents the point in the tailwater where pressure in the submerged bubbles is in equilibrium with the effective saturation concentration. When bubbles are at depth, C_{SE} is greater than C_S. Obtaining d_{eff} provides a means to correct oxygen transfer efficiency calculations based on direct oxygen measurements. When methane or another tracer measurement is not available to compute Eqs. 2.5 and 2.6, estimates of d_{eff} are made based on dam geometry and an analysis of the flow (Hibbs and Gulliver 1997, Hetteriachchi et al. 1998). These formulations of d_{eff} are proportional to the tailwater and typically range from zero to 2/3 the tailwater depth.

To estimate the effective depth for gated sills, d_{eff} values observed by Urban et al. (2001) with uncertainty less than 1 m are plotted against the tailwater depth. A linear regression of the resulting relationship yields

$$d_{eff} = 0.276\, y_3. \tag{2.7}$$

Adjustment of E from Equations (2.6) and (2.7) represents an estimate of the true measured oxygen transfer efficiency at gated sills.

2.5. Predictive model formulation

The transition at the gate from submerged to unsubmerged hydraulic jump correlates with an increase in oxygen transfer efficiency (Hettiarachchi et al. 1998, Urban et al. 2001). Existing predictive models do not take this transition into account. Rather, they seek to predict oxygen transfer for all gate openings with one equation, or the model applies only to unsubmerged hydraulic jumps. Characterization of the aeration capacity of a gated structure is first accomplished by determining whether the flow under the gate forms a submerged or unsubmerged hydraulic jump.

When water passes under the gate, the streamlines converge as they pass through the gate opening, forming a vena contracta. The depth at the vena contracta is taken as the upstream depth of the hydraulic jump. Clemmens et al. (2003) developed a method for estimating the depth of the vena contracta downstream of a submerged radial gate based on gate geometry. An analysis of the Greenup and Willow Island dam geometry revealed a contraction coefficient of between 0.61 and 0.63 for the range of tested gate openings. The tainter gates in this study are of similar dimensions, and a contraction coefficient of 0.63 is applied to the remaining tainter gates (Smithland, Jonesville, Columbia, Red River). The same contraction coefficient will be applied to roller gates (London, Marmet, Winfield), as the physics of the flow are similar and the literature on calibration of roller gates is limited. The upstream jet depth is calculated as

$$y_2 = 0.63\, y_g. \tag{2.8}$$

A precise estimate of exit parameters at the gate is used to calculate the sequent depth of the upstream flow. Thus site-specific gate conditions will determine if the hydraulic jump is submerged or unsubmerged.

2.5.1. Submerged hydraulic jump

If the upstream jet is submerged, gas transfer is primarily a function of the turbulence at the water surface, through a process known as surface renewal (Tamburrino and Gulliver 2002). The oxygen transfer coefficient is proportional to (Gulliver 2007)

$$K_L \propto = \sqrt{\frac{D\Delta V^2}{\upsilon}}, \tag{2.9}$$

where ΔV is taken as the difference between velocities before and after the jump, or $V_2 - V_3$ where V_3 = tailwater velocity, D = diffusion coefficient of oxygen in water and ν = kinematic viscosity of water. The specific interfacial area per volume available for gas transfer is proportional to the tailwater depth, y_3,

$$a = \frac{A}{\forall} \propto \frac{1}{y_3}. \tag{2.10}$$

The time scale for surface renewal will be estimated as the residence time of oxygen in the tailwater carried by the mean flow, or

$$t \propto \frac{2y_3}{V_2 - V_3}. \tag{2.11}$$

Combining Eqs. (2.9), (2.10) and (2.11) with Eq. (2.3) gives a prediction for transfer efficiency at unsubmerged hydraulic jumps of

$$E_{20} = 1 - \exp(-K_L a t) = 1 - \exp\left(-\beta_1 \sqrt{\frac{D}{\upsilon}}\right), \tag{2.12}$$

where β_1 is a fitting coefficient. Equation 2.12 suggests transfer efficiency for unsubmerged jumps is constant regardless of gate opening. When the roller of the

hydraulic jump is submerged air entrainment is minimal and most aeration is due to turbulence at the free surface.

The small transfer efficiencies of submerged hydraulic jumps result in substantial relative measurement uncertainties. For this reason, the visual observations of Urban et al. (2001) are used to calibrate an average E_{20} for submerged hydraulic jumps. The transition from submerged to unsubmerged hydraulic jump was witnessed at transfer efficiencies less than 0.25. Taking an average of these measurements gives $E_{20} = 0.056$. The resulting value of β_1 is computed from Eq. (2.12) to be 1.29.

2.5.2. Unsubmerged hydraulic jump

If the upstream gate is unsubmerged, the variables in Eq. (2.3), K_L, a and t, become dependent upon oxygen transfer across bubble surfaces. As bubbles are created at the toe of the jump and transported through the roller, they transfer oxygen into the flow at a rate proportional to the liquid film coefficient. Azbel (1981) developed a scaling relation for the bulk liquid film coefficient in a bubbly turbulent flow as

$$K_L \propto \frac{D^{1/2} U^{3/4}}{L^{1/4} \upsilon^{1/4}} \frac{(1 - \varphi)^{1/2}}{(1 - \varphi^{5/3})^{1/4}}, \tag{2.13}$$

where U = characteristic velocity of large eddies, L = a characteristic length scale of large eddies and φ = gas void ratio of the air in water. Since void ratios in the roller do not vary greatly for hydraulic jumps of low Froude number (Resch et al. 1974), the terms containing φ are incorporated into a constant coefficient. The characteristic velocity of the largest eddies is assumed proportional to the upstream jet velocity, or V_2. Long et al. (1991) showed the largest eddies in the roller are approximately the size of the depth of the jump. Thus the characteristic length of the resulting predictive equations is taken as $\Delta h = y_{3S} - y_2$, or the difference between the static tailwater and the upstream jet depth.

The interfacial area available for gas transfer is directly related to bubble size in the turbulent shear region. An expression for the interfacial area of a bubble swarm is often given as

$$a \propto \frac{\varphi}{d_b} = \frac{q_a}{d_b q}, \tag{2.14}$$

where q_a = specific discharge of air entrained into the flow, $q = V_2 y_2$ = specific discharge of water and d_b is the mean bubble diameter. The bubbles captured in the toe of the roller are responsible for the majority of oxygen transfer into the flow. For perspective, assuming a void ratio of 0.1 as observed by Resch et al. (1974) and a mean bubble diameter of 2 mm, a 1 m^3 control volume in a typical hydraulic jump roller would have a collective bubble surface area of approximately 130 m^2.

Empirical studies show the air entrainment rate q_a in hydraulic jumps is proportional to F (Rajaratnam 1967, Resch et al. 1974, Chanson 1995). Herein, the air entrainment rate is considered proportional to the velocity of the upstream jet since F was shown to decrease with gate opening, and the results of Urban et al. (2001) suggest air entrainment generally increases with gate opening. The size of entrained air pockets in highly turbulent flows corresponds with surface tension over density (Hinze 1955), and is inversely proportional to the force of gravity acting on breaking waves in the roller. The rate of air entrainment is thus assumed to be

$$q_a \propto V_2 \sqrt{\frac{\sigma}{\rho g}}, \tag{2.15}$$

where σ = surface tension, ρ = density of water and g = acceleration of gravity.

A common relationship for bubble diameter in a shear flow based on a critical Weber number is (Hinze 1955)

$$d_b \propto \left(\frac{\sigma}{\rho}\right)^{3/5} \varepsilon^{-2/5}, \tag{2.16}$$

where d_b = bubble diameter and ε = rate of turbulent kinetic energy dissipation per unit mass. Energy dissipation is subject to a higher degree of unpredictability due to acute differences in spillway geometry and inflow conditions. Liu et al. (2004) estimated the rate of energy dissipation in hydraulic jumps with low Froude numbers as

$$\varepsilon = \frac{gq\Delta H}{L_j 0.5\left(y_2 + y_3\right)}\ , \tag{2.17}$$

where ΔH is the energy loss across the jump and L_j = length of the hydraulic jump, chosen as (Ivanchenko 1936)

$$L_j = 10.6\left(\mathrm{F}^2\right)^{-0.185}\left(y_3 - y_2\right)\ , \tag{2.18}$$

Taken together, Eqs. (2.14) through (2.18) provide a characteristic relation of the specific surface area, a, of entrained air bubbles in the roller of a hydraulic jump.

The majority of air entrainment has been shown to occur at the interface of the upstream jet and tailwater, where bubble population and void ratio are at a maximum (Resch and Leutheusser 1974). Since bubbles are transported through the turbulent shear layer by vortices the size of the jump (Long et al. 1991), their residence time is proportional to the time of migration from the top of the upstream jet to the top of the roller, or

$$t \propto \frac{\Delta h}{V_r}\ , \tag{2.19}$$

where V_r is the average bubble rise velocity. Bubbles in a shearing flow are generally in a transition from a spherical bubble to a mushroom cap bubble, where their rise velocity is assumed relatively constant at 0.25 m/s (Azbel 1981).

Combining Eqs. (2.13) through (2.19) results in the following expression for E_{20}:

$$E_{20} = 1 - \exp(-K_L at) = 1 - \exp\left(-\beta_2 \frac{D^{1/2} V_2^{3/4}}{\Delta h^{1/4} \upsilon^{1/4}} \left(\frac{\rho^3 \varepsilon^2}{\sigma^3}\right)^{1/5} \left(\frac{\sigma}{\rho g y_2^2}\right)^{1/2} \frac{\Delta h}{V_r}\right), \quad (2.20)$$

where β_2 = a proportionality constant. Equation 2.20 can be recast in dimensionless form as:

$$E_{20} = 1 - \exp(-K_L at) = 1 - \exp\left(-\beta_2 \, \mathrm{Sc}^{-0.5} \, \mathrm{R}_h^{-0.25} \mathrm{F}_h \, \mathrm{W}_h^{0.1} \, \Psi\right), \quad (2.21)$$

where

$$\mathrm{Sc} = \frac{\upsilon}{D}, \quad (2.22)$$

$$\mathrm{R}_h = \frac{V_2 \Delta h}{\upsilon}, \quad (2.23)$$

$$\mathrm{F}_h = \frac{V_2}{\sqrt{g \Delta h}}, \quad (2.24)$$

$$\mathrm{W}_h = \frac{\rho V_2^2 \Delta h}{\sigma}, \quad (2.25)$$

$$\Psi = \varepsilon^{2/5} \frac{\Delta h^{7/5}}{y_2} \frac{1}{V_r V_2^{1/5}}. \quad (2.26)$$

A dimensionless turbulence dissipation term, Ψ, is introduced from Eq. (2.20) to capture the relationship of turbulence dissipation rate to bubble size and bubble gas transfer. The contributions of the Ψ parameter to gas transfer are thought to be subject to more variability than the contributions of the remaining dimensionless terms due to the dependence on the length of the jump, which is not precisely defined. Thus, a log-linear regression is performed on β_2 and Ψ to fit the equation to existing data. The result gives an exponent of 0.06 for Ψ and a leading coefficient of 27.1 for β_2:

$$E_{20} = 1 - \exp\left(-27.1\ \mathrm{Sc}^{-0.5}\ \mathrm{R}_h^{-0.25}\mathrm{F}_h\ \mathrm{W}_h^{0.1}\ \Psi^{0.06}\right), \tag{2.27}$$

Equation (2.27), developed from relations for bubble behavior in turbulent shear flows, provides a prediction for oxygen transfer efficiency of unsubmerged hydraulic jumps at a low-head gated sill structure.

A comparison of Eq. (2.27) to the field measurements of Urban et al. (2001) and Wilhelms (1988) shows improved accuracy in predicting oxygen transfer efficiency (Figure 2.5). The standard error of the predictions around a perfect fit is 0.078, a substantial improvement over previous predictive equations (Gulliver et al. 1998). Direct measurements of oxygen were obtained by Wilhelms (1988), thus Eqs. (2.6) and (2.7) are used to determine C_{SE}, which replaces C_S in Eq. (2.3). Based on the visual observations of Urban et al. (2001), transfer efficiencies less than 0.25 are assumed to result from submerged hydraulic jumps and are not included in the calibration of Eq. (2.27).

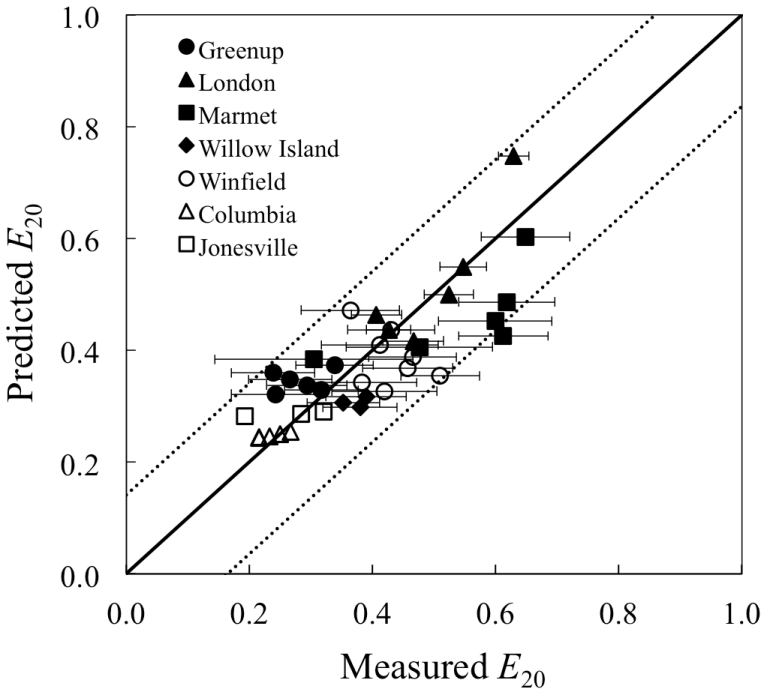

Figure 2.5. Comparison of measured and predicted oxygen transfer efficiency at seven gated sill dams with unsubmerged hydraulic jumps. Error bars denote measurement uncertainty, 1:1 slope denotes perfect agreement, - - - denotes 95% confidence interval.

2.6. Discussion

Static tailwater depth and hydraulic jump height are found to be good indicators of oxygen transfer efficiency. As the gate rises, Δh decreases and turbulent fluctuations at the free surface of the upstream jet approach the free surface of the tailwater, where resistance to the flow is less. Air pockets of greater volume are entrained at a higher frequency as Δh approaches 0. Since the magnitude of Δh is determined from the static tailwater depth, a lower y_{3S} will correspond with a lower Δh and higher transfer efficiencies. Oxygen transfer efficiency was greatest at Marmet and London, which had the lowest measured y_{3S} of 1.01 m and 0.89 m respectively, and a Δh that approached 0 at the maximum tested y_g. The four structures with the largest y_{3S} and Δh, Greenup, Willow Island, Columbia and Jonesville, respectively, had the four lowest measured and

predicted oxygen transfer efficiencies. Smithland, where only submerged hydraulic jumps were observed, had a y_{3S} and Δh nearly twice that of Greenup. By choosing Δh as the characteristic length, F_h also increases with discharge and correlates directly with E_{20}.

From Eq. (2.27), a predictive relationship between transfer efficiency and gate opening for a range of y_{3S} and y_{1S} at a constant sill depth of 5m is developed (Figure 2.6). Transfer efficiency is shown to increase as gate opening and discharge increase, at a rate controlled by y_{3S}. A deeper y_{3S} provides greater resistance to the momentum of the upstream jet and requires greater discharge to form a stable hydraulic jump. Once the upstream jet has enough momentum and the hydraulic jump is fully unsubmerged, aeration increases significantly.

This observation differs from an Ogee crest-type spillway, where the greatest indicator of oxygen transfer efficiency is head (Rindels and Gulliver 1991). At such structures the velocity of the plunging jet, and the depth to which entrained bubbles are pushed into the tailwater, increase with head. The impact of tailwater depth on energy dissipation is not as substantial when compared to gated sills, where energy dissipation is directly related to the geometry of the hydraulic jump. Head does have a noticeable effect on E, as evidenced by the rise in predicted E_{20} from (a) to (d) in Figure 2.6. However, the gains made in velocity and momentum through increasing head are not enough to overcome the effect of a large downstream static tailwater depth.

Given spillway rating curves and headwater, tailwater and sill depth, a spillway operator has the ability to predict oxygen transfer efficiency for a range of flow conditions at gated sill structures. Figure 2.6 is a good indicator of E_{20} when gate opening is the only parameter available to control discharge.

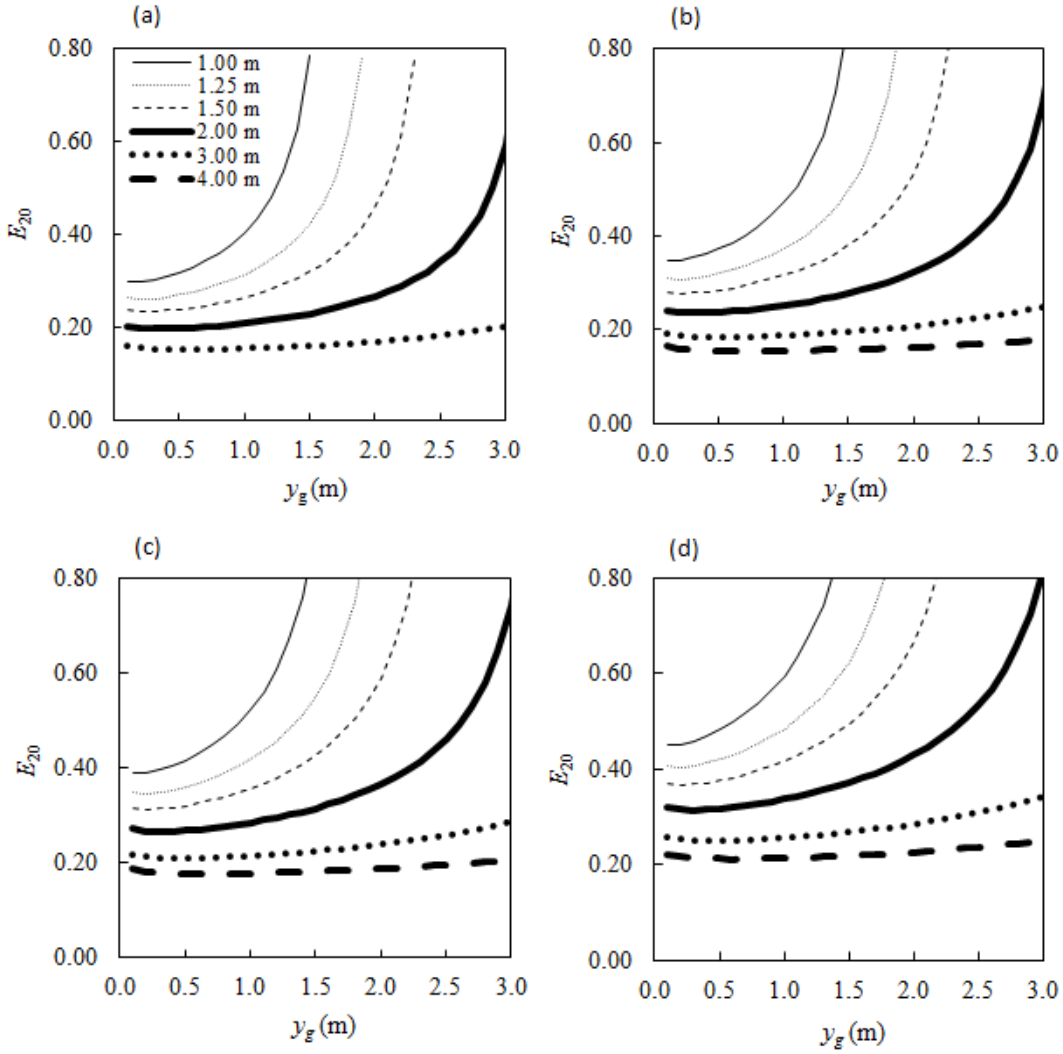

Figure 2.6. Predicted oxygen transfer efficiency based on gate opening for six different static tailwater elevations with static headwater depth of (a) 4m, (b) 6m, (c) 8m and (d) 12m. Sill depth is held constant at 5m.

2.7. Application: prediction of oxygen transfer efficiency at Markland Lock and Dam

The method described above is applied to the Markland Lock and Dam, a low head gated sill on the Ohio River where Hetteriachchi et al. (1998) performed oxygen transfer efficiency measurements for a variety of gate openings. An analysis of the gate rating curves gives q for each gate opening. Relevant elevations obtained from the literature are y_{1S} = 12.5m and y_{3S} = 1.53m. Velocity at the vena contracta is taken as

$$V_2 = \sqrt{2g\left(y_{1S} - 0.5y_2\right)}\,, \tag{2.28}$$

The required variables are calculated and inserted into Eq. (2.27) to get a prediction for E_{20} (Table 2.1).

Hetteriachchi et al. (1998) performed oxygen measurements, which must be adjusted for the effective saturation concentration ratio as described above. The adjusted efficiencies are then indexed to 20^{o}C using Eq. (2.4) (Table 2.2).

Table 2.1. Computing Eq. (2.27) using field measurements of Hetteriachchi et al. (1998).

Variable	y_g	q	$Sc^{-1/2}$	$R_h^{-0.25}$	F_h	$W_h^{0.1}$	$\varepsilon^{0.4}$	$\Psi^{0.06}$	Predicted E_{20}
Equation			[2.22]	[2.23]	[2.24]	[2.25]	[2.17, 2.18]	[2.26]	[2.27]
Markland	0.15	2.15	0.047	0.015	4.18	4.65	9.54	1.43	0.387
	0.30	4.22	0.047	0.015	4.32	4.62	8.81	1.36	0.384
	0.46	6.20	0.047	0.015	4.47	4.58	8.34	1.31	0.388
	0.61	8.11	0.047	0.015	4.65	4.55	7.99	1.28	0.395
	0.76	9.94	0.047	0.016	4.85	4.50	7.71	1.25	0.405
	0.91	11.69	0.047	0.016	5.08	4.46	7.50	1.22	0.418
	1.07	13.38	0.047	0.017	5.34	4.41	7.34	1.20	0.433
	1.22	15.01	0.047	0.017	5.66	4.36	7.23	1.18	0.451
	1.37	16.58	0.047	0.018	6.05	4.29	7.18	1.15	0.474
	1.52	18.10	0.047	0.018	6.53	4.23	7.20	1.13	0.502

Table 2.2. Adjusting measured E_{O2} values for effective saturation concentration and indexing to 20^o C. Data obtained by Hetteriachchi et al. (1998).

Variable	y_g	C_U/C_S	C_D/C_S	E (using C_S)	d_{eff}	C_{SE}/C	E (using C_{SE})	E_{20}
Equation				[2.3]	[2.7]	[2.6]	[2.3]	[2.4]
Markland	0.15	0.761	0.826	0.27	1.35	1.13	0.18	0.16
	0.30	0.759	0.863	0.43	1.35	1.13	0.28	0.25
	0.46	0.767	0.890	0.53	1.35	1.13	0.34	0.30
	0.61	0.762	0.934	0.72	1.35	1.13	0.47	0.42
	0.76	0.765	0.953	0.80	1.35	1.13	0.51	0.47
	0.91	0.758	0.965	0.85	1.35	1.13	0.55	0.50
	1.07	0.763	0.968	0.87	1.35	1.13	0.56	0.51
	1.22	0.768	0.977	0.90	1.35	1.13	0.58	0.52
	1.37	0.764	0.975	0.89	1.35	1.13	0.57	0.52
	1.52	0.769	0.979	0.91	1.35	1.13	0.58	0.53

A comparison of the predicted E_{20} values and the measured and adjusted E_{20} values shows good agreement for nearly all transfer efficiencies (Figure 2.7). Adjusted transfer efficiencies at or below 0.25 are not compared with the model due to uncertainty in the gate opening when the hydraulic jump transitions from submerged to unsubmerged. Over prediction at lower measured transfer efficiencies is due to uncertainty in the transition from submerged to unsubmerged hydraulic jump, and is consistent with other locations. Figure 2.7 highlights the pronounced effect of C_{SE} on E. The effective saturation concentration provides for transfer efficiency measurements that are more representative of the pressure force acting on an entrained air bubble as it passes a hydraulic structure.

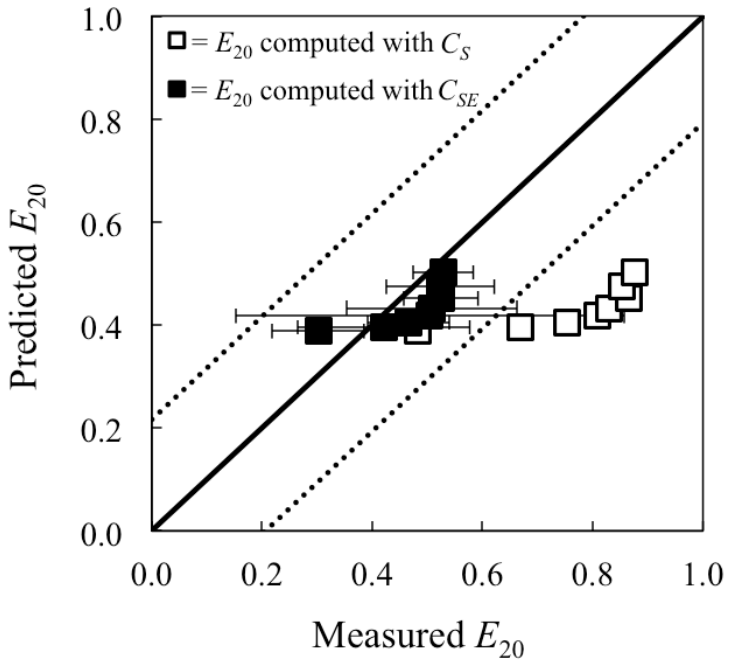

Figure 2.7. Comparison of measured and predicted oxygen transfer efficiencies.

2.8. Conclusions

An improved predictive model is formulated to compute oxygen transfer efficiency at gated sill structures using derived relationships for turbulence, scaling of bubble diameter and the liquid film coefficient. Previous models were developed either from flume experiments, where bubbles do not scale appropriately, or from prototype structures, where measurements at a limited number of sources prohibited wider applicability. The current formulation incorporates bubble behavior in turbulent flows, and is calibrated with field measurements at seven gated sill dams.

The new equation can be applied to predict E_{20} at low-head dams with gated sills and unsubmerged hydraulic jumps in the stilling basin. When the hydraulic jump is submerged, oxygen transfer is predicted to be constant, controlled by turbulence at the free surface. When the jump is unsubmerged, bubble formation in the roller of the jump leads to increased bubble-water mass transfer. A relationship is derived relating oxygen transfer efficiency to Schmidt number, Froude number, Reynolds number, Weber number and a dimensionless turbulence term, Ψ, each calculated using the height of the hydraulic jump as the characteristic length scale.

The relations developed indicate oxygen transfer efficiency is dependent on the upstream velocity, gate opening and static tailwater depth. At a given structure, E_{20} increases with gate opening. Across multiple structures, E_{20} increases as static tailwater depth decreases. When direct oxygen measurements are carried out, an adjustment for the increased saturation concentration in the tailwater is required before comparing measured E_{20} to predicted $E_{20,}$ or when using E_{20} to predict downstream oxygen concentration.

Accurate forecasting of oxygen transfer can decrease uncertainty in hydropower facility operation and lead to optimization of gate operation schedules. Potential structural changes and their impact on oxygen transfer may also be examined.

3. Simulating air entrainment and vortex dynamics in a hydraulic jump

3.1. Introduction

A hydraulic jump arises when supercritical flow transitions to subcritical flow, resulting in turbulence, energy dissipation, air entrainment, and higher rates of gas transfer. A hydraulic jump is frequently employed downstream of dams to dissipate energy and improve oxygen levels in the flowing water. Air entrainment occurs when pockets of atmospheric gases are captured as bubbles during an oscillation of the toe of the jump. These pockets of air experience breakup in the turbulent shear region, producing bubbles that either rise into the roller where they are released to the atmosphere, or travel downstream with the bulk flow where air-liquid gas transfer can occur. Aeration at the free surface is simultaneously enhanced by contributions from breaking waves.

Experimental investigations of air entrainment have revealed a characteristic structure of bubbly flow in the hydraulic jump (Rajaratnam, 1967; Resch et al., 1974; Avery and Novak, 1978; Murzyn and Chanson, 2007). Impingement of the recirculating roller upon the upstream jet creates the primary source of air bubbles transported downstream. The void fraction, φ, or the proportion of air to water and air together, is often used to characterize the time-averaged behavior of bubbles within the jump. The frequency of bubbles and the maximum void fraction are strongly linked to the inflow Froude number (Chanson and Brattberg, 2000), defined as $Fr = U_o/(gd)^{0.5}$, where U_o and d are respectively velocity and depth of the upstream jet, and g is the gravitational acceleration. Void fraction measurements have been carried out with relative accuracy using dual-tip conductivity probes (Straub and Anderson, 1958; Rajaratnam, 1967; Chanson, 2007b), hot-wire anemometry (Resch et al., 1974), visual techniques (Hoyt and

Sellin, 1989; Mossa and Tolve, 1998), and optical fiber probes (Murzyn et al., 2005). It has been found that the maximum void fraction at a given elevation increases rapidly downstream from the toe, peaking in the roller region before decreasing gradually downstream (Rajaratnam, 1962). The shape of the void fraction profile within the hydraulic jump varies depending on inflow conditions and the boundary layer thickness of the inflow (Resch et al., 1974). Herein, the discussion will focus exclusively on hydraulic jumps with a thin boundary layer in the incident flow, otherwise characterized as partially-developed supercritical inflow. In the turbulent shear region, the void fraction exhibits a Gaussian distribution about a maximum air concentration located slightly above the location of maximum bubble frequency (Resch et al., 1974; Chanson and Brattberg, 2000). The void fraction increases sharply towards unity as the free surface is approached. Accurate estimates of void fraction in the shear and interfacial regions are required to develop predictions of gas transfer rates, cavitation, and flow bulking (Wilhelms and Gulliver, 2005).

Several inherent difficulties inhibit accurate air bubble measurements in a multiphase flow, including signal interpretation uncertainty in turbulent flow regimes, bubble-probe interaction errors, and the detection of small bubbles (Boyer et al., 2002). Consequently, a relatively limited number of experiments in the literature characterize air bubble diameter throughout the hydraulic jump. Resch et al. (1974) analyzed hot-wire signals to estimate bubble diameter from air exposure time, and found the PDF of bubble diameter exhibits a log normal distribution with a peak around 5 mm. A similar technique was used to show that maximum bubble diameter decreases with distance from the toe (Babb and Aus, 1981). Optical fiber probes have been used to characterize bubble diameter in the turbulent shear region as ranging from 2 mm to 12 mm for hydraulic jumps of $2 < Fr < 8$ (Murzyn et al., 2005). Others have neglected to define a bubble diameter, and instead present bubble chord times, or the time spent by the bubble on a conductivity probe tip (Murzyn and Chanson, 2007; Chanson, 2007b). From these experiments, the bubble chord time PDF also exhibits a log normal distribution for a wide range of *Fr* jumps. As *Fr* is increased, the PDF becomes more skewed as both the

maximum upper chord time and the number of small bubbles increase. Because of the simplifying assumptions employed in each of these techniques, measurements of bubble size in a hydraulic jump are typically regarded as approximate values (Babb and Aus, 1981).

The relationship between turbulence and bubble dynamics is not completely understood, as the intrusive nature of multiphase experimental studies limits the acquisition of instantaneous flow data. Formation of the shear layer begins at the toe where the impingement of the roller upon the upstream jet is the primary source of both air and vorticity (Hornung et al., 1995; Dabiri and Gharib, 1997). Shear layer instabilities induced by toe oscillations produce spanwise vortices that travel downstream where, through pairing, they can increase in size from $2d$ to $7d$ (Long et al., 1991; Zhang et al., 2012). The strength of turbulence in the shear region is at a maximum near the toe (Resch and Leutheusser, 1972; Liu et al., 2004), leading to bubble breakup and corresponding with the location of highest bubble frequency (Murzyn et al., 2005). Recent studies have revealed positive correlations between air entrainment and turbulent fluctuations of the roller surface (Murzyn and Chanson, 2009; Chachereau and Chanson, 2011a).

Hoyt and Sellin (1989) observed a braid-roll structure within the shear layer that contributes to air entrainment in the roller, and proposed the hydraulic jump be interpreted as a mixing layer with both transverse and streamwise coherence. Within a typical mixing layer, two parallel streams of fluid with differing velocities merge, resulting in coherent vortices whose evolution is governed by the natural or forced instabilities upstream of their conjunction. In the hydraulic jump, a recirculating roller region with negative velocity is situated above an impinging flow with positive velocity, and large local instabilities induced through the self-forcing action of recirculation and toe oscillations result in coherent vortices. Evidence of coherent vortical structures in mixing layers of free-shear flows is well documented (see e.g. Brown and Roshko, 1974; Hussain, 1986), but very few experimental observations exist for the classic hydraulic jump. The bulk of literature on coherent vortical structures in the hydraulic jump is based on qualitative visualization of primary spanwise vortices in high ($Fr > 2$) Froude number

jumps (Mossa and Tolve, 1998; Zhang et al., 2012), or, at most, experiments at low ($Fr <$ 2) Froude number with the addition of point velocity measurements (Misra et al., 2008; Rodríguez-Rodríguez et al., 2011).

Advances in computer power have made the numerical study of hydraulic jumps a viable companion to laboratory investigations. The first simulations captured free surface fluctuations in the liquid phase but ignored the contributions of air entrainment outright (Liu and Drewes, 1994; Chippada et al., 1994). Later, multiphase simulations implemented a phenomenological subgrid model that determined air entrainment based on turbulent fluctuations at the free surface (Souders and Hirt, 2004; Gonzalez and Bombardelli, 2005). These models, in line with numerous others (e.g. Carvalho et al., 2008; Abbaspour et al., 2009), have shown that Reynolds-Averaged Navier-Stokes (RANS) simulations with two-equation turbulence models, in combination with a Volume of Fluid (VOF) method for resolving the free surface, can capture the formation of the jump. Quantitative numerical results of void fraction distributions in a hydraulic jump have recently been produced using a subgrid air entrainment model (Ma et al., 2011; Cheng and Chen, 2011). However, these studies did not resolve the physical processes of bubble entrainment and breakup that dictate the void fraction profile, i.e., air entrainment was simulated based on inputs from experimental data or empirical relationships. Attempts to reproduce air entrainment directly through numerical simulation have been thus far unsuccessful (Lubin et al., 2009). This limitation restricts use of numerical simulations to instances where experimental verification of bubble diameters is readily available, which is not often the case.

A recent review of the state of aerated flow numerical simulations revealed a significant deficiency in model validation and a lack of valuable insights into relevant flow dynamics (Chanson, 2013). The aim of this paper is to present fully validated simulations of hydraulic jumps that inherently predict air-water flow characteristics without the use of experimental calibration. We also present the flow physics in terms of vortical structures observed in 3D numerical simulations, and their contributions to air-bubble transport. This paper is organized as follows. In Section 3.2, the numerical

technique is described, the time dependence of the hydraulic jump is explored to determine an appropriate sampling rate and time for the numerical simulations, and a grid analysis is conducted to establish an appropriate computational cell size for capturing simulated air entrainment. In Section 3.3, validations of time-averaged velocity profiles, void fraction profiles, and bubble diameter are presented. Section 3.4 explores the flow physics in more detail by showing new evidence of vortex merging, the existence of streamwise vortices, the relationship between toe fluctuations and vortex evolution, and the similarities and differences between the hydraulic jump and a classic mixing layer. Conclusions are offered in Section 3.5.

3.2. Problem setup and numerical methodology

3.2.1. Problem setup

Our simulation conditions were designed to model the experiment of Murzyn et al. (2005). A representation of their experimental setup is shown in Figure 3.1. A recirculating laboratory flume 12m long, 0.3m wide, and 0.4m high was used to create a quasi stable hydraulic jump. A sluice gate controlled the depth of the impinging jet, d, while a weir near the downstream outlet stabilized the jump and controlled the tailwater depth, d_{tw}. An RBI dual-tip probe optical phase-detection instrument was used to measure void fractions at various depths and distances downstream from the foot of the jump. The inflow exhibited a boundary layer thickness ranging from $0.2d - 0.4d$, characterizing the jump as partially developed. No free surface aeration occurred upstream of the impingement point, and the incident flow was free of bubbles. The velocity of the upstream jet, U_o, and d were adjusted to result in a variation of low Froude number jumps. The measurements at $Fr = 2.43$, 3.65, and 4.82 are used for comparison in the present study.

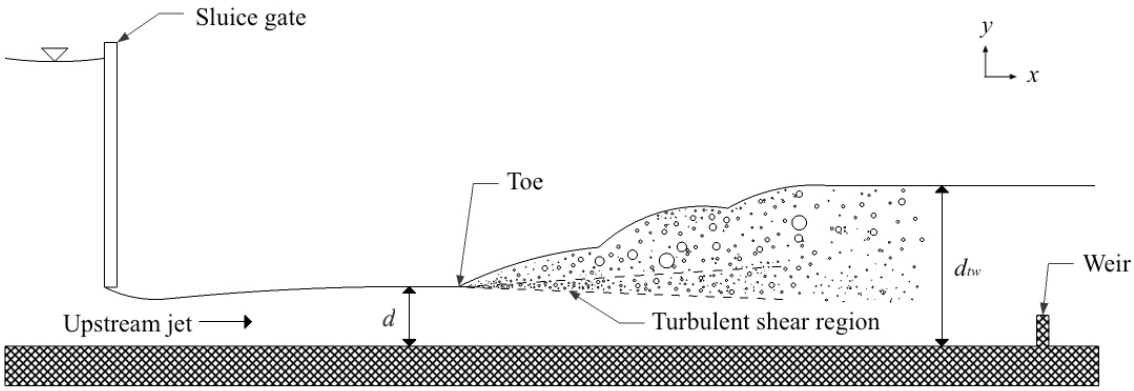

Figure 3.1. Representation of the experimental set-up of Murzyn et al. (2005). Not to scale.

3.2.2. Numerical methodology

Numerical simulations are carried out using OpenFOAM®, an open source computational fluid dynamics software package. Two and three-dimensional (2D and 3D) simulations are conducted assuming an unsteady, turbulent, incompressible flow. The evolution of the free surface is modeled using *interFoam*, a VOF solver designed for two immiscible, isothermal, interpenetrating fluids (OpenFOAM, 2012). The hydraulic jump is a complex problem to simulate due to the highly transient behavior of the toe and the turbulent entrainment and subsequent shearing of large air pockets in the roller. The *interFoam* solver has been shown to accurately resolve the physics of air entrainment and hydrodynamic breakup processes in a variety of fluid phenomena (Deshpande et al., 2012b). To our knowledge, the present study is the first application of the solver to investigate the air entrainment characteristics of the hydraulic jump.

In the VOF approach, a single set of momentum equations is shared by the two phases, which are mathematically treated as a single continuum medium. The volume of fluid in each computational cell is tracked by an indicator function, γ, and the free surface evolution is governed by a transport equation for γ in cells that contain a phase interface. The governing equations take the form

$$\nabla \cdot \boldsymbol{u} = 0, \tag{3.1}$$

$$\frac{\partial(\rho \boldsymbol{u})}{\partial t} + \nabla \cdot (\rho \boldsymbol{u}\boldsymbol{u}) = -\nabla p + \rho \boldsymbol{g} + \nabla \cdot \boldsymbol{\tau} + \sigma \kappa \nabla \gamma, \tag{3.2}$$

$$\frac{\partial \gamma}{\partial t} + \nabla \cdot (\gamma \boldsymbol{u}) + \nabla \cdot \left(\boldsymbol{u}_c \gamma (1 - \gamma)\right) = 0, \tag{3.3}$$

where $\boldsymbol{u}$ is the fluid velocity vector, ρ is the fluid density, p is the scalar pressure, $\boldsymbol{\tau}$ is the viscous stress tensor given as $\tau = 2\mu \boldsymbol{S} = 2\mu(0.5[(\nabla \boldsymbol{u}) + (\nabla \boldsymbol{u})^{T}])$ where μ is the dynamic viscosity, σ is the surface tension, κ is the mean curvature of the free surface, γ indicates the volume fraction of fluid in each computational cell, and $\boldsymbol{u}_c$ is an artificial "compressive velocity", which acts normal to the phase interface to counter numerical diffusion (Rusche, 2002; OpenFOAM, 2012).

The fluid domain consists of a mixture of phases, where each computational cell contains a phase fraction between $\gamma = 1$, indicating the continuous fluid (liquid, $\varphi = 0$), and $\gamma = 0$, indicating the dispersed fluid (gas, $\varphi = 1$). The fluid properties ρ and μ are calculated based on the weighted contributions of the volume fraction of respective fluid as (Rusche, 2002)

$$\rho = \rho_l \gamma + \rho_g (1 - \gamma), \tag{3.4}$$

$$\mu = \mu_l \gamma + \mu_g (1 - \gamma), \tag{3.5}$$

Surface tension forces at the interface are represented using the continuum-surface-force model developed by Brackbill et al. (1992). Curvature is computed based on the volume fraction gradient. The model has shown good performance in flows where surface tension and bubble dynamics are dominant (Krishna and van Baten, 1999; Deshpande et al., 2012b). To capture the appropriate curvature and ensure that surface

tension forces are well represented in the flow, computational cells must be of a smaller scale than the average bubble diameter. The surface tension coefficient σ was not reported in Murzyn et al. (2005), thus an investigation of void fraction profiles with σ = 0.07 N/m and σ = 0.047 N/m was carried out. A negligible difference in void fraction profiles was observed, and a value of σ = 0.07 N/m was maintained for all simulations.

Numerical simulations of the hydraulic jump utilizing a two equation k-ε formulation have shown good agreement with laboratory measurements (Liu and Drewes, 1994; Zhao et al. 2004; Carvalho et al., 2008). To apply this approach, Eqs. 1 and 2 are Reynolds averaged, resulting in a Reynolds stress that represents the transport and dissipation of energy due to turbulence. Next, μ is replaced by an effective viscosity, μ_{eff}, where

$$\mu_{eff} = \mu + \mu_t, \tag{3.6}$$

and μ_t is the turbulent eddy viscosity. Eddy viscosity is then related to turbulent kinetic energy, k, and energy dissipation, ε, through a constitutive relationship

$$\mu_t = \rho C_\mu \frac{k^2}{\epsilon}, \tag{3.7}$$

where C_μ is a variable model parameter sensitized to the flow using the following relations (Shih et al., 1995):

$$C_\mu = \frac{1}{4+A_s U^* \frac{k}{\epsilon}}, \quad A_s = \sqrt{6}\cos(\phi), \quad \phi = \frac{1}{3}\arccos\left(\sqrt{6}W\right), \quad W = \frac{S_{ij}S_{jk}S_{ki}}{\tilde{S}^3},$$

$$\tilde{S} = \sqrt{S_{ij}S_{ij}}, \quad U^* = \sqrt{S_{ij}S_{ij}+\Omega_{ij}\Omega_{ij}}, \quad \Omega_{ij} = \frac{1}{2}\left(\frac{\partial u_i}{\partial x_j} - \frac{\partial u_j}{\partial x_i}\right).$$

The transport of k and ε are computed using

$$\frac{\partial(\rho k)}{\partial t} + \frac{\partial(\rho k \boldsymbol{u})}{\partial \boldsymbol{x}} = \frac{\partial}{\partial \boldsymbol{x}}\left[\left(\mu + \frac{\mu_t}{\sigma_k}\right)\frac{\partial k}{\partial \boldsymbol{x}}\right] + G_k - \rho\epsilon, \tag{3.8}$$

$$\frac{\partial(\rho\epsilon)}{\partial t} + \frac{\partial(\rho\epsilon \boldsymbol{u})}{\partial \boldsymbol{x}} = \frac{\partial}{\partial \boldsymbol{x}}\left[\left(\mu + \frac{\mu_t}{\sigma_\epsilon}\right)\frac{\partial \epsilon}{\partial \boldsymbol{x}}\right] + \rho C_1 \boldsymbol{S}\epsilon - \rho C_2 \frac{\epsilon^2}{k + \sqrt{\nu\epsilon}}, \tag{3.9}$$

where σ_k and σ_ε are model constants equal to 1 and 1.2, respectively, G_k represents turbulent kinetic energy generation from the mean velocity gradients,

$$G_k = 2\mu_t S_{ij} S_{ij}, \tag{3.10}$$

C_1 is a variable model parameter,

$$C_1 = \max\left[0.43, \frac{\eta}{\eta + 5}\right], \ \eta = \frac{k}{\epsilon}\sqrt{2 S_{ij} S_{ij}}, \tag{3.11}$$

C_2 is a model constant equal to 1.9, and ν is the kinematic viscosity (OpenFOAM, 2012). In contrast to the standard k-ε closure scheme, the realizable k-ε scheme ensures the positivity of normal stresses by sensitizing C_μ to the mean strain rate, mean rotation rates, and the turbulence fields in a matter consistent with the physics of turbulent flows. The realizable scheme exhibits improved performance over the standard k-ε scheme in shear flows (Zhu and Shih, 1994; Kim et al., 1999), recirculating flows (Qian et al., 2009), and when air bubble entrainment is a relevant flow characteristic (Zidouni et al. 2010).

To discretize the transient terms, a Crank-Nicolson scheme was used with an off-centering coefficient of 0.5 for all but the smallest grid size, where a coefficient of 0.9 was employed to improve the numerical stability of the simulations as cell size was reduced. Spatial discretization was carried out using a second order, Gauss linear discretization scheme. Cells containing a volume fraction interface are discretized with a second order blended difference scheme and a van Leer limiter (Rusche, 2002; OpenFOAM, 2012). The Pressure Implicit Splitting of Operators (PISO) algorithm was used for coupling the pressure and velocity, while the time step was limited by a

maximum Courant number of 0.5. The discretization scheme maintained a second order global accuracy.

3.2.3. Simulation conditions

As an example, the computational domain and grid for Fr = 4.82 are shown in Figure 3.2. Boundary conditions are given in Eqs. 3.12-3.17. On the left hand boundary (Ω_{il}), an inlet flow of depth d was set to match experimental conditions for each Fr jump (d = 0.046 m, 0.032 m, and 0.021 m for Fr = 2.43, 3.65, and 4.82, respectively), a wall was placed above the inlet up to 0.2 m to simulate a sluice gate (Ω_{wl}), and the remaining depth was open to the atmosphere (Ω_{ol}). The top (Ω_{ot}) and right (Ω_{or}) boundaries were also open to the atmosphere. The bottom boundary was a no-slip wall (Ω_{wb}), and an overshot weir was placed near the downstream end of the mesh to set the tailwater elevation. The entire domain was bounded by a depth of 0.4 m and a length of 2.6 m for the Fr = 2.43 simulation, 2.9 m for the Fr = 3.65 simulation, and 2.1 m for the Fr = 4.82 simulation. The initial grid was a structured, uniform mesh. Successive, local grid refinements were made from the left hand boundary to a minimum of 10d past the final measurement location. The goal of the present study is to capture the air entrainment characteristics at the toe and subsequent bubble transport downstream. The numerical domain is optimized to force a jump to occur in the first 0.5 m of the domain, ensuring all air entrainment, bubble breakup, and bubble transport corresponding with the experimental measurement locations remain fully contained in the finest mesh. Within this region, the first grid nodes off the bottom wall are within the log layer for all cases.

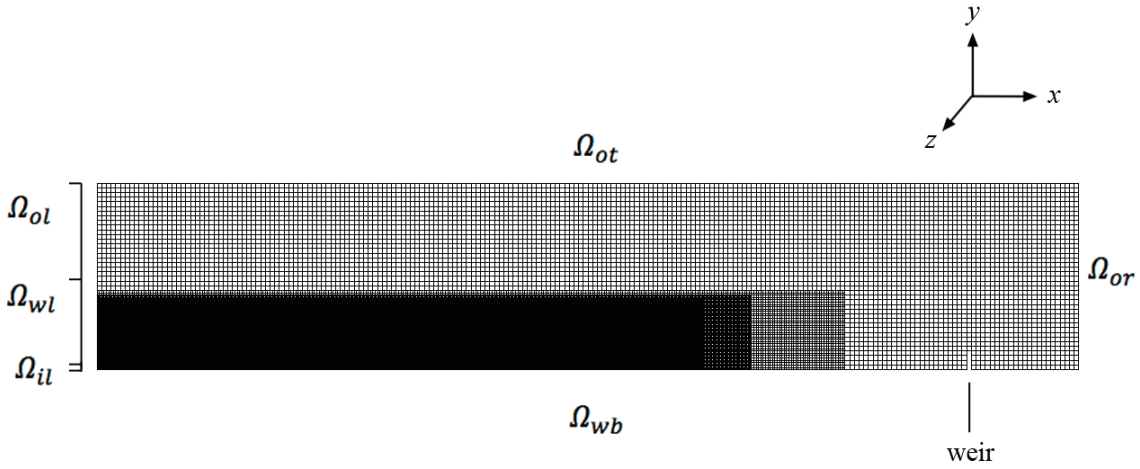

Figure 3.2. 2D computational grid for the case of $Fr = 4.82$.

$$\Omega_{il}: \quad \boldsymbol{n} \cdot \nabla p = -(\boldsymbol{n} \cdot \nabla \rho)\boldsymbol{g} \cdot \boldsymbol{x}; \quad \boldsymbol{u} = (U_o, 0); \quad \gamma = 1; \tag{3.12}$$

$$\Omega_{wl}: \quad \boldsymbol{n} \cdot \nabla p = -(\boldsymbol{n} \cdot \nabla \rho)\boldsymbol{g} \cdot \boldsymbol{x}; \quad \boldsymbol{u} = (0,0); \quad \boldsymbol{n} \cdot \nabla \gamma = 0; \tag{3.13}$$

$$\Omega_{ol}: \quad \boldsymbol{n} \cdot \nabla p = 0; \quad \boldsymbol{n} \cdot \nabla \boldsymbol{u} = 0; \quad \boldsymbol{n} \cdot \nabla \gamma = 0; \tag{3.14}$$

$$\Omega_{ot}: \quad p + \rho \boldsymbol{u}^2 = 0; \quad \boldsymbol{n} \cdot \nabla \boldsymbol{u} = 0; \quad \boldsymbol{n} \cdot \nabla \gamma = 0; \tag{3.15}$$

$$\Omega_{or}: \quad \boldsymbol{n} \cdot \nabla p = 0; \quad \boldsymbol{n} \cdot \nabla \boldsymbol{u} = 0; \quad \boldsymbol{n} \cdot \nabla \gamma = 0; \tag{3.16}$$

$$\Omega_{wb}: \quad \boldsymbol{n} \cdot \nabla p = -(\boldsymbol{n} \cdot \nabla \rho)\boldsymbol{g} \cdot \boldsymbol{x}; \quad \boldsymbol{u} = (0,0); \quad \boldsymbol{n} \cdot \nabla \gamma = 0; \tag{3.17}$$

A constant velocity, U_o, was prescribed at the flow inlet to match experimental conditions. A constant velocity, U_o, was prescribed at the flow inlet to match experimental conditions. The upstream jet traveled approximately 15-20d downstream from the inlet before encountering the tailwater, which was a sufficient length to ensure the velocity profile developed a boundary layer thickness of between 0.2d and 0.4d, and could be characterized as partially developed. All walls were modeled as no-slip, and outlets were prescribed a zero gradient velocity condition, $\boldsymbol{n} \cdot \nabla \boldsymbol{u} = 0$, where $\boldsymbol{n}$ is the normal surface vector. Total pressure at the top outlet, $p + \rho \boldsymbol{u}^2$, was set equal to 0 and p was calculated from $\boldsymbol{u}$ on the boundary. Walls and outlets were prescribed with a

buoyant pressure condition. Turbulence parameters k and ε were modeled using a zero gradient condition at all outlets while solid wall boundaries were modeled using a logarithmic wall function. Values of k and ε at the inlet were assigned assuming 5% turbulence intensity and a turbulent length scale of 10% of the inlet depth.

A 3D simulation was also conducted for $Fr = 4.82$. The front and back planes, Ω_{fp} and Ω_{bp}, respectively, were modeled as a free-slip surface. This treatment is identical to Eq. (3.14) for scalars and tangential components of vectors, while the normal components of vectors are set equal to 0. The grid was similar to Figure 3.2 with a width of 0.1 m extended in the z direction. This width was chosen to model the interior of the experimental domain, where side wall effects are negligible (Chanson, 2007a). The mean motion of bubbles is highly influenced by spanwise vortices, which are constrained by the free surface, and to a small degree, streamwise vortices. Domain boundaries were chosen to ensure spanwise vortices are fully resolved in both 2D and 3D simulations, and streamwise vortex pairs are fully resolved in the 3D simulation.

3.2.4. Time dependence

The void fraction measurements of Murzyn et al. (2005) were obtained using optical fiber probes with a sampling rate of 1 MHz and a sampling time of 120 s. Though a range of sampling rates and times have been reported in the literature, Chanson and Brattberg (2000) found no difference in air concentration distributions at sampling times longer than 10 s. Computational restraints allowed for a maximum sampling rate of 20 Hz, thus the sampling time dependence of the simulations was analyzed to find a balance between computational cost and modeling accuracy. The integration of time-averaged void fraction over depth, i.e. $\Sigma\bar{\varphi}_j\Delta y_{ji}$, was chosen as the principal indicator of convergence, where y indicates the vertical position, i represents the horizontal index, j represents the vertical index, and $\bar{\varphi}$ is the time-averaged void fraction. A vertical integration is representative of the average amount of air entrained into the flow over time, and therefore serves as a gauge of accuracy for air entrainment.

A visual observation shows the average void fraction profile approaching a constant shape after just 1 s of sampling time at 20 Hz (Figure 3.3). To quantify average air entrainment from our simulations, vertical data points were obtained at four downstream horizontal locations matching those of Murzyn et al. (2005). A void fraction of 0.5 was assumed to be the location of the free surface and served as a cutoff for depth integration. The value of $\Sigma\varphi_j\Delta y_{ji}$ for each 2D simulation was obtained every 0.05 s, and a time average was carried out over 20 s. The relative error in $\Sigma\bar{\varphi}_j\Delta y_{ji}$ after 5 s, 10 s, and 15 s of time averaging was computed using $\Sigma\bar{\varphi}_j\Delta y_{ji}$ obtained after a 20 s sampling time. For the $Fr = 4.82$ case, the relative error after 5 s, 10 s, and 15 s sampling times was 0.076, 0.054, and 0.007, respectively. The relative error in average entrained air after 15 s of sampling time showed a similar trend for all Fr jumps, thus a sampling time of 15 s is used in the following analyses. A 15 s sampling time represents 7.5 – 30 toe pulsations for hydraulic jumps in the range of Froude number and Reynolds number considered in this study (Chanson and Gualtieri, 2008).

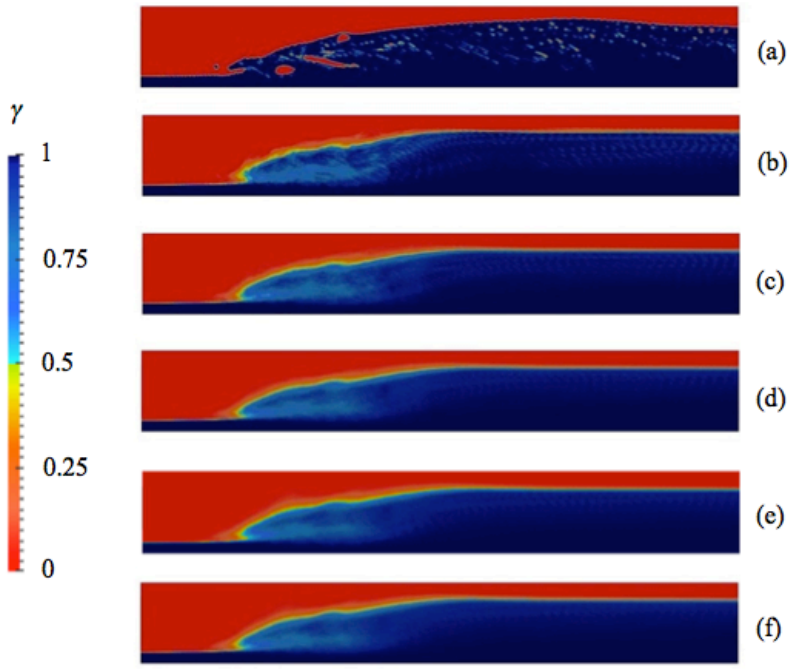

Figure 3.3. Time-averaged volume fraction field for a 2D simulation of $Fr = 4.82$ after 0 s (a), 1 s (b), 5 s (c), 10 s (d), 15 s (e), and 20 s (f).

3.2.5. Grid analysis

Void fraction dependence on cell density was measured at each grid refinement level. The coarsest grid was a structured, uniform mesh with cells of length 10 mm, roughly $0.3d - 0.5d$. At subsequent refinement levels the cell length, Δx, was reduced by half in the region of interest (Figure 3.2). Again, $\Sigma\bar{\varphi}_j\Delta y_{ji}$ was chosen as the principal indicator of convergence, and relative error was computed with respect to the total entrained air obtained by Murzyn et al. (2005). The results are listed in Table 3.1. A relative error of less than 10% of experimental values was deemed acceptable for purposes of evaluation. This was obtained at Δx = 1.25 mm for 2D simulations and at Δx = 2.5 mm for the 3D simulation. In the Fr = 4.82 2D simulation, a decrease in Δx from 1.25 mm to 0.625 mm lowered the relative error from 3.7% to 1.0%, but increased the computational time substantially by a factor of 29. Therefore, we have chosen to use Δx = 1.25 mm for all cases. At this grid size, relative error in the 3D simulation was 35% of the relative error from the 2D simulation, while the computational time was increased by a factor of 341.

A significant improvement is seen in 2D simulations when the grid size is reduced from Δx = 2.5 mm to Δx = 1.25 mm (Grid 4). At this grid size, the largest bubbles in the flow are represented by at least eight computational cells. The resolution at this bubble diameter to grid ratio is sufficient to capture bubble deformations caused by the interaction of vortices and the bubble interface (Tomiyama et al., 1993). These interactions contribute to the potential breakup and trajectories of the bubbles. Within the shear layer of the jump, the largest bubbles are found near the toe, and vary from 10 – 20 mm in diameter (Murzyn et al., 2005). Bubbles are most susceptible to breakup in this high shear region, and their fate influences the overall bubble field downstream. A bubble diameter to grid size ratio of eight is achieved for 10 mm bubbles with Grid 4. When this occurs, the largest bubbles are sheared more effectively at the toe, and their internal flow field is sufficiently resolved, improving their mean motion within the shear layer. Smaller satellite bubbles produced during breakup are not effectively resolved on coarser grids. Compared with coarser grids, Grid 4 shows improved void fractions near

the toe due to better resolution of small bubbles produced during breakup. The transport and turbulent dispersion of these small bubbles also significantly improved the simulation of average entrained air downstream.

Table 3.1. Relative error in average void fractions, calculated with respect to the time-averaged void fractions of Murzyn et al. (2005). CPU time is obtained by multiplying the total simulation time by the number of processors.

Grid	Max Δx (m)	Grid size				CPU time (h)				Relative error			
		Fr = 2.43	3.65	4.82 2D	4.82 3D	2.43	3.65	4.82 2D	4.82 3D	2.43	3.65	4.82 2D	4.82 3D
1	0.01	2.6E+04	2.3E+4	1.7E+4	8.4E+4	0.3	0.6	0.5	1.9	0.622	0.422	0.689	0.391
2	0.005	5.7E+04	6.0E+4	4.3E+4	2.7E+5	2.1	1.8	1.2	33	0.428	0.394	0.511	0.240
3	0.0025	1.4E+05	1.6E+5	1.2E+5	1.5E+6	13	13	11	1,170	0.344	0.359	0.396	0.081
4	0.00125	4.2E+05	4.7E+5	3.7E+5	1.0E+7	349	388	289	98,496	0.013	0.064	0.037	0.013
5	0.000625			1.1E+6				8,361				0.010	

3.3. Air and water flow characteristics

In this section, the 2D and 3D numerical results are presented and compared with the experimental results of Murzyn et al. (2005). Ideally, validation of simulated aerated flows should include comparisons of velocity, void fraction, turbulence intensity, and bubble characteristics with experimental measurements (Chanson, 2013). For all simulations, average void fraction and bubble size are obtained from the volume fraction field. To the authors' knowledge, the validation of bubble diameter simulated without the use of a subgrid bubble model is the first reported in the literature for a hydraulic jump. Based on the available experimental data, a comparison of turbulence intensity and mean velocity is not possible. Instead, we compare some mean velocity characteristics with those obtained experimentally from similar *Fr* jumps.

3.3.1. Velocity

The mean horizontal velocity flow structure for $Fr = 4.82$ 3D is shown in Figure 3.4. For the 3D validation all values were obtained along an *x*-*y* plane located centered in the middle of the numerical domain (z = 0.05 m). The downstream measurement location is given by $x\text{-}x_{toe}$, where x_{toe} is the average location of the toe, and *x* is the downstream location. Velocity profiles compare favorably to the velocity field of similar *Fr* jumps obtained experimentally (Liu et al., 2004; Lin et al., 2012). Maximum velocity is observed at the toe and remains slightly above the wall moving downstream. The shear region begins immediately above the location of maximum velocity, denoted by the dotted black line, and extends vertically to the dotted white line, which denotes the minimum positive horizontal velocity ($u = 0$ in the roller).

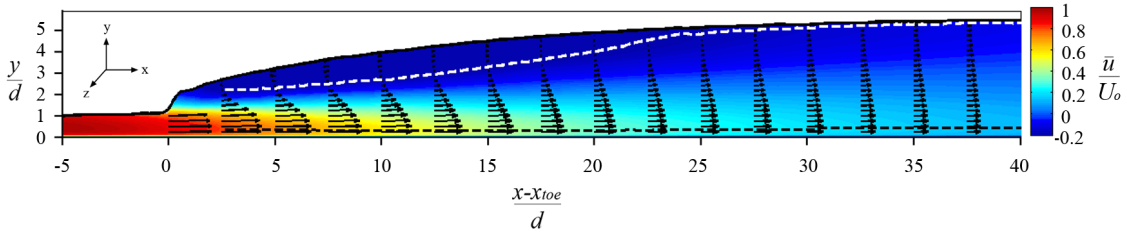

Figure 3.4. Color contours representing the average horizontal velocity for $Fr = 4.82$ 3D beneath the mean free surface ($\bar{\gamma} = 0.5$). White and black dotted lines represent the location of minimum and maximum mean horizontal velocity, respectively, and arrows depict (u, v) velocity vectors.

The velocity profile within a hydraulic jump is similar to a wall jet (Rajaratnam, 1965), described with the empirically calibrated equation (Lin et al, 2012)

$$\frac{\boldsymbol{u}}{\boldsymbol{u_{max}}} = 2.3\left(\frac{y}{b_w}\right)^{0.42}\left[1\text{-erf}\left(0.886\ \frac{y}{b_w}\right)\right], \tag{3.18}$$

where erf is the error function, $\boldsymbol{u_{max}}$ is the maximum velocity at the given downstream location, y is the vertical location, and b_w is the half width of the wall jet, or the height at $\boldsymbol{u} = \boldsymbol{u_{max}}/2$. A comparison of all simulated data with that of the similarity profile (Eq. 3.18) shows a similar shape in both the lower and upper shear layer (Figure 3.5). Scatter about the theory line is consistent with that seen in experiments (e.g. Fig. 20 of Lin et al., 2012; Fig. 3.18 of Murzyn and Chanson, 2007).

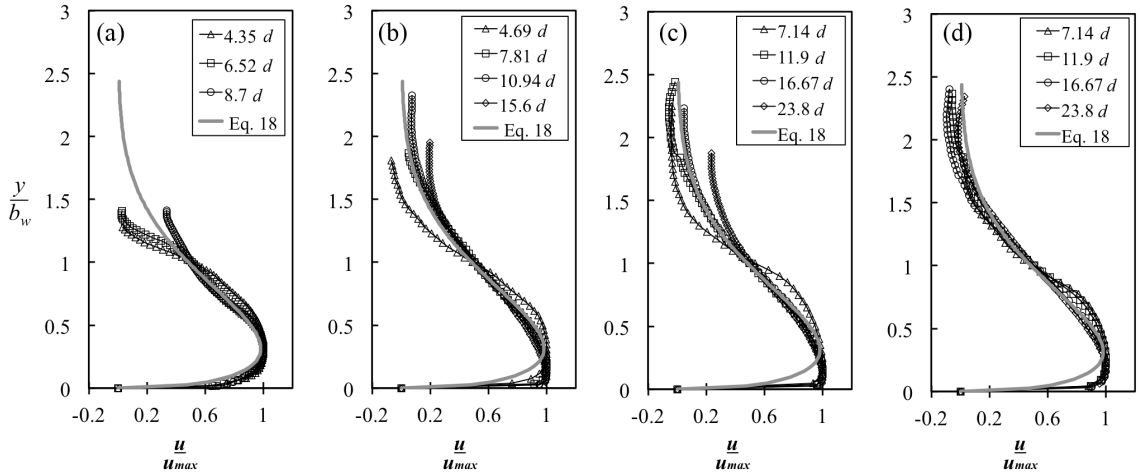

Figure 3.5. Time-averaged velocity profile compared to a wall-jet similarity solution for $Fr = 2.43$ (a), $Fr = 3.65$ (b), $Fr = 4.82$ 2D (c), and $Fr = 4.82$ 3D (d).

Maximum velocity decays exponentially with increasing streamwise distance from the toe (Figure 3.6). Simulation data follows the exponential relationship

$$\frac{\boldsymbol{u}}{\boldsymbol{u_{max}}} = \exp\left(-A\frac{x-x_{toe}}{d}\right) \tag{3.16}$$

with $A = 0.043$ for 2D data, and $A = 0.030$ for 3D data, in agreement with the experimentally observed $A = 0.028$ for jumps with $Fr > 5$ (Chanson, 2010). The 2D numerical data exhibit a similar scatter about the exponential trend line as lower Fr jumps observed in experiments (Fig. 3.19 of Murzyn and Chanson, 2007; Fig. 11 of Chanson, 2010). The maximum velocity in 3D for $Fr = 4.82$ is approximately 10% higher than 2D at comparable locations within the shear layer. This is thought to be attributable to resolution of 3D vortex dynamics, as described in Section 3.4.

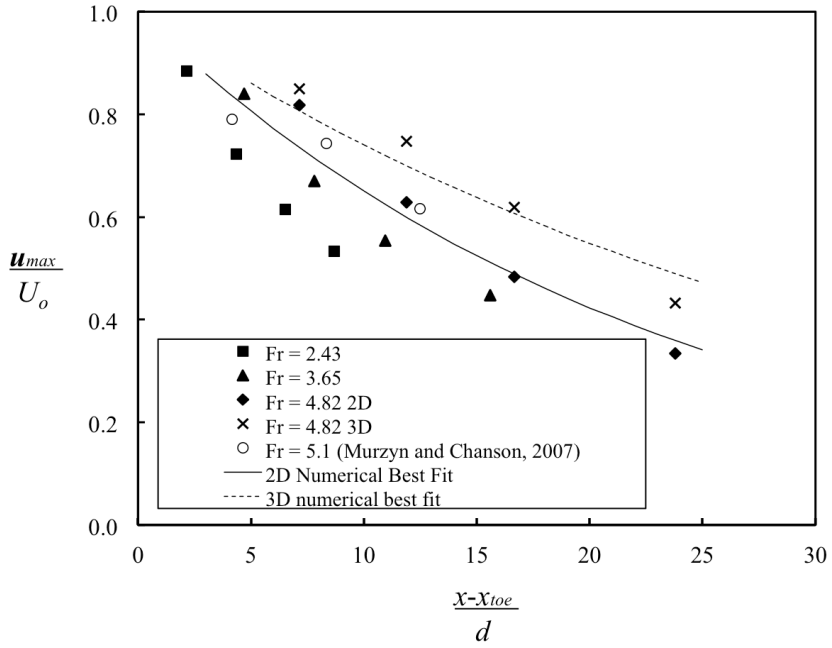

Figure 3.6. Maximum velocity in the shear layer, normalized by upstream jet velocity, at dimensionless downstream locations.

3.3.2. Void fraction

The numerical simulations were able to capture the entrainment of air at the toe, the shearing of air pockets in the roller, the rise of large bubbles out of the flow, and the transport of small bubbles downstream. A quantitative representation of average void fraction is shown in Figs. 3.7-3.9. Each plot shows simulated and experimental time-averaged void fractions as a function of depth normalized by the upstream jet depth.

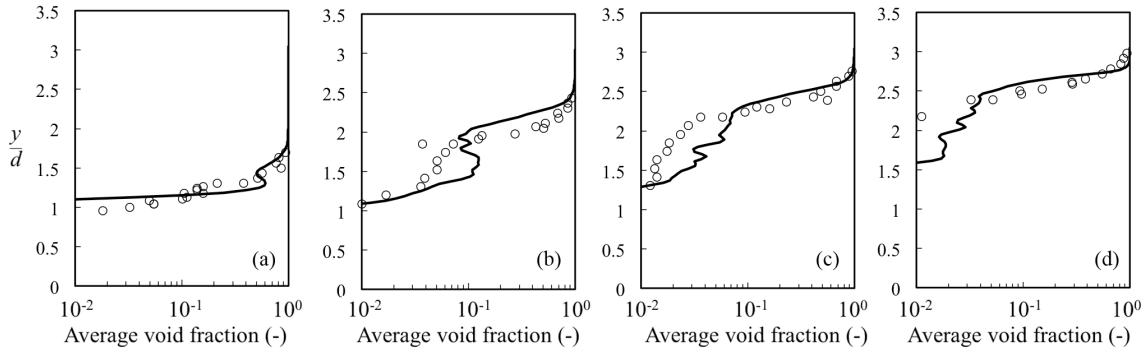

Figure 3.7. Average void fraction profiles for $Fr = 2.43$ at $x\text{-}x_{toe} = 2.17d$ (a), $4.35d$ (b), $6.52d$ (c), and $8.7d$ (d). '○' denotes experimental average void fraction (Murzyn, 2013); '—' denotes simulated average void fraction.

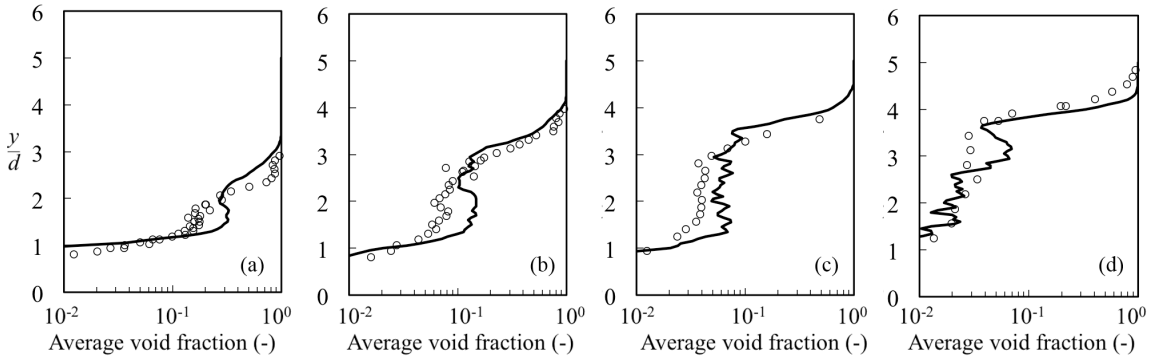

Figure 3.8. Average void fraction profiles for $Fr = 3.65$ at $x\text{-}x_{toe} = 4.69d$ (a), $7.81d$ (b), $10.94d$ (c), and $15.6d$ (d). Symbols see Figure 3.7.

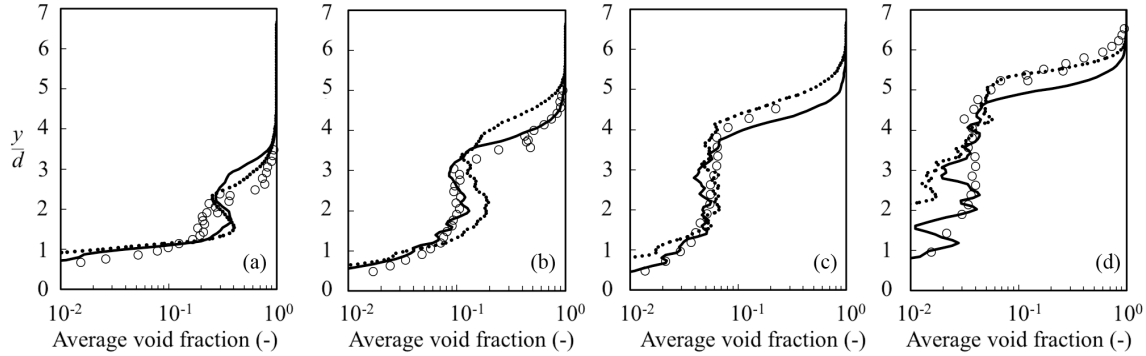

Figure 3.9. Average void fraction profiles for $Fr = 4.82$ at $x\text{-}x_{toe} = 7.14d$ (a), $11.9d$ (b), $16.67d$ (c), and $23.8d$ (d). '○' denotes experimental average void fraction (Murzyn, 2013); '----' denotes 2D simulated average void fraction; '—' denotes 3D simulated average void fraction.

Ascending at each location a rise in void fraction leads to a maximum air concentration within the shear region, above which void fraction begins to decrease. The shape is similar to a Gaussian solution to the advection-diffusion equation for the void fraction as described by Chanson (1996). The shape is more pronounced for higher *Fr* jumps, where air entrainment at the toe is increased. The simulation tends to predict higher void fractions in the shear region near the toe of the jump (Figures 3.7-3.9, a and b). The turbulent action of the shear layer leads to instantaneous bubble breakup and coalescence, characterized by a continuous deformation of a moving interface. Regions exhibiting this flow structure are susceptible to higher uncertainties in both experiments and simulations. Despite the numerical challenges, average simulated air concentration rarely deviates greater than 10% from experiments. Moving downstream, void fractions are nearly identical in the turbulent shear region, indicating an accurate representation of bubble transport in the downstream turbulent shear region (Figures 3.7-3.9, c and d).

In the upper layer of the jump, breaking waves and turbulent ejections of fluid are the dominating mechanisms of air entrainment, and the void fraction profile increases sharply to $\varphi = 1$. Nearly all simulation locations capture this abrupt increase at an elevation matching the experiments. Near the toe of the jump, the simulation tends to over predict the average free surface elevation by $0.2d - 0.5d$ for higher *Fr* number jumps (Figures 3.8-3.9, a). These increased elevations tend to match locations with higher void fraction in the shear layer, indicating the presence of air in the shear layer has a bulking effect on the flow. Moving downstream, the simulation is accurate in capturing the upper void fraction profile, where free surface fluctuations are severely suppressed.

The longitudinal structure of average void fraction compares favorably with experimental values (Figures 3.10 and 3.11). The elevation of maximum void fraction, y_{Cmax}, versus horizontal location within the jump shows a linear relation with a gradient of 0.112, in close agreement with 0.108 and 0.102 measured by Chanson and Brattberg (2000) and Murzyn et al. (2005), respectively. Maximum void fractions at each horizontal location decay with distance from the toe, in line with experiments. As *Fr* is

increased and the jump transitions from oscillating to steady, simulated C_{max} and y_{Cmax} tend to improve towards the experimental values.

Void fraction profiles and longitudinal structure for Fr = 4.82 in 2D and 3D show similarity throughout the jump. The largest improvement in 3D simulations is seen near the toe of the jump (Figure 3.9b). The 3D simulation improves void fraction predictions in the shear layer, and consequently the average free surface elevation shows improvement over the 2D simulation. The resolution of additional turbulent processes, vortex dynamics, and vortex interactions discussed in Section 3.4 is believed to be responsible for this improvement.

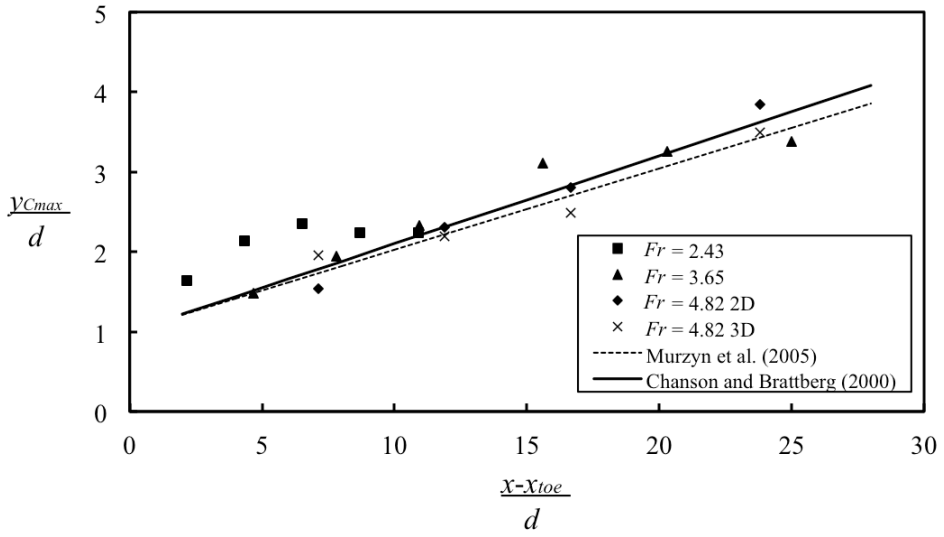

Figure 3.10. Elevation of maximum air concentration, normalized by upstream jet depth, at dimensionless downstream locations.

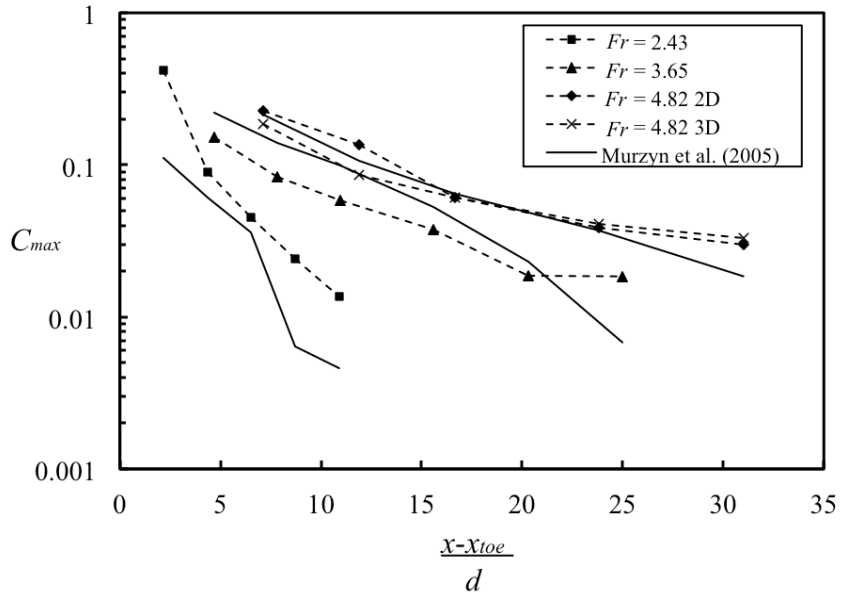

Figure 3.11. Maximum air concentration at multiple dimensionless downstream locations.

3.3.3. Bubble diameter

Validation of air entrainment is achieved through quantification of a Sauter mean diameter, i.e., the diameter of a single spherical bubble with the equivalent volume to surface area ratio of an ensemble of bubbles. A proper determination of Sauter mean diameter demands a sampling rate and sampling frequency at which an experimental apparatus can capture all relevant bubble characteristics. However, experimental sampling rates and sampling times required to achieve a stable bubble frequency count are significantly higher than what is computationally feasible (Chanson and Brattberg, 2000; Murzyn et al., 2005). A sensitivity analysis has shown that bubble count rates are underestimated for sampling rates below 5 kHz and sampling times below 30 to 40 seconds (Chanson, 2007c). Due to the unrealistic computational demands of a 5 kHz sampling rate, any numerical estimate of Sauter mean diameter will underrepresent

bubble frequency. However, some insights into bubble size can be achieved through an analysis of the instantaneous void fraction field.

The assumption by experimentalists is that bubbles within the jump are spherical and detection instrumentation intercepts a bubble along its diameter (Resch et al., 1974; Babb and Aus, 1981; Waniewski et al., 2001). To simulate this technique, a contour map of individual bubbles is created for each time step through a linear interpolation of a 2D γ field about a particular γ value. In 3D, the γ field on an x-y plane through the centerline of the domain is analyzed, as in the experimental analysis of Murzyn et al. (2005). An analysis of various contour values shows a linear interpolation about $\gamma = 0.95$ ($\varphi = 0.05\%$) produces the maximum bubble count, bubble frequency, and the proper distribution of bubble sizes while visually representing the bubble field of a hydraulic jump. Figure 3.12 shows the 2D contour field of bubbles and the 3D flow field from side and cross-section views, where bubbles are represented as isosurfaces about $\gamma = 0.95$. Larger pockets of air are present at the toe, while smaller bubbles are visible throughout the jump. A range of bubble shapes and orientations are present. To maintain consistency with experimental methods, bubbles are assumed spherical, and a closed contour line is deemed a single bubble. The projected area diameter, or the diameter of a sphere with the same projected area as the closed contour, is obtained from $d_B = (4A_B/\pi)^{0.5}$, where d_B is the projected area diameter and A_B is the 2D area of the closed contour. The diameters of all recorded bubbles are calculated in this fashion, and a Sauter mean diameter for a given vertical section of the flow is estimated using

$$d_s = \sum_j {d_b}^3 \Big/ \sum_j {d_b}^2 \quad . \tag{3.17}$$

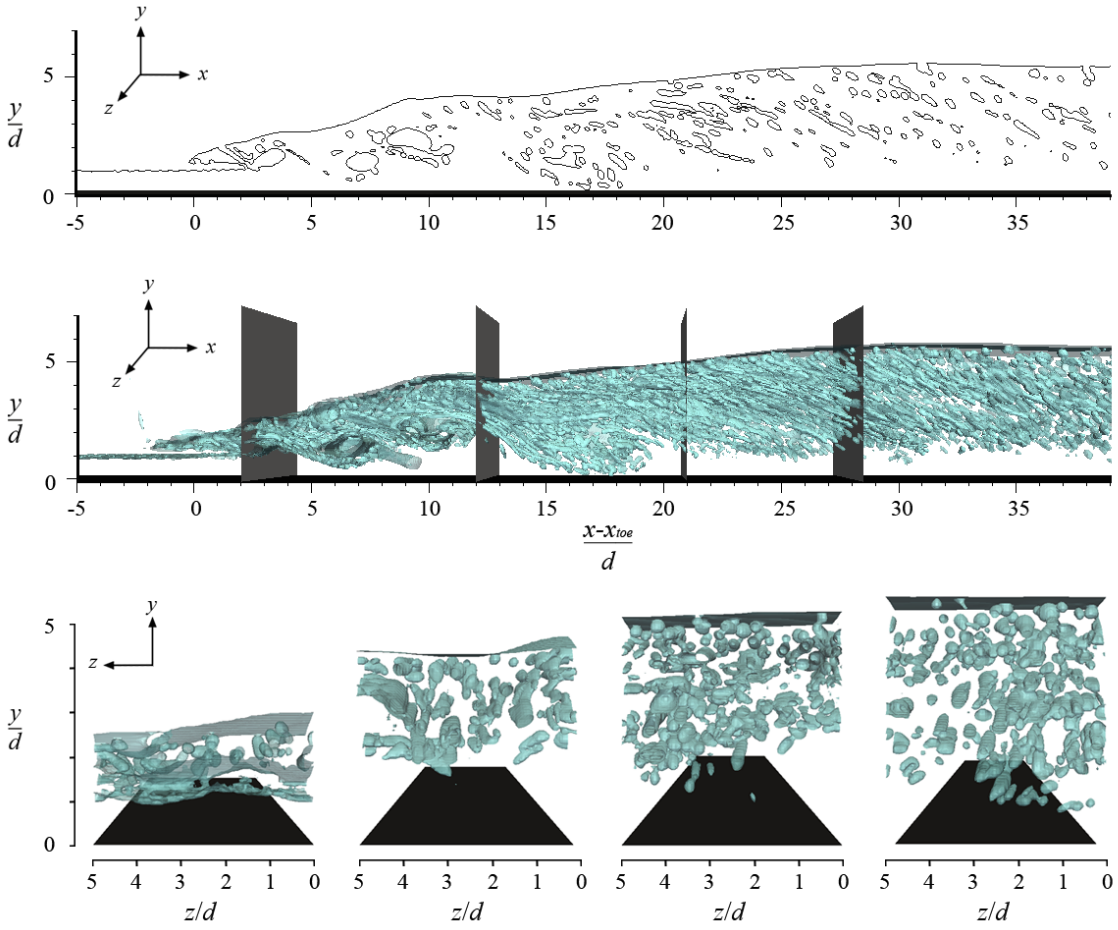

Figure 3.12. Instantaneous flow field for $Fr = 4.82$ 3D. Top: contour of the volume fraction field about a value of $\gamma = 0.95$ on an x-y plane through the channel centerline ($z/d = 2.5$). Middle: side view, with bubbles represented by 3D isosurfaces about $\gamma = 0.95$. Bottom: cross section of the flow field corresponding to each plane in the 3D view.

The vertical profiles of d_s at various downstream locations in the jump are shown in Figs. 3.13 – 3.16. Each plot shows the full range of bubbles observed in the simulation overlaid with simulated and experimental d_s as a function of depth normalized by $y_{\varphi 95}$, i.e., the vertical location of 95% air concentration ($\varphi = 0.95$). The longitudinal measurement locations are the same as those used in void fraction measurements. A contouring algorithm is used to produce an array of x and y coordinates for each distinct closed contour of φ. The centroid and area of the contour are estimated from these coordinates and each closed contour is assumed to be an independent bubble. A bubble is

associated with a particular location if the x coordinate of the centroid of the bubble falls within a ±2 cm range of the specified horizontal location.

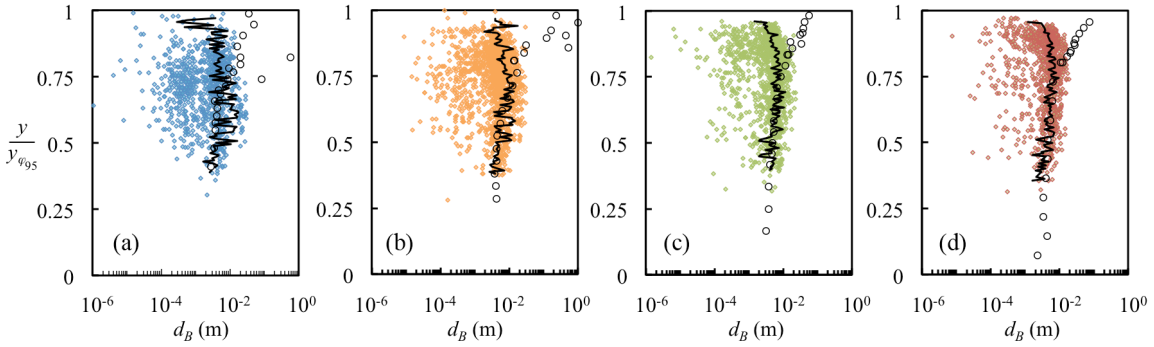

Figure 3.13. Bubble diameter for Fr = 2.43, plotted against elevation normalized by $y_{\varphi 95}$, for x-x_{toe} = 2.17d (a), 4.35d (b), 6.52d (c), and 8.7d (d). '○' denotes experimental Sauter mean diameter (Murzyn, 2013); '◆' denotes diameter of a single numerical bubble, d_b; '—' denotes numerical Sauter mean diameter, d_s.

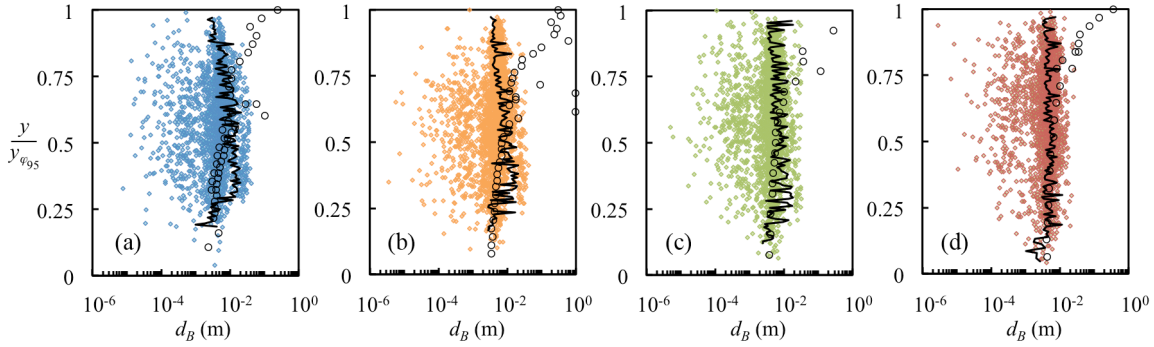

Figure 3.14. Sauter mean diameter for Fr = 3.65, plotted against elevation normalized by $y_{\varphi 95}$, at x-x_{toe} = 4.69d (a), 7.81d (b), 10.94d (c), and 15.6d (d). Symbols see Figure 3.13.

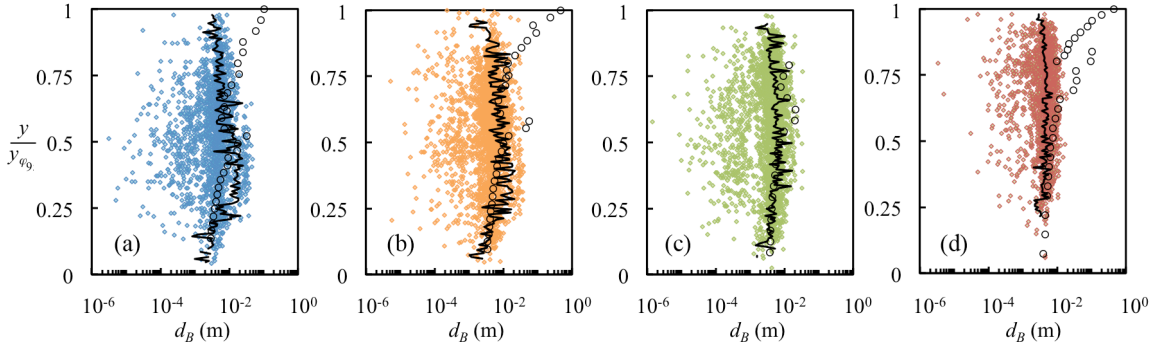

Figure 3.15. Sauter mean diameter for $Fr = 4.82$ 2D simulation, plotted against elevation normalized by $y_{\varphi 95}$, at $x\text{-}x_{toe} = 7.14d$ (a), $11.9d$ (b), $16.7d$ (c), and $23.8d$ (d). Symbols see Figure 3.13.

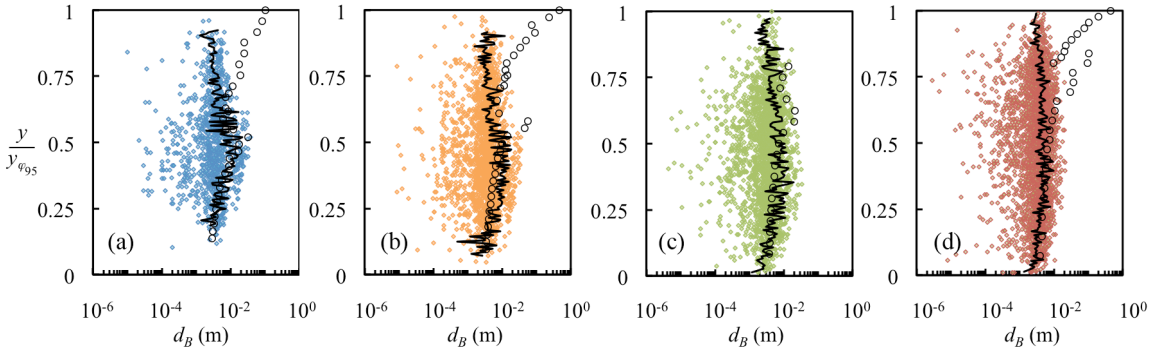

Figure 3.16. Sauter mean diameter for $Fr = 4.82$ 3D simulation, plotted against elevation normalized by $y_{\varphi 95}$, at $x\text{-}x_{toe} = 7.14d$ (a), $11.9d$ (b), $16.7d$ (c), and $23.8d$ (d). Symbols see Figure 3.13.

At the first two measurement locations, d_S shows an increase from the floor of the jump up through the shear layer ($0 < y/y_{\varphi 95} < 0.5$), qualitatively matching the trend observed in experiments for all Fr jumps. The 3D simulation exhibits the best agreement, matching the location and size of the maximum experimental d_S in the shear layer. Rising above the elevation of entrainment ($0.5 < y/y_{\varphi 95} < 0.75$), d_S decreases slightly from the maximum value in the lower shear layer. This trend is more apparent at higher Fr, and correlates closely with a similar trend in void fraction (Figures 3.7-3.9, a

and b), indicating the largest bubbles contribute most to maximum air concentrations. Bubble size measurements in this region tend to have a large uncertainty, and can vary up to an order of magnitude for repeated measurements at the same elevation (Murzyn, 2013). Scatter is observed in the simulated bubbles as well, though qualitative agreement with experiments is achieved. Both the 2D and 3D simulations produce bubbles throughout the depth of the jump, indicating the advection-diffusion of bubbles is well modeled. For Fr = 2.43 there is minimal downward vertical transport of bubbles after the initial entrainment (Figures 3.13a, 3.13b), while greater Fr jumps show a wider vertical distribution (Figures 3.14a, 3.15a, 3.16a).

At the final two measurement locations, bubble size tends to be fairly uniform throughout the depth of the jump, and closely matches experimental d_S for all simulated cases. The 2D simulations tend to underrepresent bubble counts in the lower portion of the jump (Figures 3.13c, 3.13d, 3.15d). An improvement is seen in the 3D simulation, where the vertical distribution of bubbles spans the full depth of the jump (Figures 3.16c, 3.16d), suggesting that the under representation in 2D simulations is a shortcoming of the numerical approach. The mechanisms responsible for this improvement will be discussed in Section 3.4.

Sauter mean diameter tends to diverge from experimental estimates near the free surface. In the experimental set-up, optical probes measured the percentage of air at the free surface, which included water surface fluctuations and breaking waves that may not be indicative of distinct bubbles. The contour approach based on the simulation data ensured that each bubble identified was a distinct bubble with no portion open to the atmosphere. Bubbles open to the atmosphere and breaking waves at the free surface frequently occur in an open channel flow with this level of turbulence. By including their contributions in measurements, an increase in d_s near the free surface is expected, i.e., the measurement of bubble sizes are erroneous near the free surface. Murzyn et al. (2005) did not incorporate any bubble size estimates when φ was greater than 0.25 for this reason. These results are included herein to emphasize the difficulties associated with obtaining accurate bubble size estimates near a free surface. Simulation results suggest

that Sauter mean diameter is close to uniform from the lower depths of the jump up to the free surface, with a slight increase in the shear layer near the toe, where large air pockets are entrained and sheared. Free surface fluctuations contribute to air bubble entrainment; however, we observe the Sauter mean diameter of these bubbles is not substantially larger than those in the turbulent shear region.

Bubble diameter exhibits a log normal distribution at all locations, consistent with the experimental observations of Resch et al. (1974), and similar to measurements of air chord times (Murzyn and Chanson, 2007). A wide range of bubble sizes is represented in the simulation; the smallest bubbles are seen when a single computational cell with $\gamma \approx 0.95$ is surrounded by cells with $\gamma = 1$. While the interfacial motion of these bubbles is not physically resolved, their presence is representative of the smallest bubbles in the flow, and conservation of their total air concentration is required to obtain Sauter mean diameter and average void fraction estimates. With each reduction in grid size the minimum bubble size that can be resolved decreases, and incremental decreases in Sauter mean diameter are expected. Considering the wide range of bubble sizes present in the hydraulic jump, a statistical convergence of bubble diameter may never be achieved. In this work, we have focused on capturing the breakup and transport of bubbles on a Sauter mean diameter scale. By restricting our analysis to bubbles that reside only in the shear layer, Sauter mean diameter shows agreement with experiments throughout the jump (Figure 3.17). At nearly all locations, simulated d_s is within one standard deviation of experimental values.

A marked improvement towards experimental values of d_s is seen as the grid size is reduced. At a grid size of $\Delta x = 1.25$ mm, the largest bubbles in the shear layer attain a bubble diameter to grid ratio of eight, in agreement with the resolution requirement for bubbles in a VOF method set by Tomiyama et al. (1993). This corresponds with the large improvement in average entrained air seen in Table 1. We conclude that given the computational effort associated with the accuracy of bubble diameter presented herein, a 2D simulation will give an accurate bubble size distribution and depth-averaged void ratio when the largest bubble diameter is represented with eight computational cells, or

when four computational cells represent the depth-averaged Sauter mean diameter. If void fraction and total air entrainment are the prime concern, a 2D simulation is accurate to within 10% of total entrained air. A 3D simulation improves the vertical bubble distribution and longitudinal bubble transport within the jump. If proper bubble dynamics are more important than average void fraction, a 3D simulation is required, again with at least eight computational cells contained within the largest bubble diameter.

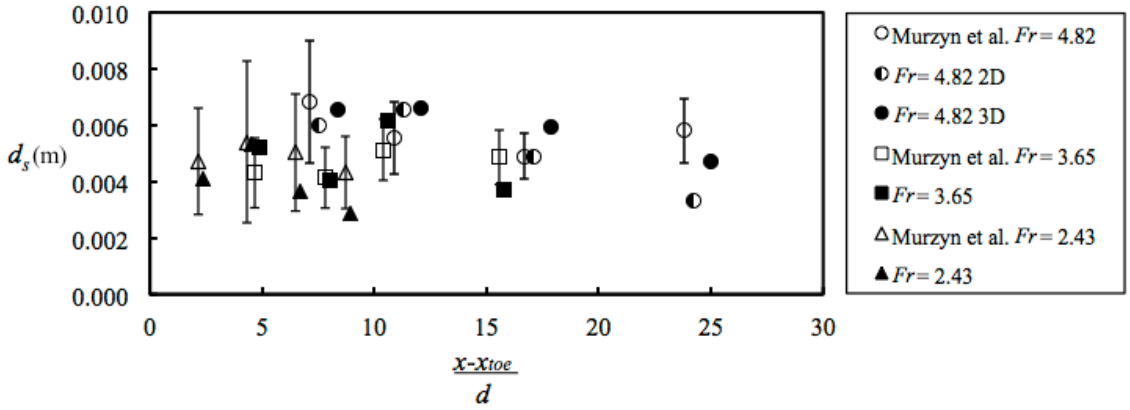

Figure 3.17. Depth-averaged Sauter mean diameter within the shear layer. Error bars indicate one standard deviation of experimental values.

3.4. Vortical structures

The hydraulic jump is frequently modeled as a 2D problem when the width to inlet depth ratio is sufficiently large, yet the presence of complex vortical structures and turbulence indicates a 3D phenomenon. These processes are not resolved in 2D simulations, leading to a less accurate prediction of air entrainment and bubble transport. A clear characterization of the additional bubble transport mechanisms resolved in a 3D simulation is required to understand the shortcomings of a 2D simulation. In this section, we visualize the 3D vortical structures associated with primary and secondary bubble transport and describe their importance in mixing and breakup.

Limited experimental evidence suggests the hydraulic jump flow field is similar to a mixing layer (Hoyt and Sellin, 1989; Long et al., 1991; Mossa and Tolve, 1998), yet difficulty in obtaining instantaneous experimental data over space has restricted quantitative analysis. Recent analysis of video images has shown that spanwise vortices are produced at a constant rate that tracks closely with the average oscillation frequency of the toe (Zhang et al., 2012). However, the toe fluctuates only quasi-periodically about a mean value, and frequently exhibits large and small oscillations consecutively in the same direction. It is observed in simulations that these oscillations introduce instabilities of varying intensity and frequency into the upstream jet, which manifest downstream as vortices after a shear-layer roll-up. Under some circumstances the vortices convect downstream at a constant speed, while under other circumstances the vortices may merge, altering their convective velocity. The downstream vorticity signature responds dynamically to a stimulus at the toe, analogous to a forced mixing layer with induced vortex pairing downstream (Ho and Huang, 1982). To explore this behavior further, the vorticity structure within the jump is analyzed during an upstream and a downstream toe fluctuation.

When the toe is moving upstream, the shear layer appears to experience fairly consistent roll-up. During this regime the roller recirculates an uninterrupted source of bubbly fluid to the toe, and the shear layer instability develops far enough downstream

that vortices have limited interactions with the free surface. In Figure 3.18 (top), four vortices are present in the shear layer, as visualized by contours of spanwise vorticity. The roller is flattened, meaning the recirculating fluid in the roller cascades towards the toe largely unaffected by the underlying vortical structures, and the free surface exhibits a fairly constant slope starting from the toe and moving downstream. The distance between vortex centers, defined as the location of maximum vorticity within a closed vorticity contour, increases slightly moving downstream, from 4.4*d* between A and B, 5.0*d* between B and C, and 6.25*d* between C and D. The vorticity contours exhibit some modulation around larger pockets of air, as was also evidenced in DNS simulations of a bubble rising through a free shear layer (Taeibi-Rahni et al., 1994). Figure 3.18 (bottom) shows an advancement in time of 0.2 s, in which the toe has fluctuated upstream, two new vortices have been generated, and the remaining vortices have convected downstream. The distance between the first four vortex centers increases moving downstream, while the distance between B and C decreases as the vortices begin to rotate around each other and pair. This is correlated with a free surface perturbation directly upstream of the merging point. No large perturbations are seen near the toe, consistent with a lack of pairing there. While in a classic mixing layer a lack of vortex pairing reduces the spreading rate (Ho and Huang, 1982), a lack of vortex pairing near the toe of a hydraulic jump flattens the roller, allowing the recirculating flow to spill further and send the toe upstream.

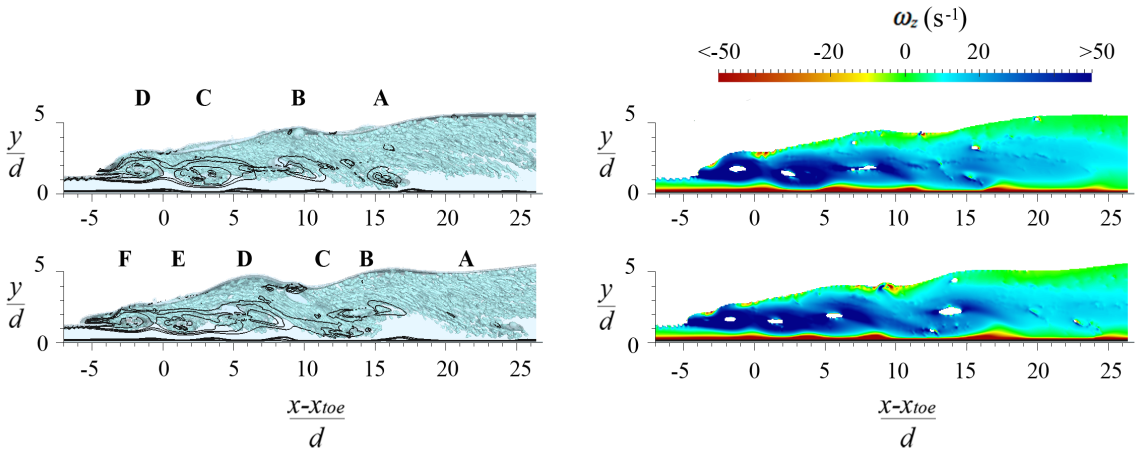

Figure 3.18. Visualization of the eddy structure during an upstream fluctuation of the toe. Left: a combination of selected instantaneous vorticity contours (ω_{mag} = 30, 40, 50, 100, 200 s^{-1}) through a 2D *x*-*y* plane down the center of the domain. Vorticity maxima inside a vorticity contour are indicated by A through F. Bubbles are represented by a volume fraction isosurface on $\gamma = 0.95$. Right: a color contour map of ω_z through a 2D plane down the center of the domain. White areas indicate regions of high void fraction. Top and bottom rows are separated by 0.2 s.

When vortices pair in the shear layer, the corresponding interruption of flow from the roller alters the forcing mechanism and the toe moves downstream. A series of vortex pairing and downstream toe fluctuations is shown in Figure 3.19. Initially the roller is relatively flat and distinct vortices are present (Figure 3.19a). When vortices pair near the toe (Figure 3.19b to Figure 3.19c, F-E), the free surface is perturbed and rises. This rise in elevation creates a cascade of roller fluid down the upstream side of the elevated free surface. As the impact of the spilling roller deflects the impinging jet downwards a strong roll-up occurs (Figure 3.19d, G), resulting in vertically offset vortices that begin to rotate around each other (Figure 3.19e, H and G). The vorticity contours of H-G in Figure 3.19f exhibit a strong similarity to the convective merging of two co-rotating vortices obtained experimentally (Figure 1 of Cerretelli and Williamson, 2003). At this point the toe exhibits a fluctuation downstream immediately after vortex merging. Further, more violent disruptions of the free surface result (Figure 3.19g), again producing pairs of vertically offset vortices (J, I) that merge and form a roll-braid

structure (Figure 3.19l). The merging of vortices provokes a dynamic response at the free surface that results in greater shear layer instabilities and a fluctuation of the toe downstream. This feedback loop is achieved at some point during the steady roller flow regime (Figure 3.18), and appears to intermittently return to that regime after the toe reaches a maximum position downstream.

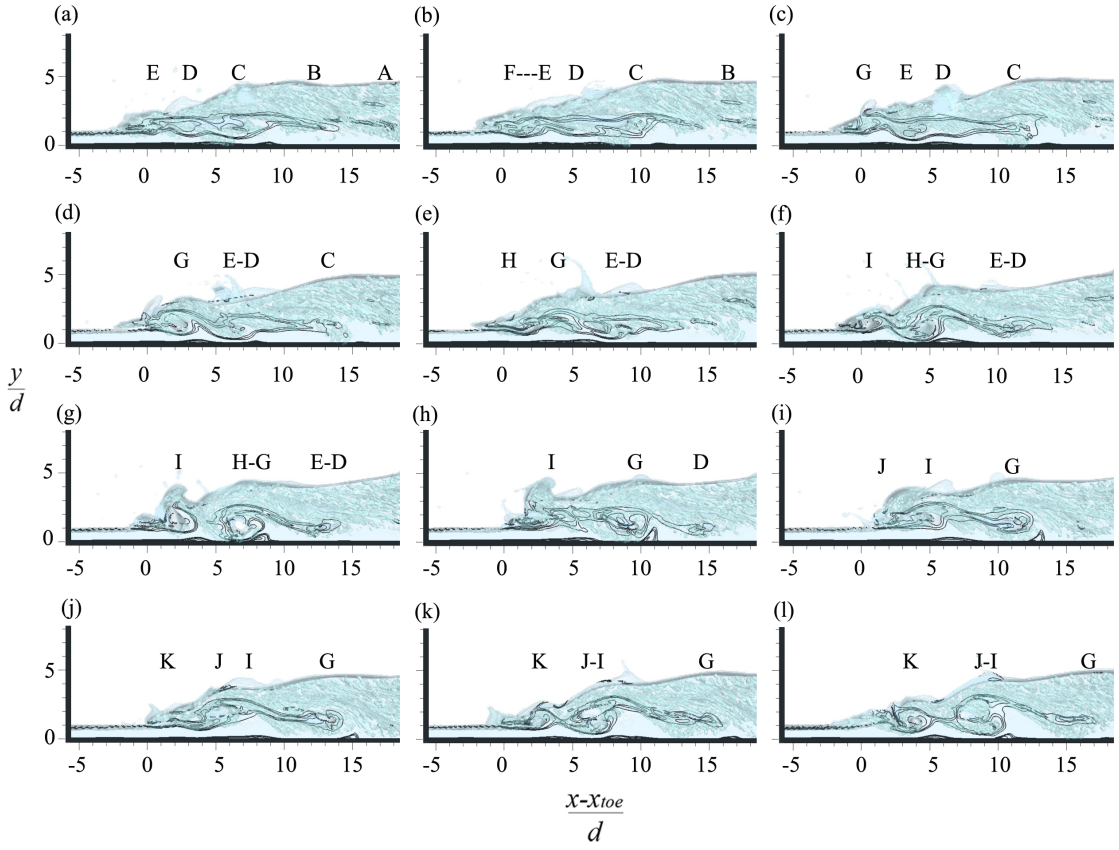

Figure 3.19. Frame-by-frame representation of selected instantaneous vorticity contours (black lines) for ω_{mag} = 30, 40, 50, 100, 200 s^{-1}, through a 2D *x*-*y* plane down the center of the domain, and bubbles represented by a volume fraction isosurface on $\gamma = 0.95$. Distinct vortices are marked A through G, with the '–' indicating merging vortices. For consistency a merged vortex retains the marking of the downstream vortex. The evolution of semi-periodic downstream fluctuations leads to a roll-braid structure (l). Frames are separated by 0.05 s.

The convective velocity of vortices, u_c, is obtained by tracking the vortex centers over time for Figure 3.18 and Figure 3.19. The result is plotted in Figure 3.20. The majority of vortices show a constant convective velocity, with an average of $u_c/U_o = 0.35$ for Figure 3.18 and 0.4 for Figure 3.19, in line with the value of 0.4 obtained experimentally by Zhang et al (2012) for similar Froude and Reynolds number hydraulic jumps. In the regime where no merging is observed, all vortices within the shear layer travel at a similar speed. At some point, an upstream vortex reaches a critical distance from a downstream vortex and the merging process begins. The mutual influence of each individual vortex results in a counter-clockwise rotation of the vortex pair, forcing the upstream vortex to descend lower to a region of higher horizontal velocity (Figure 3.19f, H; Figure 3.19k, J). The downstream vortex rotates higher into a lower velocity region, leading to a rise in free surface elevation (Figure 3.19f, G; Figure 3.19k, I). This interaction occurs quickly, and the resultant merged vortex travels downstream with a nearly constant velocity.

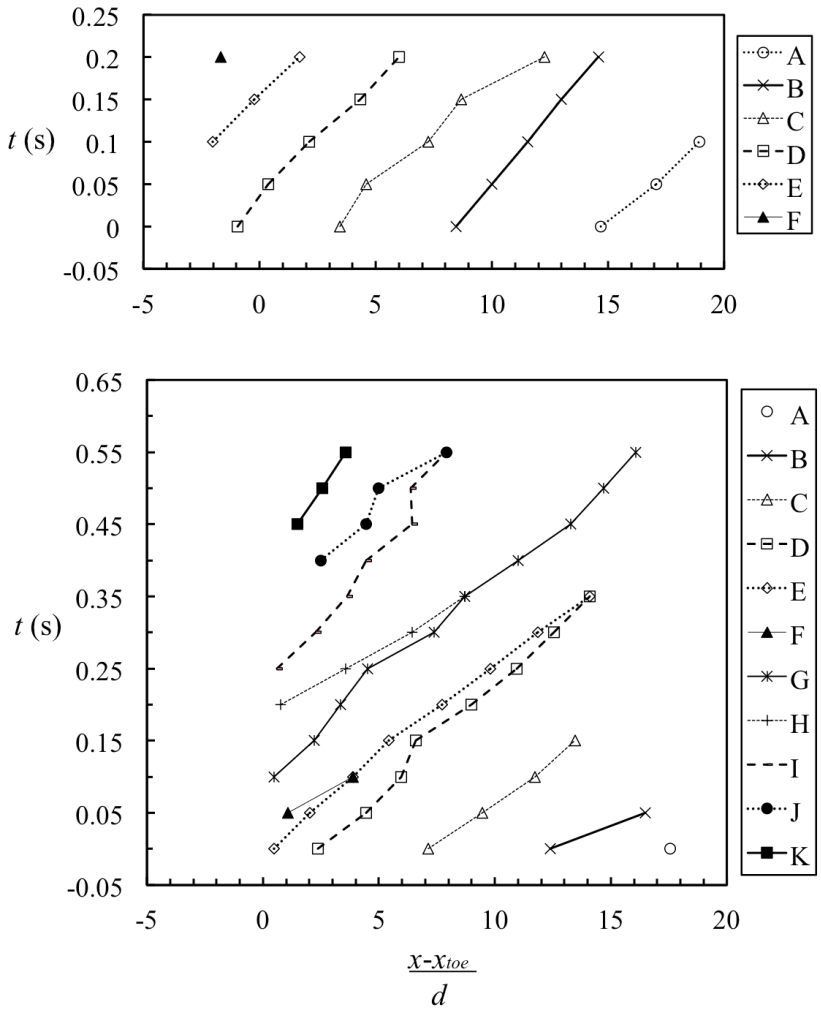

Figure 3.20. Vortex center tracked over time. Top: vortices observed from Figure 3.18. Bottom: vortices observed from Figure 3.19. Letters correspond with vortices from each figure.

Spanwise vortex instabilities generate secondary, streamwise vortices within a mixing layer (Bernal and Roshko, 1986; Hussain, 1986). These streamwise vortices are present in the saddle, or braided region, which is characterized by a relatively small amount of coherent spanwise vorticity, longitudinal vortex stretching, and high shear (Hussain, 1986). Hoyt and Sellin (1989) proposed that a similar braiding process exists in a hydraulic jump, and provided a sketch of a roll-braid structure. Our 3D numerical simulation displayed evidence of a roll-braid structure between two spanwise vortices following the roll-up and subsequent pairing and subsequent roll-up of a spanwise vortex (Figures 3.19f, 3.19l). As shown in Figure 3.21, counter-rotating streamwise vortex pairs, located in the saddle point between the first and second spanwise vortices downstream from the toe, were observed following the roll-up of merged spanwise vortices (Figures 3.21a, b, c). The pairs form near the upper portion of the downstream side of a spanwise vortex, and are oriented diagonally downward towards the upstream side of the neighboring downstream spanwise vortex. Streamwise vorticity is strongest at the upstream side of the pair, in line with the upwelling of fluid from the neighboring upstream spanwise vortex. The interaction of these nearly orthogonal (i.e. spanwise and streamwise) vortices has been shown to produce high 3D turbulence and mixing (Hussain, 1986). Consequently, bubbles transported through this region are consistently observed to experience breakup and are more likely to be transported to lower regions of the flow by the neighboring downstream spanwise vortex. The increased shear provided by streamwise vortices results in improved simulations of void fraction and Sauter mean diameter in 3D compared with 2D, as shown in Sec. 3.3.

The combined counter-rotating motion between streamwise vortices is observed to contribute to free surface fluctuations (Figure 3.21a). The diameter of streamwise vortices is approximately $1d - 2d$, as is the transverse length of the corresponding free surface fluctuations (Figure 3.21a). This is in agreement with the transverse free surface integral length scales observed near the toe in experiments with jumps of similar Fr (Chachereau and Chanson, 2011a). Longitudinal free surface fluctuations are observed above merged spanwise vortex pairs, with a length of $2d$ - $3d$ (Figure 3.19g, Figure

3.19l), also in line with experimental observations. These results suggest the additional upward flux of fluid between streamwise vortex pairs adds a three-dimensional component to free surface fluctuations.

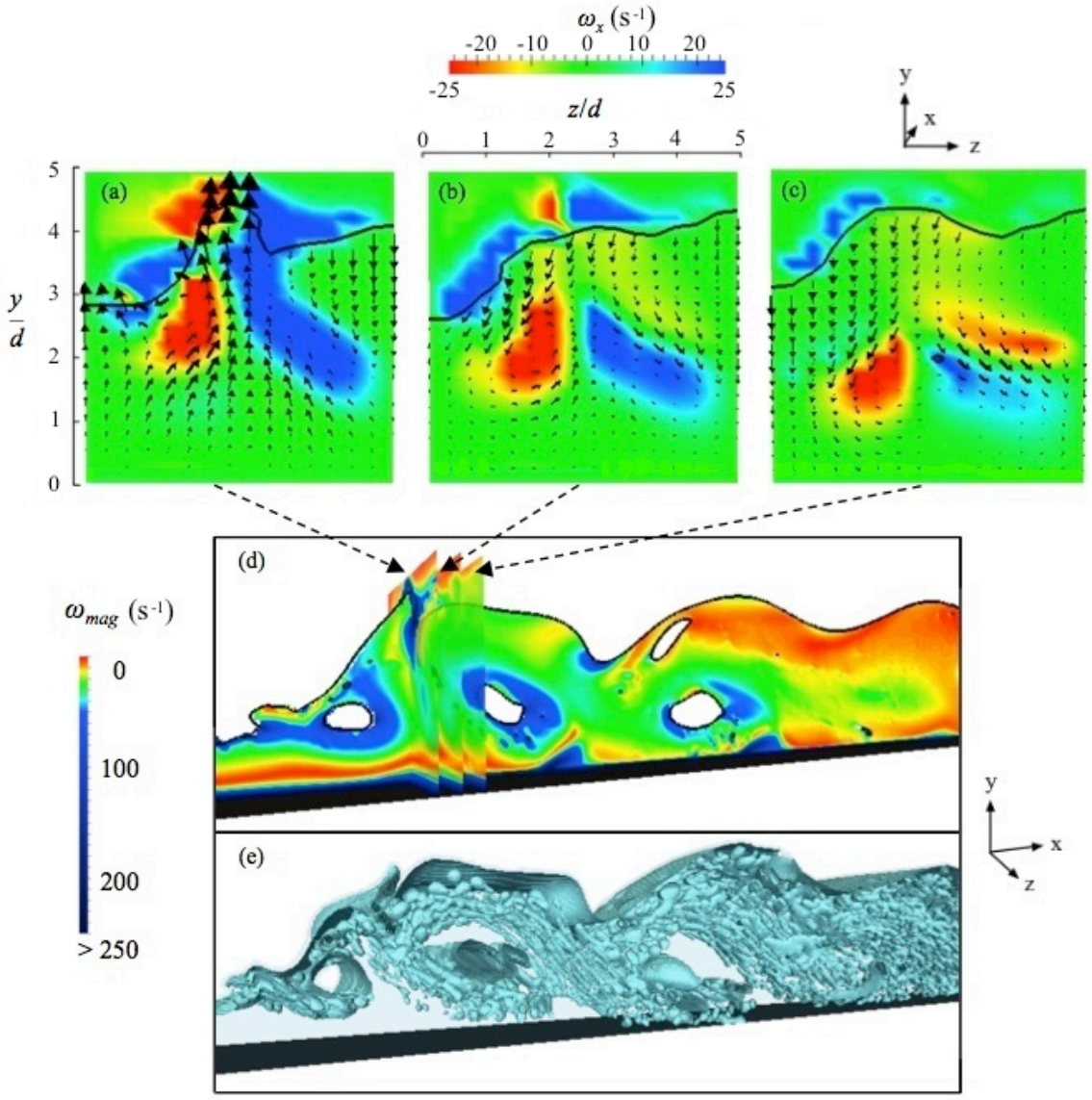

Figure 3.21. Counter-rotating streamwise vortices observed between two connected spanwise vortices. (a, b, c) Spanwise, plan views of ω_x are separated by 0.5d. Arrows represent velocity vectors in the y-z plane, while the solid black line represents the instantaneous free surface. (d) Contour map of ω_{mag} through a 2D plane down the center of the domain. (e) A 3D view of a volume fraction isosurface on $\gamma = 0.95$.

A spatially inhomogeneous bubble field is observed in the presence of a braid-roll structure. As large spanwise vortices descend towards the floor, eddies are shed from the high shear region at the wall (Figure 3.19g, Figure 3.19h). If these eddies have sufficient strength, they are observed to contribute to the break up of the connected roll-braid structure by sending an upwelling of fluid into the saddle (Figure 3.19h, Figure 3.19i). The fluid in the lower boundary layer is devoid of bubbles, and this injection into the shear layer creates a distinct region with no bubbles. Additionally, spanwise vortices induce some noticeable clustering of bubbles, in that a lack of bubbles is observed immediately downstream of strong spanwise vortices, while the center of each vortex contains a high concentration of bubbles (Figure 3.22). This observation is concurrent with experiments, where two regions of high air concentration are observed after a large spill of the roller (Mossa and Tolve, 1998). It is clear from the simulations that each oscillation of the toe gulps pockets of air that travel within rotating spanwise vortices. Smaller bubbles tend to rotate on the exterior of the vortex, where they can be transported to the lower region of the shear layer by the combined action of streamwise vortices and spanwise rotation.

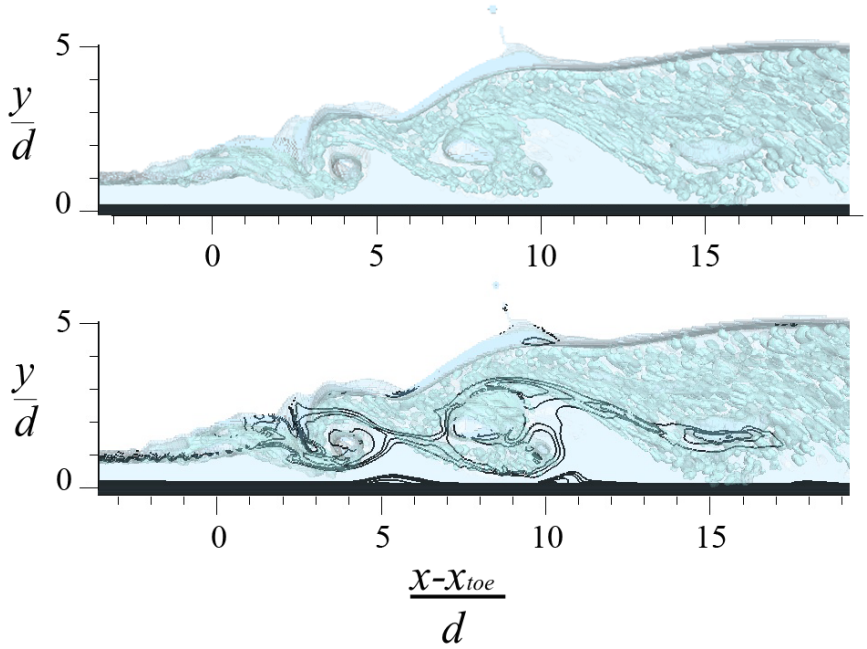

Figure 3.22. Selected instantaneous vorticity contours (black lines) for ω_{mag} = 30, 40, 50, 100, 200 s^{-1}, through a 2D *x*-*y* plane down the center of the domain, and bubbles represented by a volume fraction isosurface on $\gamma = 0.95$, during a roll-up of a streamwise vortex (from Figure 3.19l). Top: spatially inhomogeneous bubble field. Bottom: a lack of bubbles is seen on the lower downstream side spanwise vortices, below the location of streamwise vortex pairs, and above the region where vorticity is shed from the wall.

The upstream and downstream oscillations of the toe have a significant effect on vortex dynamics within the jump. The complex interactions of spanwise vortices, wall eddies, and streamwise vortex pairs are not present in 2D simulations. This is believed to have an impact on bubble breakup, coalescence, and transport within the turbulent shear region. As shown in Figure 3.9b, the 3D simulation produced a more accurate average void fraction profile within the shear layer. The 3D simulation produced y_{Cmax} higher than in the 2D simulation, which is more consistent with experiments. Bubble size was also more accurate in the 3D simulation (Figure 3.17). These results suggest improved void fraction and bubble size in a 3D simulation can be attributed to vertical and horizontal bubble transport and bubble breakup due to the combined action of streamwise and spanwise vortical structures.

3.5. Conclusions

The goal of the present study was to develop a computational framework for the investigation of air entrainment and bubble dynamics in simulated hydraulic jumps. Simulations in 2D and 3D are carried out using an unsteady RANS formulation, a realizable k-ε turbulence closure model, and a VOF numerical treatment of the free surface. Void fraction profiles, velocity profiles, and Sauter mean diameter are validated against experimental data from the literature. The total air entrained by the jump is found to converge to experimental values, while Sauter mean diameter shows similarity to experimental estimates within the turbulent shear region. A VOF treatment of the free surface at the proper grid size, sampling rate, and sampling time intrinsically captures air entrainment at a hydraulic jump without the use of an *ad hoc* air entrainment subgrid model, an improvement over previous simulations reported in the literature. Further, our results confirm that experimental methods for obtaining bubble size estimates near the free surface over-predict Sauter mean diameter.

Our simulations indicate that if the objective of study is to determine the quantity of air entrained by a hydraulic jump, a 2D simulation will produce results within a 10% difference of experimental values, without requiring excess computational time, when the diameter of the largest bubbles in the flow is represented by at least eight computational cells. A 3D numerical simulation is recommended if bubble dynamics are considered an important process to model. Improved void fraction profiles and bubble size distributions in a 3D simulation are attributed to improved modeling of bubble transport, and to better resolution of bubble breakup due to the combined action of streamwise and spanwise vortical structures. Improvements come at a cost of two orders of magnitude increase in computational time compared with the 2D simulation, and are manifest in void fraction profiles immediately downstream from the toe, where 3D turbulence and mixing decrease average bubble size.

Examination of the 3D flow field provides an improved understanding of the flow physics, particularly the behavior of vortical structures and their effect on bubble

transport. Spanwise vortices are generated at the confluence of two counter flowing streams, the roller and the impinging jet. Vortex evolution is significantly impacted by the self-forcing mechanism of the recirculating roller, which imparts vorticity into the impinging jet. Unlike a typical mixing layer, the slow stream (i.e. roller) exhibits a dynamic response to the underlying vortex behavior. When vortices convect without merging they have limited interactions with the roller, and steady recirculation moves the jump toe upstream. The toe becomes supply limited and moves downstream when the convective merging of vortices interrupts cascading roller fluid. Vortices merge quickly and maintain a fairly constant velocity downstream. As a consequence of vortex merging, short-lived counter-rotating streamwise vortices are created which combine with spanwise vortices to produce free surface fluctuations. The simulations presented herein reveal flow structures that cannot be visualized experimentally, leading to a better understanding of the flow physics within the hydraulic jump.

4. Numerical investigation of vorticity and bubble dynamics in a hydraulic jump

4.1. Introduction

The hydraulic jump is a commonly employed energy dissipation mechanism downstream of hydraulic structures. The jump is characterized by a rapid rise in free surface elevation at the transition from supercritical flow to subcritical flow, and is accompanied by intense turbulence, energy dissipation, and air entrainment. The strength of the hydraulic jump is classified by Froude number, $Fr = U_o/(gd)^{1/2}$, where U_o is the velocity of the upstream jet, d the depth of the upstream jet, and g is acceleration due to gravity. The air entrainment rate, maximum bubble count rate, maximum air concentration, and roller aeration length all increase with increasing Fr (Rajaratnam, 1962; Chanson and Brattberg, 2000; Hager, 1992). A significant bubble population is present throughout the jump, a result of the entrainment of large air pockets at the toe and subsequent breakup and coalescence in the developing turbulent shear layer. Characterizing the behavior, transport, and evolution of these bubbles is critical to developing models of air entrainment and gas transfer at the hydraulic jump (Urban et al., 2008).

The air-water flow properties of the hydraulic jump have been experimentally investigated in detail (Rajaratnam, 1967; Resch and Leutheusser, 1972; Chanson and Brattberg, 2000; Murzyn et al., 2005; Chachereau and Chanson, 2011b). Significant contributions include longitudinal characterization of void fraction profiles, bubble diameter, velocity distribution, and turbulence characteristics. Turbulence in the jump is generated at the confluence of two semi-parallel counter flowing streams, the roller and the impinging jet, leading to the creation of large spanwise vortices (Peregrine and Svendsen, 1978; Hoyt and Sellin, 1989; Rodriguez-Rodriguez et al., 2011; Zhang et al.,

2012). The interaction of successive spanwise vortices produces semi-periodic fluctuations of the toe and roller surface (Murzyn and Chanson, 2009; Witt et al., 2014), resulting in complex interactions between entrained bubbles and vortical structures.

The inherent spatial limitations of intrusive probes restrict most experimental analysis of the jump to time-averaged air-water properties. To overcome this limitation, visual techniques including particle image velocimetry (Lin and Rockwell, 1995; Lennon and Hill, 2006), image processing (Mossa and Tolve, 1998; Chanson, 2010), Doppler ultrasound velocimetry (Liu et al. 2004), and bubble image velocimetry (Lin et al., 2012) have been employed to illuminate the instantaneous features of the jump. Other techniques seek to extract 2D and 3D signatures from 1D data, such as inhomogeneity in longitudinal clustering of bubbles in the shear layer (Gualtieri and Chanson, 2010; Chachereau and Chanson, 2011b). The high void fraction content in the roller, the presence of a recirculation region with negative velocity, and the turbulent 3D nature of the jump prove significant obstacles in conducting a detailed experimental analysis of instantaneous bubble-water interactions.

Improved numerical algorithms for modeling the interface between two immiscible fluids have led to increasingly accurate studies of air entrainment and bubbly flows, and can assist in investigating the instantaneous features of the hydraulic jump. A Volume of Fluid (VoF) approach has been employed to simulate breaking waves (Lubin et al., 2006), plunging jets (Deshpande et al., 2012a), flow over stepped spillways (Cheng et al., 2004), and the hydraulic jump (Witt et al., 2014). Two methods of turbulence modeling have emerged for these types of flows: large eddy simulation (LES) and two-equation unsteady Reynolds-averaged Navier Stokes (URANS) closure models. In an LES approach, a filtering operation is applied to the Navier-Stokes equations, resulting in a filtered velocity field that explicitly resolves large scale eddies. Small scale eddies, or the interactions of unresolved and resolved scales, are modeled using a subgrid term, the residual stress tensor. In a URANS model, the Navier-Stokes equations are separated into mean and fluctuating components and then ensemble averaged, leaving only the mean flow quantities and a fluctuating velocity product term, known as the Reynolds

stress tensor. The difference in these two formulations lies in the treatment of subgrid turbulence: the Reynolds stress tensor represents the global effect of all turbulence scales on the flow field, while the residual stress tensor in the LES model only accounts for the effects of turbulent fluctuations with length scales smaller than the filter width. In this sense, the grid resolution becomes a significant computational limitation when choosing a turbulence model. An LES model must be sufficiently fine as to resolve the large scale eddies of the flow. Numerical studies using an LES turbulence model to simulate air entrainment in breaking waves have employed a grid resolution an order of magnitude lower than that of the present study (Lubin et al., 2006; Iafrati, 2009). Additionally, these studies apply a periodic boundary condition, which eases the computational requirements associated with a small grid resolution. A URANS model accommodates a wider range of flow and boundary conditions, allows for a larger grid size, and has proven a robust method of representing turbulence in the hydraulic jump (Gonzalez and Bombardelli, 2005; Carvalho, 2008; Cheng and Chen, 2013).

The benefit of capturing air entrainment in a simulated hydraulic jump would pay dividends in developing boundary and operating conditions for bubbles at prototype hydraulic structures. The presence of bubbles in the stilling basin downstream of a hydropower dam, for example, is responsible for a significant amount of gas transfer. Computational models tend to assume a representative bubble diameter based on an estimation of turbulent length scales (Orlins and Gulliver, 2000; Urban et al., 2008), while CFD models often incorporate a uniform bubble size at the point of entrainment (Politano et al., 2009). These models require calibration with field measurements, and are typically sensitive to the prescribed initial conditions. The development of accurate air entrainment models could help reduce the uncertainty in gas transfer models by generating a range of bubble size distributions based on specific operating conditions. These results could serve in addition to or replace field calibration, leading to significant cost reductions.

In a related recent work, we employ a VoF interface-capturing scheme with a URANS turbulence closure model to simulate the air entrainment and air-water

characteristics of the hydraulic jump (Witt et al., 2014). It was shown that both 2D and 3D numerical models capture the entrained air, average bubble diameter, and velocity characteristics fairly well. Visualization of the vorticity and volume fraction fields revealed the transport and merging of vortices formed at the toe resulted in downstream fluctuations of the toe, free surface perturbations in the roller, and some coherent organization of bubble structures in the turbulent shear layer. The primary objective of the current work is to investigate this phenomenon in more detail, exploring the properties of vorticity and entrained air using a 3D numerical model and, where appropriate, a 2D model.

In what follows, a description of the numerical method and setup is given in Sec. 2. A limited validation and description of ensemble average characteristics are presented in Sec. 3. Instantaneous vorticity characteristics and shear layer behavior are described in Sec. 4. Some analysis of bubble clusters and breakup are explored in Sec. 5, and the main conclusions of this work are summarized in Sec. 6.

4.2. Numerical method

A description of the simulation conditions, domain boundaries, and numerical treatment is described in a recent work (Witt et al., 2014). A comparison of 2D and 3D results was presented, and the resolution of turbulent structures in 3D was responsible for improvements in average void fraction and bubble diameter. The 2D results showed comparable accuracy in terms of average air entrained and Sauter mean diameter within the shear layer. The scope of the current study is to further investigate the air water characteristics of the hydraulic jump, and thus a differentiation between 2D and 3D results is not considered. Where relevant, 2D results are presented in tandem with 3D results to enhance the discussion. A brief description of the numerical method is outlined below to provide further clarity to the present study.

4.2.1. Physical setup

The experimental configuration simulated in this study is shown in Figure 4.1. A recirculating laboratory scale flume was used to generate a hydraulic jump characterized by inflow Froude (*Fr*) number (Murzyn et al., 2005). Three jumps of Fr = 2.43, 3.65, and 4.82 are used for comparison with the numerical simulation. The upstream jet depth was controlled by regulating flow through a sluice gate, while a downstream overshot weir of depth d_{weir} stabilized the jump and set the tailwater depth, d_{tw}. The inflow was considered partially developed, with a boundary layer thickness ranging 0.2d to 0.4d. Dual-tip optical phase detection probes with a sampling rate of 1 MHz were deployed throughout the jump to obtain mean air-water statistics over a sampling time of 2 min.

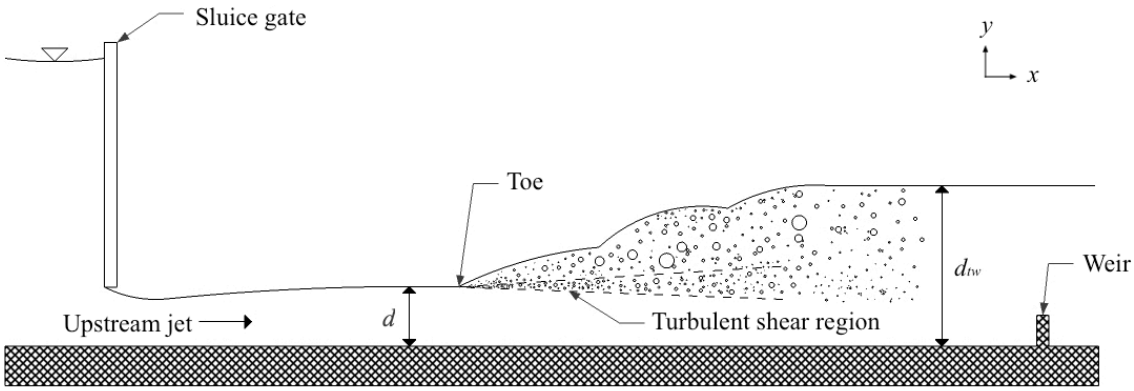

Figure 4.1. Representation of the experimental set-up of Murzyn et al. (2005). Not to scale.

With respect to the dimensions of the domain, the experimental flume extended a length of L_x = 12 m, a depth of L_y = 0.4m, and a width of L_z = 0.3 m. Computational domain boundaries are shown in Table 4.1 and Figure 4.2, and were chosen to ensure the domain boundaries did not interrupt the dynamics of the impingement and roller regions. Successive grid refinements were made in the upstream side of the domain, ensuring the full hydraulic jump, including a length of 10d downstream from the final measurement point, were contained within the finest mesh. Two simulations were carried out in 2D for

Fr = 2.43 and 3.65, and one simulation was run in 3D for Fr = 4.82. All results from the 3D simulation are taken on an x-y plane at $z = 0.5L_z$. Additional details regarding the dimensions of each case are also displayed in Table 4.1.

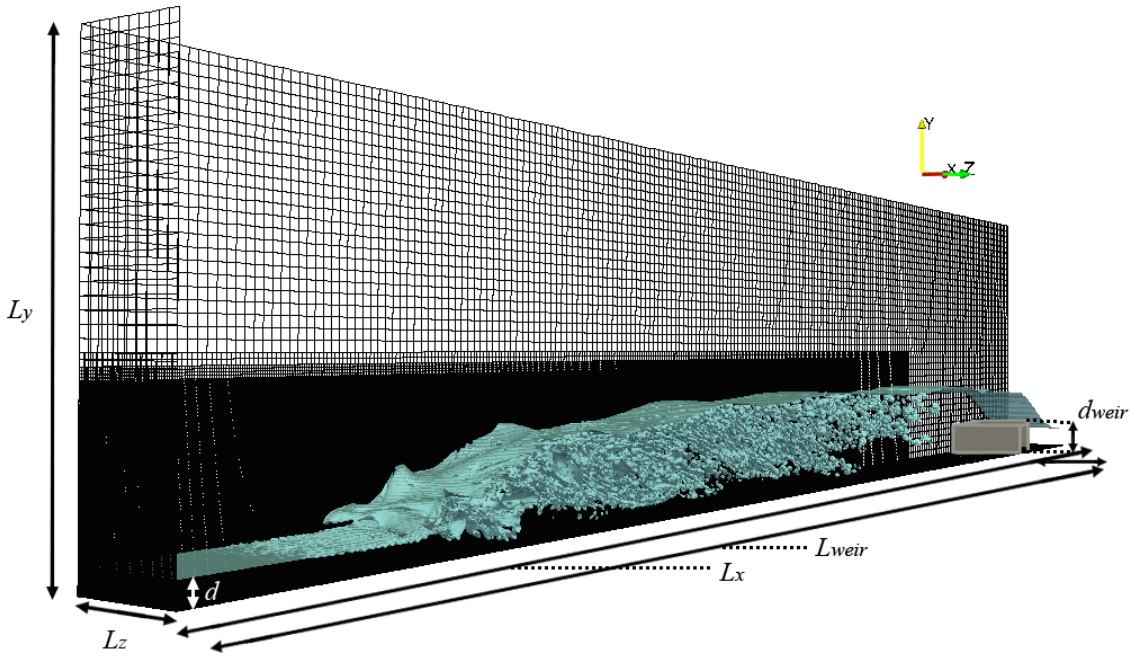

Figure 4.2. Simulated hydraulic jump and computational domain in 3D for Fr = 4.82. Bubbles and the free surface are represented by isosurface contours about a volume fraction of γ = 0.95.

Table 4.1. Description of simulation conditions corresponding to different Fr.

Fr (-)	Re (-)	d (m)	U_o (m/s)	L_x (-)	L_{weir} (m)	d_{weir} (m)	L_y (m)	L_z (m)
2.43	75,440	0.046	1.64	63d	58d	0.89d	8.7d	(-)
3.65	65,600	0.032	2.05	90d	83d	1.28d	13d	(-)
4.82	45,990	0.021	2.19	100d	89d	1.95d	19d	4.76d

4.2.1. Numerical simulation description

The simulations were computed using OpenFOAM, an open source computational fluid dynamics solver. The solver utilizes a finite volume discretization on collocated grids to solve a system of two immiscible fluids. An unsteady, Reynolds-Averaged Navier Stokes (URANS), realizable k-ε turbulence closure model was employed with a Volume of Fluid (VoF) representation of the interface between liquid and gas phases. The solver has been validated for a number of air-water characteristics including interface advection and surface tension (Deshpande et al., 2012b) and in inertia driven flows (Berberovic et al., 2009), vertical plunging jet flows (Deshpande and Trujillo, 2013), and the hydraulic jump (Witt et al., 2014).

An outline of the numerical procedure is presented below. A full description of the development and discretization of the governing equations is found in Rusche (2002) and Deshpande et al. (2012b). Within the OpenFOAM solver *interFoam*, the transport of a volume of fluid in time is expressed by an advection equation,

$$\frac{\partial \gamma}{\partial t} + \nabla \cdot (\gamma \boldsymbol{u}) + \nabla \cdot (\boldsymbol{u_c} \gamma (1 - \gamma)) = 0 , \tag{4.1}$$

where γ is the volume fraction of fluid in a cell, $\boldsymbol{u}$ is the fluid velocity vector, and $\boldsymbol{u_c}$ is an artificial compression term designed to reduce smearing of the interface (Rusche, 2002). This equation represents an algebraic interface capturing scheme, meaning the interphase between liquid and gas is not reconstructed in each cell. Instead, the interface is contained within a single cell and an enhanced numerical treatment is employed to reduce numerical diffusion at the gas-liquid interface.

In discrete form, Eq. 5.1 is given as

$$\frac{\gamma_i^{\,*} + \gamma_i}{\Delta t} = -\frac{1}{|\Omega_i|} \sum_{f \ni \partial \Omega_i} (F_u + \lambda_M F_c) , \tag{4.2}$$

where the '*' represents the new time step, Δt is the discrete time step, λ_M is a delimiter equal to zero away from the gas-liquid interface and one in cells containing an interface ($0 < \gamma < 1$), the advection term is separated into upwind (F_u) and compression (F_c) components, and a summation of these terms is performed over the cell faces (f) of the control volume Ω_i (Rusche et al., 2002; Deshpande et al., 2012b). The advective fluxes are

$$F_u = \phi_f \gamma_{f,\,upwind};\; F_c = \phi_f \gamma_f + \phi_{rf} \gamma_{rf} (1 - \gamma)_{rf} - F_u \,, \tag{4.3}$$

where ϕ_f is the volume flux, or $\boldsymbol{u}_f \cdot \boldsymbol{S}_f$, with the subscript f representing cell face values and $\boldsymbol{S}_f$ representing the surface area vector. Cell face values are obtained using a second order linear interpolation between neighboring cells. Away from the interface F_u is treated with an upwind scheme. In cells that contain an interface, a higher order scheme for $\phi_f \gamma_f$ is combined with a compressive scheme for $\phi_{rf} \gamma_{rf} (1- \gamma)_{rf}$ (Deshpande et al., 2012b). This treatment is known as a blended differencing scheme, which attempts to preserve the boundedness of the volume fraction while maintaining a high level of accuracy (Rusche, 2002).

The momentum equation is shared between liquid and gas phases, and is represented by

$$\frac{\partial(\rho \boldsymbol{u})}{\partial t} + \nabla \cdot (\rho \boldsymbol{u}\boldsymbol{u}) \;=\; -\nabla p + \rho \boldsymbol{g} + \nabla \cdot \boldsymbol{\tau} + \sigma \kappa (\boldsymbol{x} - \boldsymbol{x}_s) \boldsymbol{n} \,, \tag{4.4}$$

where ρ is the fluid density, p is the pressure, $\boldsymbol{g}$ is the acceleration due to gravity, τ represents the viscous stress tensor, $\tau = 2\mu \boldsymbol{S} = 2\mu(0.5[(\nabla \boldsymbol{u}) + (\nabla \boldsymbol{u})^{\mathrm{T}}],])$ where $\boldsymbol{S}$ is the strain rate tensor, μ is the dynamic viscosity, σ is the surface tension, and κ is the mean curvature of the free surface, $\boldsymbol{n}$ is the normal vector of the interface, and $\delta(\mathbf{x}-\mathbf{x_s})$ is the Dirac Delta function, applied only at a gas-liquid interface. The values for density and viscosity are based on a phase-weighted average obtained from the updated volume fraction

$$\rho = \rho_l \gamma + \rho_g (1 - \gamma), \quad \mu = \mu_l \gamma + \mu_g (1 - \gamma), \tag{4.5}$$

where the subscripts l and g denote the liquid and gas phases, respectively.

Two important modifications are made before discretization. First, the pressure is modified to remove the hydrostatic pressure

$$\nabla p_d = \nabla p - \nabla(\rho \boldsymbol{g} \cdot \boldsymbol{x}) = \nabla p - \rho \boldsymbol{g} - \boldsymbol{g} \cdot \boldsymbol{x} \nabla \rho , \tag{4.6}$$

where $\boldsymbol{x}$ is the position vector. This modification is employed to remove potential steep gradients due to hydrostatic effects and to simplify the pressure boundary condition at the wall (Rusche, 2002). Second, the Continuum Surface Force model of Brackbill et al. (1992) is used to convert the surface tension term into a body force. In this formulation the normal vector at the interface is calculated from the gradient of the volume fraction, $\boldsymbol{n} = (\nabla\gamma)/|(\nabla\gamma)|$, and the interfacial curvature is taken as $\kappa = -\nabla \cdot \boldsymbol{n}$. This method of computing the normal vector ensures the surface tension is only applied at a gas-liquid interface. The final term on the right hand side of Eq. 4.4 is then estimated as $\sigma\kappa\nabla\gamma$, and the momentum equation is recast as

$$\frac{\partial(\rho \boldsymbol{u})}{\partial t} + \nabla \cdot (\rho \boldsymbol{u}\boldsymbol{u}) = -\nabla p_d + -\boldsymbol{g} \cdot \boldsymbol{x} \nabla \rho + \nabla \cdot \boldsymbol{\tau} + \sigma\kappa\nabla\gamma . \tag{4.7}$$

The volume fraction advection equation and momentum equation, along with conservation of mass,

$$\nabla \cdot \boldsymbol{u} = 0 , \tag{4.8}$$

represent the complete set of governing equations for the liquid-gas system.

An unsteady Reynolds-Averaged Navier Stokes (RANS) method is applied to model subgrid turbulence. In this approach, the momentum and continuity equations are Reynolds Averaged, resulting in a Reynolds stress representing the effects of turbulence. A Boussinessq approximation is used to relate the Reynolds stress to an eddy viscosity, which represents the transport and dissipation of energy due to unresolved turbulence. A two equation, realizable k-ε approach is applied to compute eddy viscosity. The

realizable approach differs from the standard k-ε closure scheme in that the positivity of normal stresses are ensured by sensitizing C_μ to the mean strain rate, mean rotation rates, and turbulence fields. The realizable scheme has shown improved performance over the standard k-ε scheme in shear flows (Zhu and Shih, 1994; Kim et al., 1999), recirculating flows (Qian et al., 2009), and air entraining flows (Zidouni et al. 2010).

To implement this methodology into the present model, μ is replaced by an effective viscosity, μ_{eff}, where

$$\mu_{eff} = \mu + \mu_t \,, \tag{4.9}$$

and μ_t is the turbulent eddy viscosity. Eddy viscosity is then related to turbulent kinetic energy, k, and energy dissipation, ε, through a constitutive relationship

$$\mu_t = \rho C_\mu \frac{k^2}{\varepsilon} \,. \tag{4.10}$$

where C_μ is a variable model parameter sensitized to the mean strain rate, mean rotation rates, and the turbulence fields in a manner consistent with the physics of turbulent flows. A derivation and list of model variables can be found in Shih et al. (1995) and Witt et al. (2014), respectively.

The evolution of k and ε are modeled using

$$\frac{\partial(\rho k)}{\partial t} + \frac{\partial(\rho k \boldsymbol{u})}{\partial \boldsymbol{x}} = \frac{\partial}{\partial \boldsymbol{x}}\left[\left(\mu + \frac{\mu_t}{\sigma_k}\right)\frac{\partial k}{\partial \boldsymbol{x}}\right] + G_k - \rho\epsilon \,, \tag{4.11}$$

$$\frac{\partial(\rho\epsilon)}{\partial t} + \frac{\partial(\rho\epsilon \boldsymbol{u})}{\partial \boldsymbol{x}} = \frac{\partial}{\partial \boldsymbol{x}}\left[\left(\mu + \frac{\mu_t}{\sigma_\epsilon}\right)\frac{\partial \epsilon}{\partial \boldsymbol{x}}\right] + \rho C_1 \boldsymbol{S}\epsilon - \rho C_2 \frac{\epsilon^2}{k + \sqrt{\nu\epsilon}} \,, \tag{4.12}$$

where σ_k and σ_ε are model constants equal to 1 and 1.2, respectively, G_k represents turbulent kinetic energy generation from the mean velocity gradients,

$$G_k = 2\mu_t S_{ij} S_{ij} \,, \tag{4.13}$$

C_1 is a variable model parameter,

$$C_1 = \max\left[0.43, \frac{\eta}{\eta+5}\right], \ \eta = \frac{k}{\epsilon}\sqrt{2S_{ij}S_{ij}}, \tag{4.14}$$

C_2 is a model constant equal to 1.9, and v is the kinematic viscosity.

The updated values of the volume fraction are substituted into a finite volume form of Eq. 4.7 and the velocity and pressure fields are solved simultaneously using a Pressure Implicit Splitting of Operators (PISO) algorithm. The turbulent transport equations are lagged and solved using the available fluxes, velocity, and pressure fields. Discretization of the momentum and turbulent transport equations was carried out using a Crank-Nicolson scheme with an off-centering coefficient of 0.9 to improve numerical stability. Face values computed using a second order linear interpolation.

4.2.3. Computational domain

The computational domain shown in Figure 4.2 contained six distinct boundaries; a left inlet of depth d, a left wall from d to 0.2 m, a left outlet from 0.2 m to 0.4 m, a top outlet of length L_x, a right outlet of depth L_y, and a lower wall of length L_x. For velocity, a constant (U_o,0,0) m/s was prescribed at the inlet, while walls were modeled using a no-slip boundary condition and a wall turbulence model, and outlets were modeled using a zero gradient condition, $\mathbf{n} \cdot \nabla \boldsymbol{u}$. The volume fraction at the inlet was fixed at $\gamma = 1$, while a zero gradient was used for the remaining boundaries. Total pressure at the top outlet was set equal to 0 and calculated from $\boldsymbol{u}$ on the boundary using $p + \rho \boldsymbol{u}^2 = 0$. A zero gradient condition was used for the remaining outlets, while all other boundaries were modeled using a buoyant pressure boundary condition, $\mathbf{n} \cdot \nabla p_d = -(\mathbf{n} \cdot \nabla \rho)\, \boldsymbol{g} \cdot \boldsymbol{x}$.

4.2.3. Grid sensitivity

A grid refinement study was carried out by Witt et al. (2014) to determine the sensitivity of the air-water characteristics to grid size. It was observed that when eight computational cells represented the diameter of the largest bubbles in the flow, a

reduction in relative error of total entrained air below 10% of experimental values was achieved for 2D and 3D simulations. For the present study this represents a grid size of Δx = 0.00125m. The corresponding bubble size distribution in the turbulent shear layer was within one standard deviation of experimental values. A shortcoming of the approach is that the diameter of the smallest bubbles in the flow is contained within a single cell. When breakup of a large bubble results in several small satellite bubbles, these bubbles may merge in a single cell. The result is a loss of information regarding the smallest bubbles and a potential increase in the minimum bubble size. This problem is apparent in comparisons of bubble frequency, which are underrepresented in the simulations. However, the Sauter mean diameter, or the diameter of a bubble with the same surface area to volume ratio as the entire field of bubbles, is shown to be well represented in the turbulent shear layer (Witt et al., 2014). Some details regarding bubble breakup will be discussed further in Sec. 4.5.

4.3. Ensemble averaged properties

The ensemble averaged air-water properties were previously compared to the experimental data (Witt et al., 2014), and it was determined a sampling time of 15 s at a sampling rate of 20 Hz was sufficient to capture the mean flow characteristics. The same criterion is applied in this work, and some of the relevant mean air-water flow characteristics are outlined below. Misra et al. (2008) found the convergence of turbulence statistics occurred over a much longer time frame than the mean characteristics. Additionally, the experimental data used for validation did not contain any turbulence statistics (Murzyn et al., 2005), and several comparable *Fr* jumps in the literature have significantly higher Reynolds numbers, making direct comparisons difficult (Resch and Leutheusser, 1972; Liu et al., 2004). Thus, in this section only qualitative comparisons of turbulence statistics are made with the literature.

4.3.1. Air-water properties

The mean free surface elevation for all jumps is shown in Figure 4.3 compared with the mean free surface obtained by Murzyn et al. (2005). The instantaneous and mean free surface elevations are taken as the maximum elevation where $\varphi = 0.5$ and $\bar{\varphi} = 0.5$, respectively. Near the toe the free surface exhibits a high degree of intermittency, frequently entraining large air pockets while splashing violently. A high variability in φ is observed in both simulations and experiments. A standard deviation of up to $0.7d$ in free surface elevations has been observed in hydraulic jumps of comparable Fr (Chachereau and Chanson, 2011b). As an attempt to quantify free surface intermittency, Fig. 3 includes error bars that span the region in simulations where $0.2 < \bar{\varphi} < 0.8$. The VoF approach spreads an interface across one or two cells, meaning a higher φ may be expected in regions of intense breakup and bubble generation. This is indeed the case nearest the toe, where the free surface is increased over experimental values. Further downstream, the simulated and experimental free surface elevations converge to similar values.

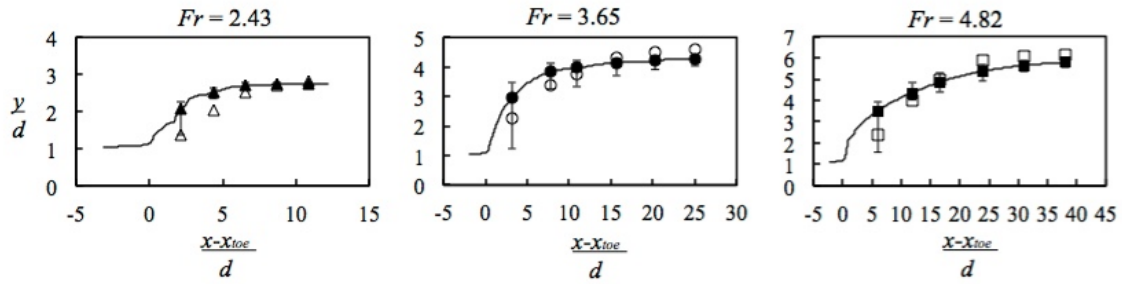

Figure 4.3. Mean free surface values from three simulations compared to experiments. Filled markers indicate simulation results while open markers indicate the elevation where $\bar{\varphi} = 0.5$ from Murzyn et al. (2005). Positive and negative error bars indicate simulation elevations with $\bar{\varphi} = 0.2$ and $\bar{\varphi} = 0.8$, respectively.

Average air concentration color contours are displayed in Figure 4.4 for Fr = 4.82. Also plotted are vertical profiles of the average air concentration for the simulation and experiment (Murzyn et al., 2005) up to the elevation where $\bar{\varphi} = 0.5$. Between $5d$ and

10d downstream of the jump toe, air concentration profiles increase in line with experiments from the lower wall up to the shear layer, but overpredict the average free surface elevation by approximately 1d. In experiments, turbulence in the roller region produces a foamy structure where thin films of liquid separate neighbor bubbles (Chanson and Brattberg, 2000), leading to higher air concentrations. While full resolution of these structures is not possible, the simulations captured qualitatively the characteristic vertical air concentration profile at all locations, and showed improved air concentrations downstream after bubbles experience breakup in the shear region.

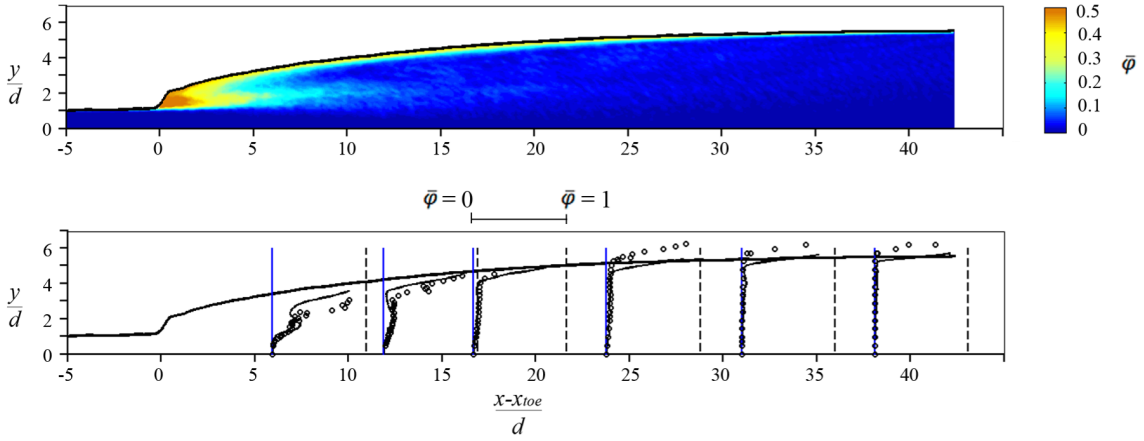

Figure 4.4. Air characteristics for $Fr = 4.82$. Top: color contours of average air concentration. Bottom: comparison between simulations (solid black line) and experiments (open circles, Murzyn et al., 2005).

Mean horizontal and vertical velocity fields are presented in Figure 4.5. The fields are overlaid with lines indicating the maximum and minimum horizontal velocities, herein referred to as the turbulent shear region, and u,v velocity vectors. The velocity profiles show similarity to a wall jet, with a maximum velocity in the lower shear region near the wall, and a decreasing velocity ascending vertically into the roller, where negative horizontal and vertical velocities contribute to recirculation. Vertical velocities are lower than horizontal velocities, as expected. Vertical velocities show a distinct spatial variability, with negative values in the roller and positive values near the toe, similar to the structure observed by Svendsen et al. (2000) for $Fr < 2$ and Lin et al. (2012)

for $Fr > 2$. In the latter, positive vertical velocities at the toe were obtained from tracking the motion of bubbles. The similarity of results obtained numerically suggests the toe is highly aerated, and the vertical motion of the toe is influenced to a certain extent by the volume of air it contains.

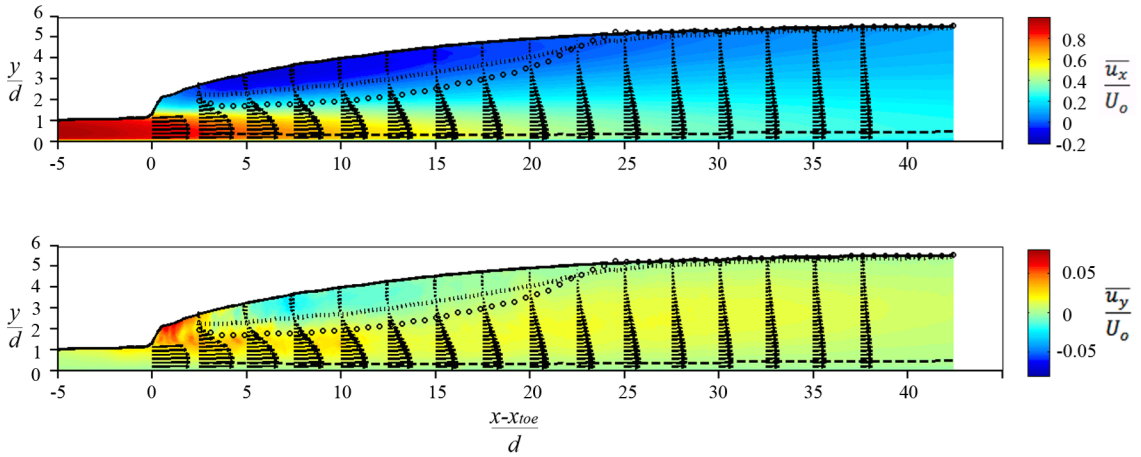

Figure 4.5. Mean velocity profiles for $Fr = 4.82$. All values are shown under the mean free surface, $\bar{\varphi} = 0.5$, demarked by the solid black line. Top: color contours of average u_x velocity. Bottom: color contours of average u_y velocity. Maximum and minimum horizontal velocity are indicated by '---' and '|||' respectively, while 'o' indicates the roller thickness $r(x)$ (Eq. 4.15).

Roller thickness is estimated as the total depth of fluid with zero mass flux downstream using (Castro-Orgaz and Hager, 2008)

$$\int_{y}^{y+r(x)} \overline{u}(x,y)\mathrm{d}y = 0\ , \tag{4.15}$$

where $r(x)$ is the thickness of the roller, and the integral is carried out from the mean free surface extending down. Roller thickness grows from the toe to a maximum approximately halfway through the roller, before decreasing at the end of flow reversal. While others have demarked the roller depth as the elevation of zero velocity (e.g. Lin et al., 2012) , the elevation of zero mass flux more closely aligns with the maximum turbulent and vorticity statistics, as shown below. The roller length obtained in this

fashion is approximately 24.5d, very near the estimated value of 26.5d predicted by Hager et al. (1990) and within the ±2d expected standard deviation.

4.3.2. Turbulent properties

Several attempts have been made to characterize the turbulence characteristics in hydraulic jumps with $Fr > 2$. Obtaining accurate measurements in the bubbly roller region has been a persistent challenge owing to the two-phase nature of the flow. Resch and Leutheusser (1972) were the first to overcome this problem by employing hot-wire anemometers to obtain limited measurements of fluctuating velocity components. Results obtained using micro acoustic Doppler velocimetry showed high noise levels in the roller, and the fluctuating free surface elevation limited the sampling volume to the shear region below the roller (Liu et al., 2004). Their results displayed similarity in turbulence intensities for $2.0 < Fr < 3.32$, with strong turbulence observed near the toe that decayed rapidly downstream. Use of particle image velocimetry (PIV) techniques have had limited success, however, the high void fraction in the roller conceals the visual field of particles leading to poor image quality (Lennon and Hill, 2006). Some cross-correlation analyses between free surface turbulence characteristics and internal air characteristics have been carried out with acoustic displacement meters and conductivity probes, respectively (Murzyn and Chanson, 2007; Chachereau and Chanson, 2011b). Recently, Lin et al. (2012) employed a PIV technique in the non-aerated region and a bubble image velocimetry (BIV) technique in the aerated region to characterize the turbulent structure of the flow. The turbulence statistics were presented in terms of bubble velocities, and showed some similarity with previous experiments. It is clear a complete picture of turbulence in the jump is still emerging.

Non-dimensional turbulence characteristics for $Fr = 4.82$ are presented in Figure 4.6. Color contours of longitudinal turbulence intensity, $\sqrt{\overline{u'^2}}/U_o$, vertical turbulence intensity, $\sqrt{\overline{v'^2}}/U_o$, in-plane equivalent Reynolds stress, $-u'v'/U_o^2$, and in-plane

equivalent turbulence intensity, $\sqrt{\overline{u'^2}+\overline{v'^2}}/U_o$, are computed from the velocity field, while color contours of normalized turbulent kinetic energy, $\sqrt{\overline{k}}/U_o$, and energy dissipation, $\varepsilon d/U_o^3$, are obtained from the realizable k-ε turbulence model. As expected, turbulence intensities are strongest near the toe and decrease downstream. Longitudinal and vertical turbulence intensities (Figures 4.6a, 4.6b) are maximum at the toe, with vertical intensities peaking just beneath the free surface and longitudinal intensities peaking at the impingement elevation, $y/d = 1$. A region of high longitudinal turbulence intensity extends into the jump and corresponds closely with the elevation of roller thickness ('o'), suggesting the magnitude of turbulence intensity is strongly influenced by the magnitude of negative velocity in the roller. Positive Reynolds stresses ($-u'v' < 0$) are observed near the toe and above the impingement elevation (Figure 4.6c), extending horizontally into the roller, while a few contours of negative Reynolds stresses are present at the impingement point. Lin et al. (2012) similarly observed a small region of negative Reynolds stress immediately downstream of the toe at the impingement elevation, and positive Reynolds stresses in the roller and turbulent shear region. Several others have not been able to characterize Reynolds stress at the toe due to measurement uncertainty, and report positive Reynolds stresses in the turbulent shear region (Resch and Leutheusser, 1972; Liu et al., 2004). Qualitatively, all normalized turbulence intensities are of the same magnitude as those obtained by previous authors for $Fr > 2$.

Maximum turbulence intensities reach a peak at the toe and decrease quickly downstream (Figure 4.7). 2D and 3D results show a degree of similarity when distance is normalized by the depth of the jump, d_{tw}, measured downstream from the roller. The strength of the jump has an effect on the strength of turbulence intensity. For $Fr = 2.43$, normalized turbulence intensities and Reynolds stresses are everywhere less than those of $Fr = 3.65$ and $Fr = 4.82$. Asymptotic values of turbulence intensity are approached moving downstream from the toe, with Reynolds stresses decaying to a minimum quicker than longitudinal and vertical turbulence intensities.

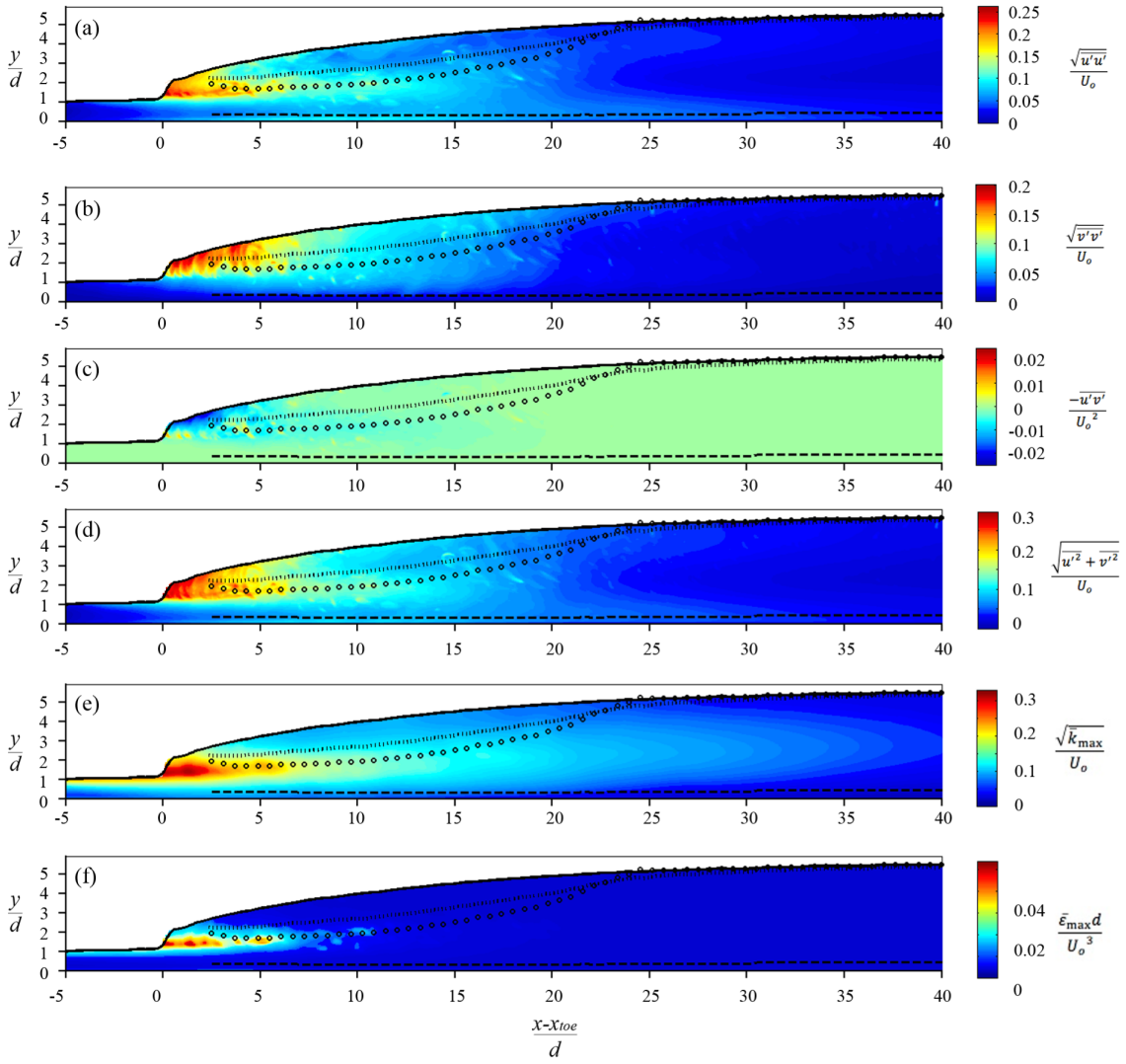

Figure 4.6. Color contours of turbulent properties for Fr = 4.82. Symbols see Figure 4.5.

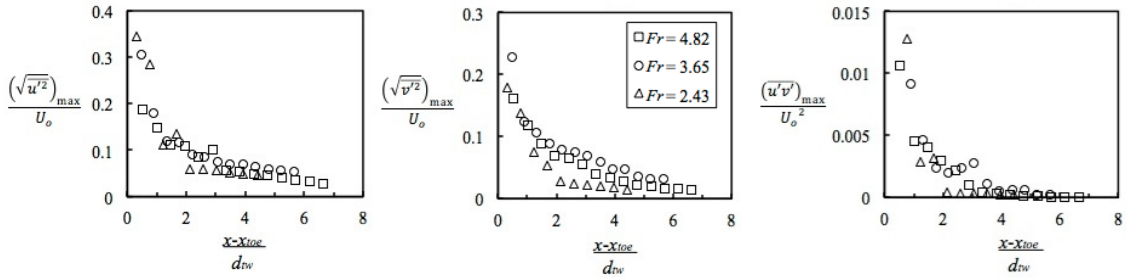

Figure 4.7. Maximum normalized longitudinal (left), vertical (center), and Reynolds (right) turbulence intensities.

Turbulent kinetic energy calculated from the realizable k-ε model for all Fr jumps shows a reasonable degree of self-similarity, as does energy dissipation (Figure 4.8). Peak values are reached at the toe and decay downstream. Turbulent kinetic energy decrease linearly in the transition region of the jump ($(x\text{-}x_{toe})/d_{tw} > 2$), corresponding closely to a line of best fit obtained from experiments (Liu et al., 2004). Higher values of turbulent kinetic energy are seen surrounding the elevation of the roller depth. Turbulent kinetic energy dissipation decreases more rapidly than turbulent kinetic energy. Maximum values in the transition region are less than 10% of those seen at the toe. Inherent difficulties persist in obtaining energy dissipation estimates experimentally. Several authors have used a two-step process to first estimate the one dimensional longitudinal turbulent velocity spectrum assuming Kolmogorov's theory of local isotropic turbulence, and second apply Taylor's frozen turbulence hypothesis to convert the spectrum into a wave number (Liu et al., 2004; Cheng and Chan, 2013). These results appear visually similar to numerical results obtained using a realizable k-ε turbulence model, indicating turbulence is well represented in the simulations.

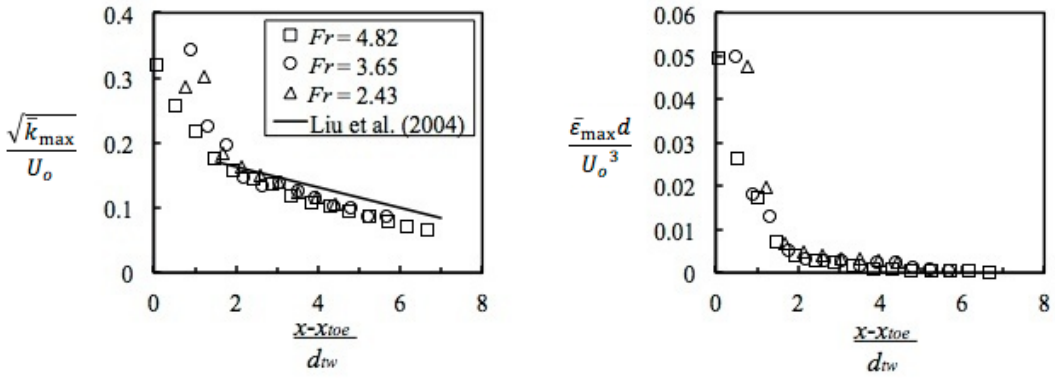

Figure 4.8. Maximum average normalized turbulent kinetic energy (left) and turbulent energy dissipation (right) for all simulated jumps.

4.3.3. Vorticity

Normalized time-averaged spanwise vorticity is shown in Figure 4.9 for *Fr* = 4.82. Maximum positive vorticity is located at the toe, in contrast to lower *Fr* jumps (< 2) where a maximum is observed approximately 10% of the roller length downstream from the toe. Greater recirculation in higher *Fr* jumps (> 2) creates a strong shear layer immediately at the toe, where vorticity is concentrated within a thin layer. Vorticity diffuses downstream, corresponding with the evolution and growth of vortices originating at the impingement point. The diffuse region is bound between the lines of maximum and minimum positive horizontal velocities, where the peak vorticity tracks closely with the roller depth (Eq. 4.15) until approximately 15*d*. The elevation of minimum horizontal velocity serves as a boundary between the largely irrotational flow of the roller and the highly rotational flow in the shear layer. A thin boundary layer is present at the lower wall, where a large negative spanwise vorticity develops due to the no-slip wall boundary condition. On average, positive vorticity is contained with the shear region, with irrotational flow in the roller above and the lower shear layer below. However, the shear layer interacts with the bottom wall and the free surface periodically. These interactions are analyzed further in the following section.

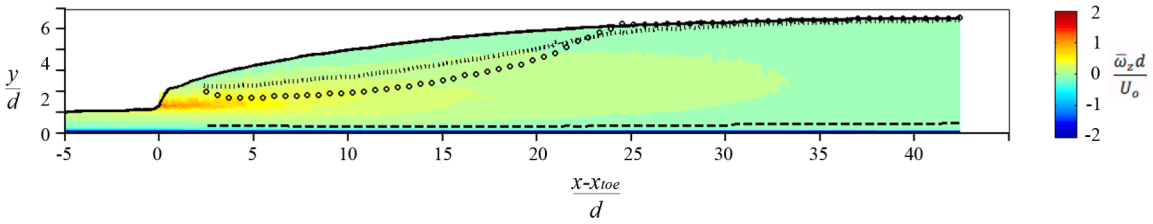

Figure 4.9. Mean normalized spanwise vorticity for *Fr* = 4.82. Symbols see Figure 4.5.

4.4. Instantaneous vorticity

The presence of large spanwise vortices, commonly referred to as coherent structures, is a defining characteristic of the hydraulic jump (Peregrine and Svendsen, 1978; Hoyt and Sellin, 1989; Long et al., 1991; Mossa and Tolve, 1989; Rodriguez-Rodriguez et al., 2011; Witt et al., 2014). Vortices are generated when the shear layer becomes unstable and experiences roll-up. In this section, the instability of the shear layer and the corresponding behavior of spanwise vortices are examined.

4.4.1. Instantaneous vorticity at the toe

The toe sits atop a thin, highly aerated shear layer, with significant spanwise vorticity in relation to the roller and the impinging jet. This in agreement with the experimental observation of Svendsen et al. (2000) for jumps with $Fr < 2$, though the region of high air content and spanwise vorticity both appear to extend further downstream. Large pockets with between 5-100% air content are intermittently gulped in between successive pulses of the roller. Vorticity is generated below these pockets, as they sit directly in the region where positive horizontal flow transitions to negative horizontal flow. The extent of air within the shear layer is highlighted by visualizing the same instant in time contoured by various distributions of γ (Figure 4.10). The highly aerated shear region penetrates $5d$ into the jump and is bounded by bubbly, low velocity roller fluid above and high velocity inflow devoid of bubbles below. Although the roller contains many bubbles, their effect on recirculation appears to be limited as evidenced by continuity of the vertical velocity profile.

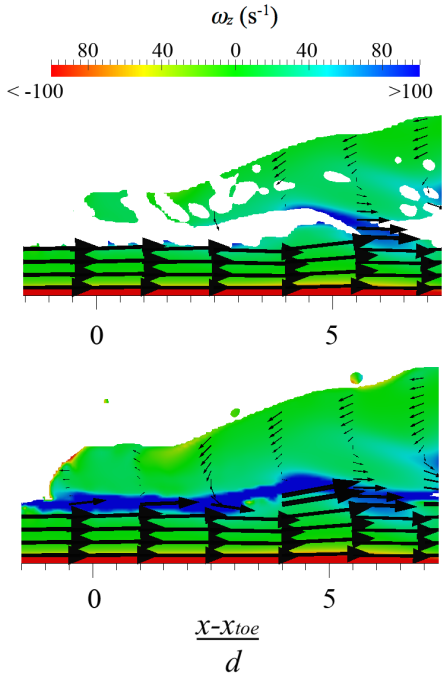

Figure 4.10. Instantaneous view of the toe of the jump on an *x*-*y* slice down the center of the domain. Top: fluid domain is shown for $\gamma > 0.99$ (white space indicates gas phase, i.e. bubbles or air). Bottom: fluid domain is shown for $\gamma < 0.01$. The jump is colored by ω_z (s^{-1}) and vectors depict (u_x,u_y).

The elevation of maximum positive vorticity is just below the region of highest air content nearest the toe, and the elevation of maximum shear is bounded within the highly aerated layer (Figure 4.11). Experimentally, the elevation of maximum shear is correlated with the elevation of maximum bubble count rate, which is consistently below the elevation of maximum air content (Chanson, 2010). Observations of the numerical simulation indicate that larger pockets of air entrained at the toe sit atop the shear layer, contributing to increased air concentrations above the shear layer. The increase in bubble frequency below the elevation of maximum air content may indicate large bubbles are sheared along the direction of maximum shear, producing smaller bubbles easily influenced by the momentum of the impinging jet. Small bubbles do not have sufficient rise velocity to escape the shear layer, and track closely with the streamline that extends from the impingement point of the upstream jet into the roller, which sits below the elevation of maximum shear.

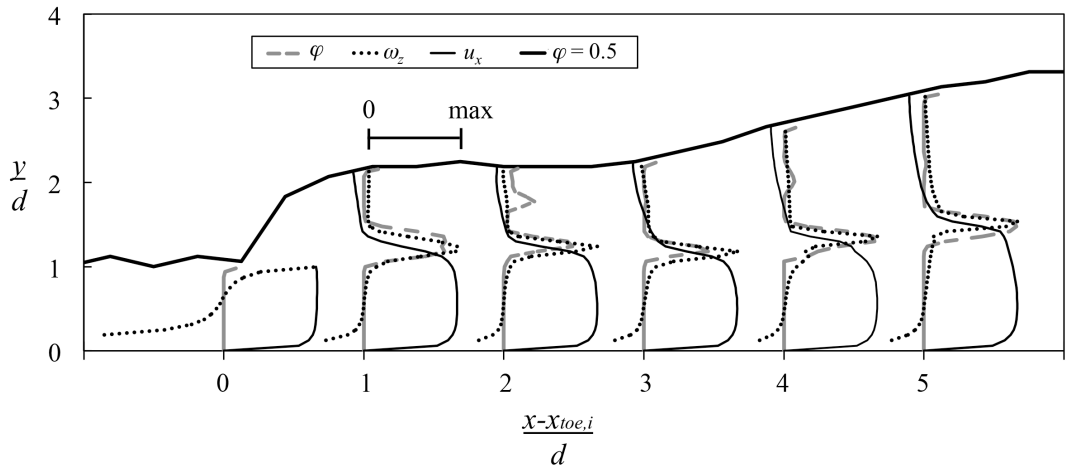

Figure 4.11. Instantaneous φ, ω_z, and u_x profiles at the toe of the jump. All values are normalized by their maximum value at the given longitudinal location.

4.4.2. Shear layer instability

The well-defined shear layer exists when the roller is cascading a steady supply of bubbly fluid towards the toe, and the free surface exhibits a fairly uniform rise from the toe to the end of the roller. In this regime the shear layer extends unperturbed a significant distance into the roller, instabilities are damped by a sufficient weight of fluid in the roller, and vortices are shed a sizable distance downstream from the instantaneous position of the toe. In time, the dynamic relationship between the roller and shear layer leads to instabilities that develop closer to the toe. The toe becomes supply limited and is forced downstream. This mechanism is highlighted in Figure 4.12. At $t^* = 0$, the shear layer instability occurs at approximately 5.25d. At $t^* = 0.04$ s the instability moves closer to the toe, occurring at 3.75d. At $t^* = 0.13$s and $t^* = 0.19$ s the instability develops at 3d. Eventually the instability develops in a region with little fluid in the roller to entrain (2d at t* = 0.23 s), the vortex interacts violently with the free surface, and the toe oscillates downstream. A clearer understanding of this relationship is obtained by analyzing the surface-normal and surface-parallel velocities of the free surface, and through a cross-correlation analysis of the shear layer and free surface elevations.

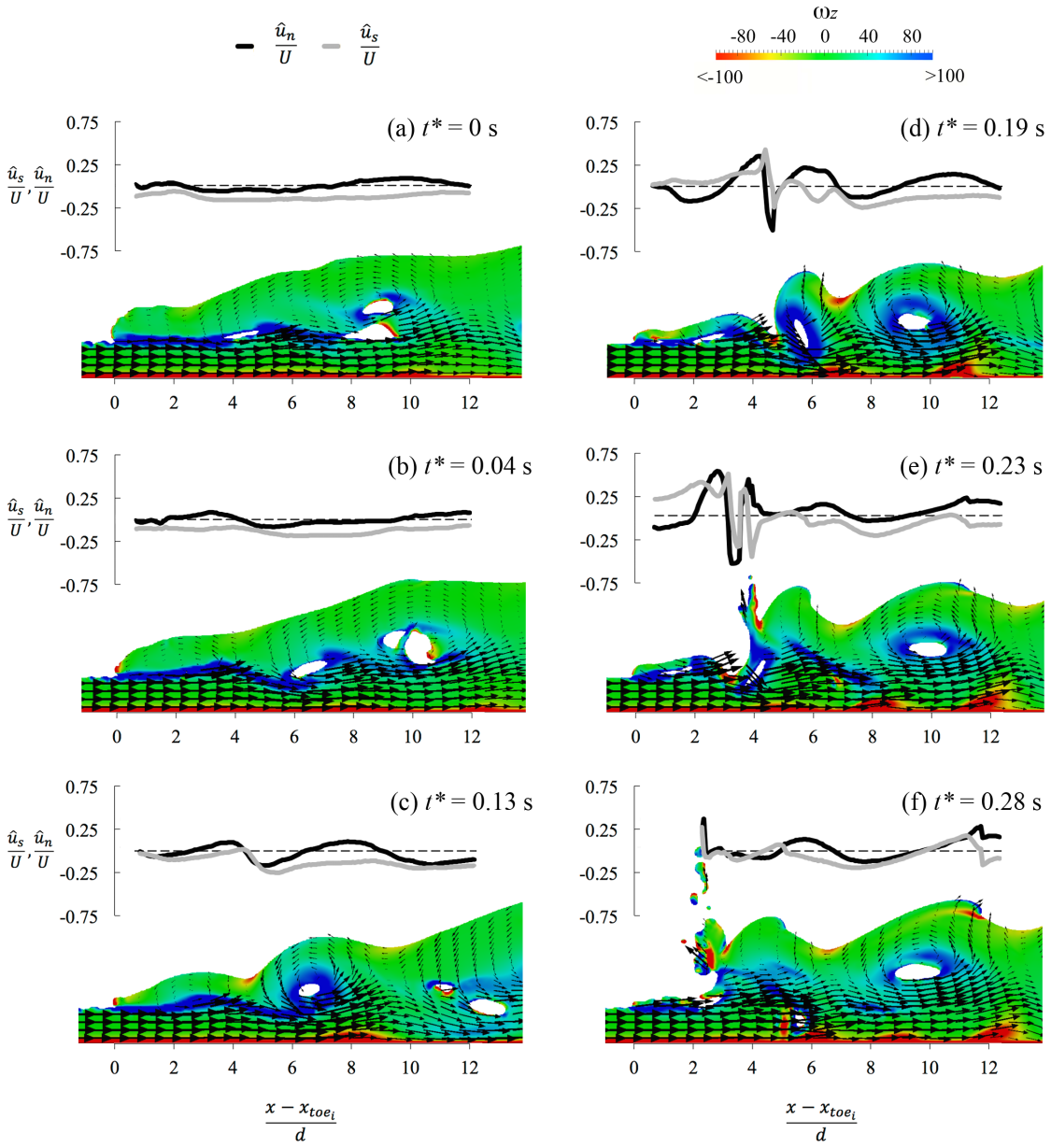

Figure 4.12. Successive roll-ups of the shear layer shown in relation to t^*=0. The shear layer is marked by dark blue indicating maximum vorticity, and the roll-up is viewed as the first location downstream from the toe where the shear-layer exhibits a pronounced downward curvature. Each roll-up produces a vortex that is advected downstream, and the next roll-up occurs closer to the toe. The jump is colored by ω_z and overlaid with u, v velocity vectors. Normalized surface-parallel and surface-normal velocities are plotted above each jump. The instantaneous position of the toe is set as 0 on the x-axis, though the total distance traveled by the toe from (a) to (f) is 2.4d.

4.4.2.1 Surface normal and parallel velocities

Free-surface characteristics can be analyzed by looking at the instantaneous surface parallel and surface normal velocities (Misra et al., 2008), computed on the γ = 0.5 surface as

$$\hat{u}_s = u_x \cos\theta + u_y \sin\theta \,, \tag{4.16}$$

$$\hat{u}_n = -u_x \sin\theta + u_y \cos\theta \,, \tag{4.17}$$

respectively, where θ is the angle tangent to the mean surface with respect to the x-axis, estimated from

$$\theta = \tan^{-1}\left[\frac{\partial(\eta(x))}{\partial x}\right], \tag{4.18}$$

and $\eta(x)$ is the instantaneous free surface elevation at $\boldsymbol{x}$, or the elevation where φ = 0.5. The graph overlay at each time step of Figure 4.12 shows the corresponding free surface normal and parallel velocities, normalized by the velocity of the upstream jet. The surface is relatively stable when the shear layer penetrates unperturbed into the roller, and $\hat{u}_n$ varies smoothly from the toe up the roller. The surface normal velocity is negative as a steady stream of fluid cascades down the front of the roller and provides a source of fluid for the toe. Regions of pronounced positive $\hat{u}_n$ are seen at t^* = 0.13s, where a large vortex approaches the free surface. The magnitude of $\hat{u}_n$ increases with each successive vortex created, while the corresponding longitudinal location advances towards the toe. A sharp difference in magnitude and sign is seen near the toe at t^* = 0.19s, where a vortex roll-up very near the free surface and a strong perturbation at the toe occur simultaneously. A strong negative $\hat{u}_n$ is seen on the upstream side of the vortex, as it entrains most of the fluid from the roller directly above. The roller is effectively thinned and $\hat{u}_n$ reverses sign to align with the incoming jet, leading to a collision of surfaces moving with opposing velocities.

Surface parallel velocity shows a similar trend. At t^* = 0 and t^* = 0.04 s, $\hat{u}_s$ is

entirely negative as the roller cascades unperturbed. At $t^* = 0.19$ s, $\hat{u}_s$ directly above the toe makes a marked shift from negative to positive. This transition coincides with a decreasing roller depth. The constant source of flow from the downstream portion of the roller is interrupted, cutting off the driving recirculatory force of the roller and causing the aerated shear layer to pull all fluid resting above in the direction of the flow. The shear layer roll-ups nearer to the toe result in strong oscillations in $\hat{u}_s$, eventually leading to a sharp discontinuity when the roll-up occurs near the toe. As the roller recovers from this strong perturbation, both $\hat{u}_s$ and $\hat{u}_n$ return to entirely negative values downstream with this process repeated semi-periodically.

Vortices formed near the toe initially take an elliptical shape, oriented with the major axis in the direction of flow. A shear layer roll-up near the toe changes the orientation of the vortex, aligning the major axis with the direction of maximum strain (Figure 4.12d), in agreement with the experimental observations of Misra et al. (2005) for $Fr < 2$. This orientation is thought to be partly responsible for the increased Reynolds stress near the toe, being more efficient at extracting energy from the flow (Hussain, 1986). The resulting strong turbulent ejections are similar in magnitude and location to those observed experimentally (Murzyn and Chanson, 2009), and it is thus inferred that the peak of free-surface fluctuations near the toe is correlated with a roll-up of elliptical vortices.

4.4.2.2 Shear layer instabilities and the free surface

A spatial cross-correlation analysis between the shear layer elevation and both free surface elevations and free surface velocities provides a quantitative measure of their dynamic behavior. The mean shear layer elevation, $\overline{y_s}$, is defined as the line occupied by the mean maximum spanwise vorticity in the liquid phase. This elevation approximates the centerline of passing vortices and correlates closely with the mean inflexion point of the velocity profile, where the shear is at a maximum (Figure 4.13). A velocity profile with an inflexion point is prone to significant instabilities (Michalke, 1965), and instantaneous fluctuations about the mean inflexion point can serve as a measure of shear

layer instability (Zhao et al., 2000). For hydraulic jumps of $Fr < 2$, Rodriguez-Rodriguez et al. (2011) approximated the maximum shear using the slope of the velocity profile between the locations where $\overline{u_x} = 0.35\ U_o$ and $\overline{u_x} = 0.1\ U_o$. The mean shear layer elevation $\overline{y_s}$ falls within these values for most of the jump, and is thus chosen to represent the instantaneous shear layer.

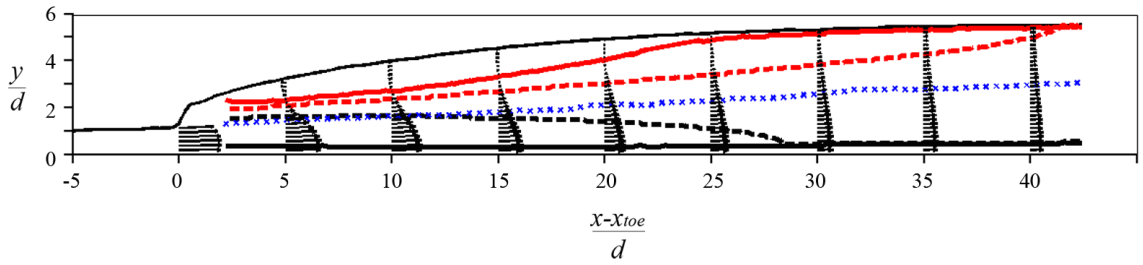

Figure 4.13. Mean velocity components for $Fr = 4.82$ compared with the mean shear layer elevation, $\overline{y_s}$. Upper and lower solid lines indicate minimum and maximum positive $\overline{u_x}$, respectively, upper and lower dashed lines represent $\overline{u_x} = 0.35U_o$ and $\overline{u_x} = 0.1U_o$, respectively, and the center 'x' indicates $\overline{y_s}$.

A low-pass band filter is commonly employed in experimental analyses of air-water correlations in the hydraulic jump to smooth spurious high-frequency signals (Murzyn and Chanson, 2007; Chachereau and Chanson, 2011b). The sampling rate in the numerical simulations was equal to the equivalent experimental cutoff frequency, thus a moving-average filter was employed. The spatial cross-correlation function then takes the form

$$R_{y_s'\eta'}(r) = \frac{1}{L_x}\int_{-L_x}^{L_x} y_s'(x+r,t)\ \eta'(x,t)\ \mathrm{d}x\,, \tag{4.19}$$

where $R_{y_s'\eta'}$ is the cross-correlation function, y_s' is the filtered instantaneous fluctuation about the average shear layer elevation $\overline{y_s}$, η' is the filtered instantaneous fluctuation about the average free surface η, and r denotes the spatial lag. The cross-correlation function was obtained for each time step and averaged over the entire sampling time.

Cross-correlations for several variables were carried out, with the subscript of R representing the variable of interest substituted into Eq. 4.19.

The normalized correlation function $R_{y_s'\eta'}$ is shown in Figure 4.14. The results exhibit a periodic shape with two large positive values separated by a negative value. The peak at a distance of 1d shows a small spatial lag in the response of the free surface to the shear layer roll-up, and the strong positive value indicates a significant correlation between the shear layer elevation and the free surface elevation. The periodicity of the function represents the tendency of vortices to travel downstream at a constant rate. These vortices frequently interact with the free surface, particularly during pairing events when thy begin co-rotating and grow in size. The correlation function loses some periodicity near the end of the roller region, as vorticity becomes diffused.

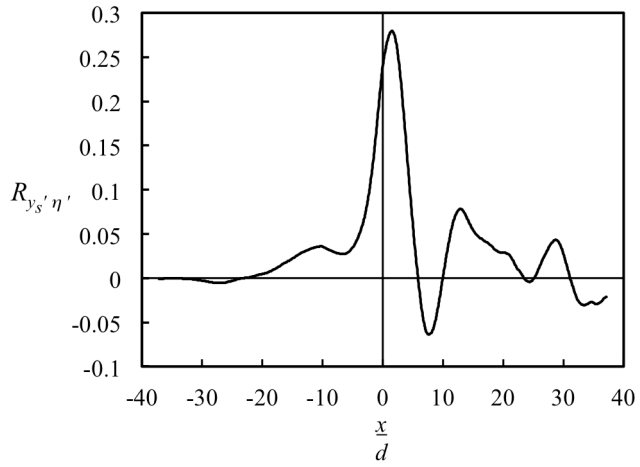

Figure 4.14. Time-averaged normalized cross-correlation of shear layer elevation and free surface elevation.

A representative snapshot of this behavior is shown in Figure 4.15. Color contours of spanwise vorticity are overlaid with lines representing the mean and instantaneous free surface and shear layer elevations. A downstream fluctuation of the toe (x-$x_{toe,i} > 0$) results in a roll-braid structure, with distinct regions of coherent spanwise vorticity. The shear layer roll-up at the toe results in an upward sloping instantaneous

shear layer from 5d to 8d, cutting through the center of the vortex and peaking in elevation at the downstream side of the vortex. The instantaneous shear layer then descends through the braid region to the upstream side of the next vortex, tracking through the center to a higher elevation downstream. At each peak in the instantaneous shear layer, a corresponding rise in the instantaneous free surface is observed slightly upstream, roughly corresponding to the 1d lag seen in Figure 4.14. The free surface fluctuation peaks between the center and downstream side of the vortex, corresponding to a region of strong positive vertical velocity.

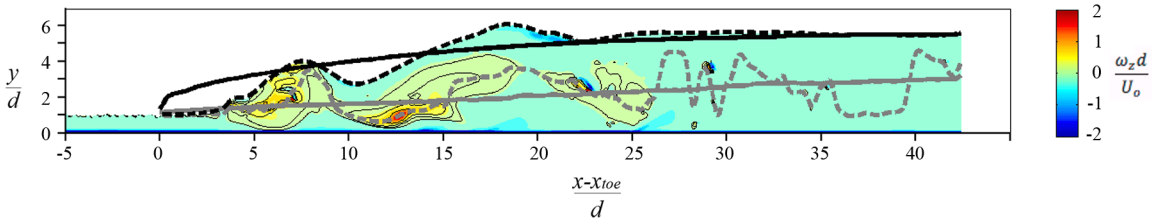

Figure 4.15. Color contours of spanwise vorticity during a shear layer roll-up. Mean free surface and shear layer elevations are shown as black and gray solid lines, respectively, while instantaneous free surface and shear layer elevations are shown as black and gray dashed lines, respectively.

The normalized spatial auto-correlation of y_s' and cross-correlation of y_s' with $\hat{u}_n'$ and $\hat{u}_s'$ are shown in Figure 4.16. A positive correlation indicates the shear layer fluctuates vertically in tandem with a positive surface normal velocity fluctuation, or an upstream surface parallel velocity fluctuation. $R_{y_s'y_s'}$ exhibits some periodicity, indicating the initial shear layer roll-up is preserved downstream in the form of traveling vortices. $R_{y_s'\hat{u}_n'}$ displays a degree of periodicity similar to that observed in Figure 4.14. The peaks and troughs are shifted slightly downstream, however, and the maximum correlation is seen at a zero spatial lag, indicating shear layer fluctuations are strongly correlated with free surface perturbations. $R_{y_s'\hat{u}_s'}$ shows a markedly different trend. A negative correlation is observed at zero spatial lag, meaning an increase in the shear layer elevation slows the spill of fluid down the roller face, and a decrease results in greater

spill velocity. This trend persists until approximately 6*d*, where the correlation becomes positive. A maximum at 11*d* corresponds with peaks in $R_{y_s'y_s'}$ and $R_{y_s'\hat{u}_n'}$, indicating the periodic creation of vortices at the toe culminates in some intense interactions between vortices and the free surface approximately halfway to the end of the roller. This location is also situated in a region of frequent vortex merging (Witt et al., 2014), meaning the shear layer instability at the toe is strongly correlated with, and responsible for, the underlying vortex structure downstream.

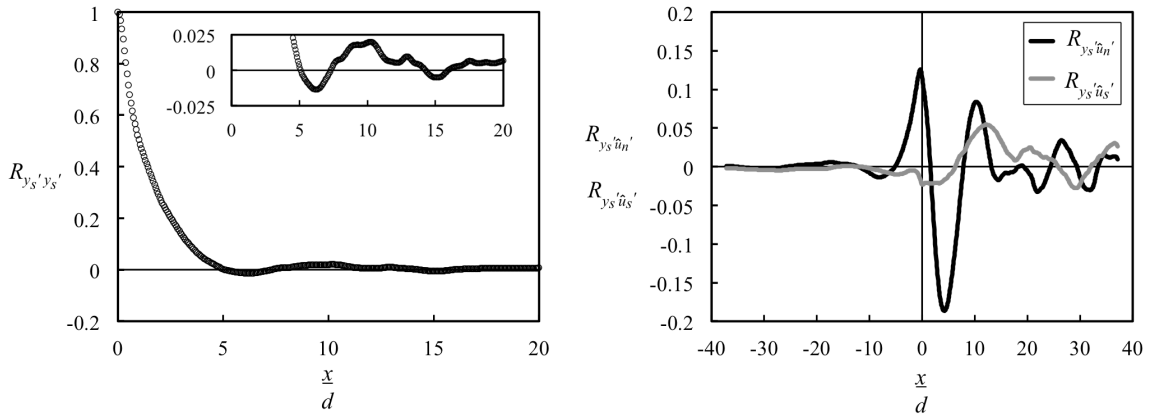

Figure 4.16. Left: normalized spatial auto-correlation of y_s'. Inset shows an expanded view of the periodicity downstream. Right: normalized spatial cross-correlation of y_s' and $\hat{u}_n'$, $\hat{u}_s'$, respectively.

4.4.3. Vorticity near the lower wall

When large spanwise vortices descend into the wall boundary layer, they interact with and shed vorticity from the lower wall. Interactions between spanwise vortices and the wall boundary layer are persistent in 3D numerical simulations (Figure 4.17). The lower wall is colored by the magnitude of the normal gradient of velocity at the wall, d***u***/dn, and indicates the extent to which the near-wall velocity is influenced by passing vortical structures. A clear increase in d***u***/dn is apparent when strong spanwise vorticity is present at the wall. Vortices descending towards the wall have a tendency to accelerate the underlying fluid longitudinally. Immediately downstream from this local

acceleration, d***u***/dn exhibits a distinct decrease. This transition region is characterized by a large upwelling of fluid from the wall boundary layer into the shear layer, and a near separation of the wall boundary layer as the streamwise velocity approaches zero. The rising fluid is characterized by a strong negative ω_z, which arises due to the steep vertical velocity gradient at the wall. This is a notable departure from $Fr < 2$ hydraulic jumps, where the bottom boundary layer does not influence the shear layer (Hornung et al., 1995; Misra et al., 2008).

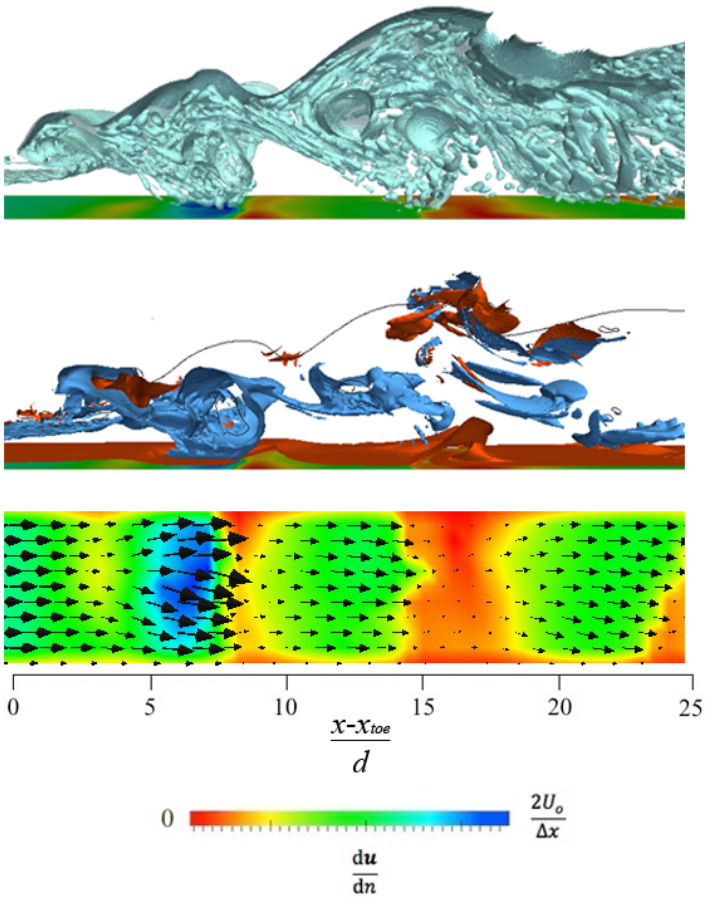

Figure 4.17. Instantaneous depiction of lower wall shear, d***u***/dn. Top: three-dimensional isosurface of volume fraction about $\gamma = 0.95$ to represent bubbles. Middle: three-dimensional isosurface of $\omega_z = 0.4d/U_o$ (blue) and $\omega_z = -0.4d/U_o$ (orange) along with a solid black contour of $\gamma = 0.5$ to represent the free surface. Bottom: top view of lower wall colored by d***u***/dn with velocity vectors indicating direction of motion in the grid node above the wall.

The streamwise component of d$\boldsymbol{u}$/dn, du_x/dn, exhibits an oscillating pattern that tracks closely with the passing of vortices (Figure 4.18). Plotting the instantaneous vorticity along $\bar{y}_s$ gives the approximate location of each passing vortex. This location coincides with the peak of du_x/dn at each longitudinal location. A passing vortex will increase du_x/dn above the mean value, while the upwelling region causes a decrease below the mean value. At the toe, vorticity is high at the impingement point but does not influence the wall shear. Once the roll-up occurs and the vortex descends towards the wall the influence becomes pronounced and tends to persist downstream, even when the vorticity has decreased considerably.

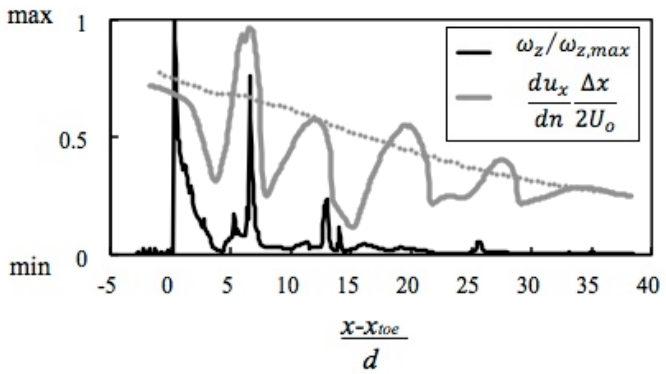

Figure 4.18. Instantaneous normalized du_x/dn, and $\omega_z(x, \bar{y}_s)$ corresponding to Figure 4.17. The mean value of du_x/dn is shown as a dashed line.

The fluid rising from the wall boundary layer is typically devoid of bubbles, as it sits below the impingement elevation of the roller and the upstream jet and represents the incident flow. An experimental analysis posited a lack of bubbles near the lower wall in the roller might be due to buoyancy effects (Waniewski et al., 2001). While buoyancy acts to lift bubbles out of the shear layer, the upwelling of non-bubbly fluid into the shear layer clearly contributes to regions of decreased bubble concentration. In the next section, additional mechanisms contributing to spatial inhomogeneity in the bubble field are explored.

4.5. Bubble clustering

Bubble clustering within the hydraulic jump has recently been explored experimentally through an analysis of air-water time scales (Chacherau and Chanson, 2011b). From these experiments, it is hypothesized that bubble clusters may be related to vorticity, bubble-turbulence interactions, breakup, or energy dissipation, though the nature of these relationships has not been determined. The present numerical approach is not able to resolve the smallest bubbles in the flow, though resolution of the average bubble diameter and total entrained air is sufficient to warrant a quantitative analysis of clustering and bubble-turbulence relationships within the hydraulic jump.

Two primary mechanisms contribute to bubble clustering in air-water flows: turbulence and bubble wake dynamics. Within shear flows with large scale coherent structures, experimental and numerical studies have shown that vortices induce coherent motion of larger bubbles, while entraining and accumulating smaller bubbles into the vortex core (Tio et al., 1993; Sene et al., 1994). The interaction between bubbles and eddies also leads to breakup, which produces a cluster structure with daughter bubbles of various sizes (Clift et al., 1978; Liao and Lucas, 2009). Clusters are also formed when freely rising bubbles capture surrounding bubbles into their wake and accelerate them past their predicted rise velocity (Stewart, 1995; Brücker, 1999). Large coherent structures and rising bubbles of various shapes are present in the hydraulic jump, thus we expect to see some preferential clustering due to turbulence and wake dynamics.

The challenge presented by bubbles within the hydraulic jump is that they are neither perfectly spherical, nor rising of their own accord through quiescent fluid, nor are they immune to breakup and coalescence. These simplifications, made to ease experimental and numerical restraints on attaining high fidelity data, are not valid for the current work and present a unique challenge to characterizing bubble behavior within the jump. Experimental studies on the hydraulic jump have implemented intrusive probes to explore bubble cluster patterns and their relationship with inflow properties (Chanson, 2007b; Chanson, 2010; Gualtieri and Chanson, 2010). If two bubbles are separated by a water chord whose length is less than the leading bubble diameter, they are deemed part

of a bubble cluster. A limitation of intrusive probes is that only bubble clusters traveling longitudinally with the mean flow (Chanson 2010; Gualtieri and Chanson, 2010), or side-by side (Sun and Chanson, 2013) are detected, and the resulting analysis seeks to detect inhomogeneity in 1D data. The justification for this technique is that a secondary bubble may be in the 'near-wake' region of a leading bubble, and is subject to influence from the leading bubble, if it trails longitudinally by a characteristic length or time scale (Chanson, 2010).

There are two underlying assumptions to address when applying a 1D 'near-wake' technique to bubbles within the hydraulic jump: bubble alignment and separation length. First, a longitudinal alignment is influential for particle-laden flows that are predominantly unidirectional, oriented horizontally (Noymer, 2000). Bubbles exhibit a rise velocity, which adds a mean vertical component of motion to their path when they have sufficient buoyancy to escape the shear layer (Sene et al., 1995). Small bubbles traveling with the flow in a hydraulic jump will not have a significant rise velocity component, and can realistically serve as tracers for the mean flow (Lin et al., 2012). They are strongly influenced by vortical structures, which alter bubble trajectories and are responsible for some coherent organization of bubbles (Balachandar and Eaton, 2010). Larger bubbles rise out of the mean flow while being transported downstream. The near-wake region behind a large bubble would not be aligned longitudinally with the flow, but would have a substantial vertical component due to the bubble path trajectory.

The second underlying assumption, bubble separation length, is fundamentally related to the particle Reynolds number (Clift et al., 1978), and is significantly less pronounced for bubbles with a small diameter and a low rise velocity. A trailing bubble preferentially clustered with a leading bubble due to wake-induced effects must be aligned with the wake of the leading bubble, the separation length must be less than the 'near-wake' length, and the wake of the leading bubble must be sufficiently strong to influence the trailing bubble (Stewart, 1995; Brücker, 1999). It is difficult to evaluate these criteria experimentally, as intrusive probes cannot capture the relevant flow details.

This section presents some bubble clustering analysis within the simulated hydraulic jump, with a discussion of the relevance of breakup.

4.5.1. Methodology for defining bubble clusters

Two characteristic length scales are required to analyze the extent of bubble clustering: an inter-bubble distance, and a characteristic search radius. A positive correlation between the two may indicate preferential clustering within the jump. Rather than use the water chord length between two bubbles aligned horizontally as an inter-bubble distance, a search radius of length of one equivalent bubble diameter, d_b, is extended normal to the interface and swept around the perimeter of each bubble. This technique maintains the same water chord length equivalent as the 1D technique, but provides the advantage of an in-plane 2D cluster characterization.

The bubble interface is determined by generating a contour map of the instantaneous volume fraction field about $\gamma = 0.95$ through an x-y plane down the center of the domain. This technique was shown to best represent the average simulated bubble diameter within the shear region (Witt et al., 2014). A neighbor bubble with perimeter coordinates that overlap the search radius is considered a cluster to the primary bubble (Figure 4.19). The search radius is obtained from the area of the volume fraction contour, $d_b = (4A_{bp}/\pi)^{1/2}$, where A_{bp} is the area of the primary bubble contour. The separation angle is defined as $\theta = \tan^{-1}[(y_{bn}-y_{bp})/(x_{bn}-x_{bp})]$, where x_b and y_b mark the centroid of each bubble, and the subscripts p and n represent the primary and neighboring bubble, respectively.

While other techniques in the literature define inter-bubble distance as the length between the centroid of the primary and neighbor bubbles, this technique was observed to bias the results toward a particular orientation within the hydraulic jump. A large majority of bubbles are deformable and display an elliptical form near the toe of the jump. In terms of a difference in respective centroid coordinates, elliptical bubbles aligned diagonally along the direction of shear will have a much larger separation distance than those aligned horizontally, though they both may be part of a cluster

structure with an equivalent water chord separation distance. This bias is controlled in experiments (Figueroa-Espinoza and Zenit, 2005), or numerically (Bunner and Tryggvason, 2003), by maintaining a homogenous bubble size distribution. To correct for this bias, and to better accommodate a wide range of bubble diameters, deformations, and orientations, the water chord distance between a primary and neighbor bubble interface is used as the inter-bubble distance. In this fashion a fully 2D analysis is achieved, allowing for characterization of both longitudinal and vertical clustering, or any combination of the two, at multiple locations throughout the jump. Additionally, the experimental assumption that a bubble is intercepted along the primary axis is no longer necessary, as the full bubble profile is available from the volume fraction field.

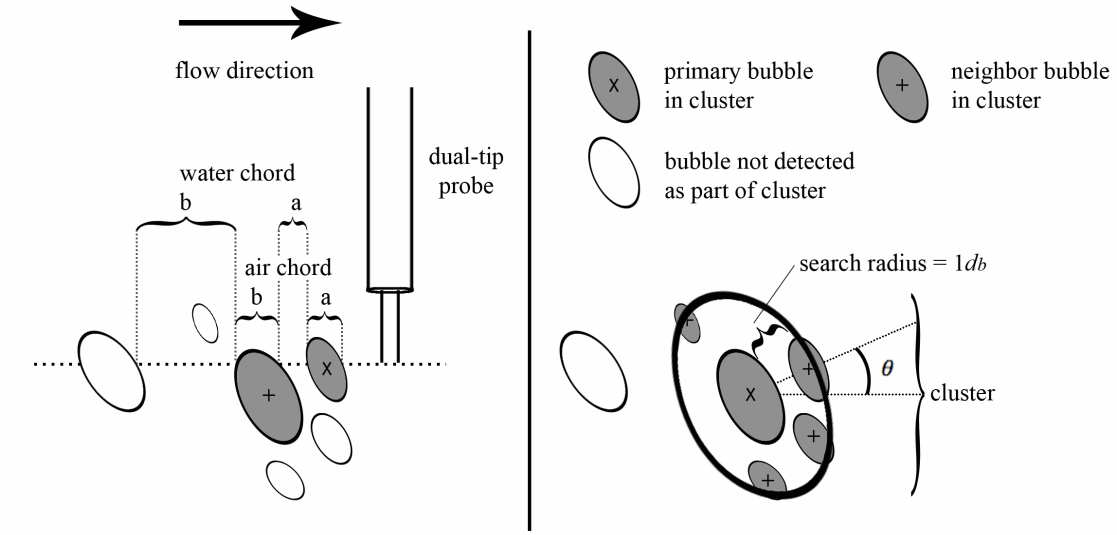

Figure 4.19. Experimental (left) and numerical (right) techniques applied to define a bubble cluster. In experiments, air and water chord lengths are recorded at a single elevation and bubbles are assumed spherical, detected along their diameter. Vertical clusters and vertically offset horizontal clusters are not detected. The numerical technique (right) accounts for all clustered bubbles located within $1d_b$.

The search radius of $1d_b$ is chosen upon consideration of the near-wake region and after a sensitivity analysis. Bubble wake length is dependent on particle Reynolds number (Clift et al., 1978), which requires as input the terminal velocity of a bubble rising in stagnant fluid. When calculated using the terminal rise velocity of bubbles with the size range present in the hydraulic jump, the particle Reynolds number is greater than 600. Wake length is only well defined up to $Re_p = 400$, where wake length plateaus at ~ $1d_b$ (Clift et al., 1978). In the turbulent hydraulic jump bubble wake is not able to develop significantly, though bubbles have a rise velocity capable of lifting them out of the shear layer and wake orientation may strongly depend upon the direction of local shear. As a comparison, deformable bubbles have shown a high probability of clustering near $1d_b$ from the interface (Bunner and Tryggvason, 2003), while bubble clusters in the hydraulic jump have been analyzed using a water chord of length $1d_b$ (Chachereau and Chanson, 2011b). A search radius of $0.5d_b$ and $2d_b$ were analyzed to determine the sensitivity of the cluster results. The location of cluster density was visually similar with no significant differences. Thus a search radius of $1d_b$ was employed for all Fr jumps.

4.5.2. Bubble cluster results

The spatial density of clustered bubble location over time is shown in Figure 4.20 for $Fr = 2.43$, 3.65 and 4.82. It is evident that clustering in the air-water shear layer is predominant. For $Fr = 2.43$, a lack of clusters is observed in the roller and in the lower wall region. As Fr is increased, clusters are found closer to the lower wall, and cluster density in the lower shear layer is increased, but cluster density remains sparse in the roller. The fact that clusters appear near the wall for higher Fr jumps and the interactions between vortices and the lower boundary layer also increase for higher Fr jumps indicates vortices may be responsible for some clustering in the lower shear layer.

For all jumps, cluster density is increased just below the free surface, near the end of the roller region. This peak cluster density corresponds closely with the location where recirculation ceases and the flow is unidirectional downstream, suggesting bubbles are densely clustered due to stagnation in the flow. This high cluster density region becomes

more diffused, spreading both longitudinally and vertically, as *Fr* increases. The average number of bubbles per cluster structure is 2.91, 3, and 2.84 for *Fr* = 2.43, 3.65 and 4.82, respectively. Despite the difference in cluster detection technique, these values are only slightly higher than the average range of 2.3 to 2.7 observed experimentally (Chanson, 2010; Chachereau and Chanson, 2011b). The percentage of bubbles in cluster structures was found to be 42.5% for *Fr* = 2.43, 40% for *Fr* = 3.65, and 31.8% for *Fr* = 4.82, also the range of 20-60% observed experimentally.

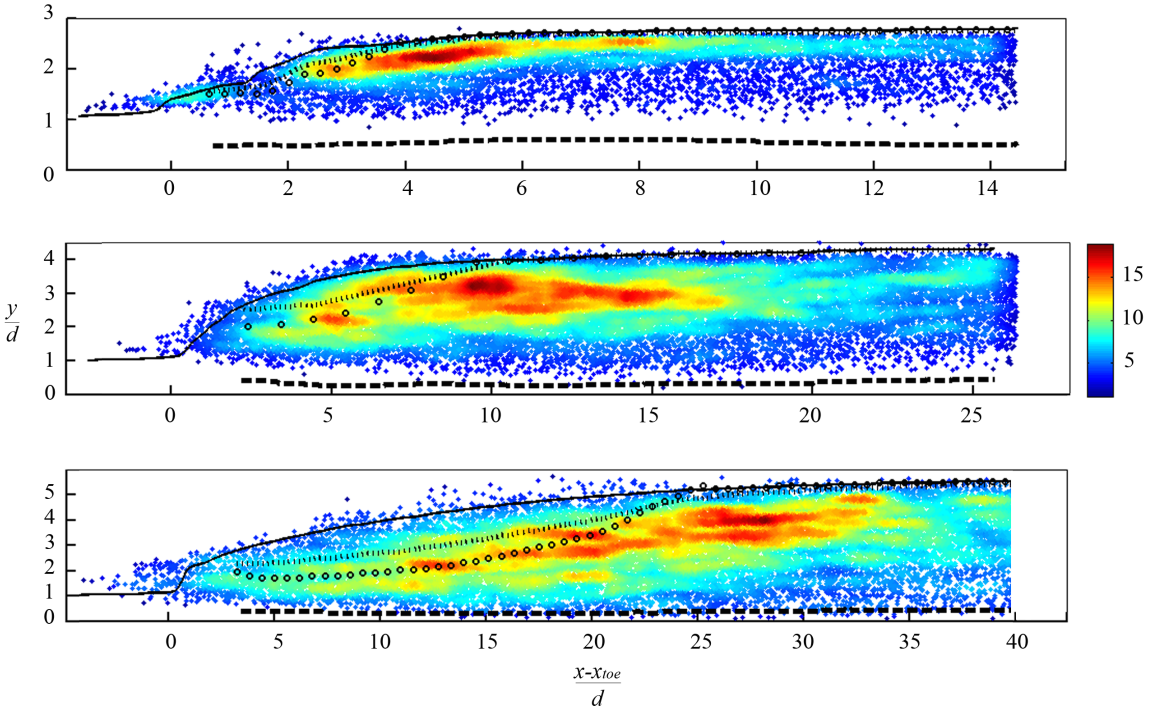

Figure 4.20. Color contour of spatial density of primary clustered bubbles over all time steps for *Fr* = 2.43 (top), *Fr* = 3.65 (middle), and *Fr* = 4.82 (bottom). Density is computed by calculating the number of times a cluster was detected within a prescribed search radius (~0.1*d*). Symbols see Figure 4.5.

Nearly all of the existing literature on bubble clustering in the hydraulic jump presents cluster information at a fixed elevation, where the bubble frequency is at a maximum (Chanson, 2007b; Chanson, 2010; Chacherau and Chanson, 2011b). At this elevation, which tracks more closely with the line of maximum velocity, the number of clusters per second, N_{cs}, peaks near the toe and decreases downstream. Figure 4.20 indicates that cluster statistics obtained at a single elevation are not indicative of the cluster behavior throughout the jump. One set of experimental results exists which provides a vertical profile of cluster statistics at several locations for a jump of $Fr = 6.51$ (Gualtieri and Chanson, 2010). For a qualitative comparison with these results, Figure 4.21 presents a vertical profile of N_{cs} at several longitudinal locations for the $Fr = 4.82$ simulation. The trend of the cluster data is remarkably similar to Gualtieri and Chanson (2010), where a 1D longitudinal clustering criteria was employed. The number of clusters peaks in the lower shear layer near the toe, just above the impingement elevation. Moving downstream, the elevation of maximum number of clusters increases to the upper shear region. This behavior is notably different from higher *Fr* jumps tested in the same experiments, where clustering in the lower shear layer is predominant throughout all longitudinal locations, correlating more closely with the region of high Reynolds stress and turbulence intensity. While cluster statistics obtained at a single elevation for jumps of $Fr > 6$ may represent the overall cluster behavior of the jump, Figure 4.20 provides evidence that cluster structures are spatially inhomogeneous for lower *Fr* jumps, and that the mechanism responsible for clustering in jumps of $Fr < 6$ may be characteristically different that that for jumps of $Fr > 6$.

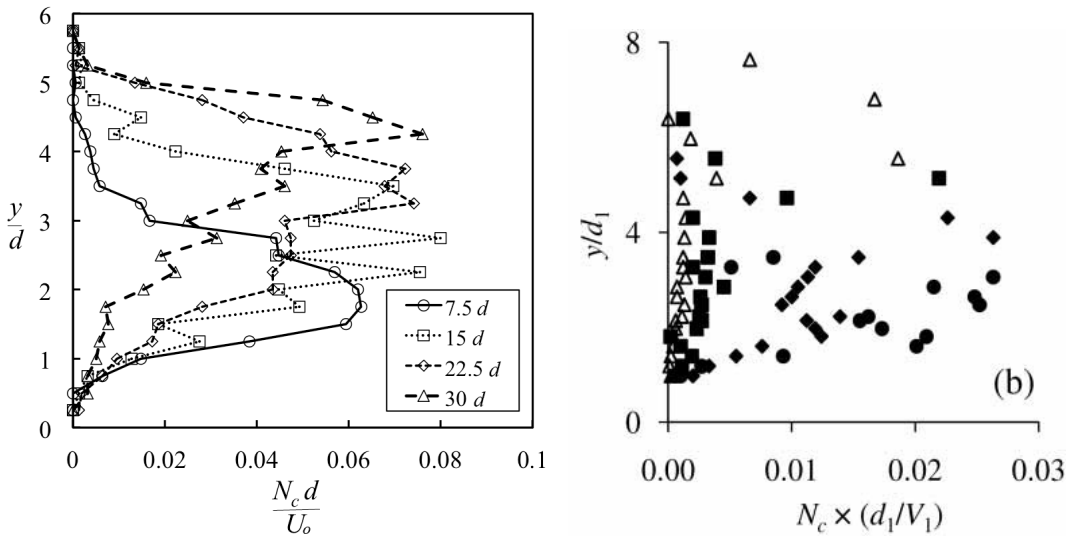

Figure 4.21. Left: vertical profile of the number of clusters per second for the $Fr = 4.82$ simulation at four downstream locations. Right: number of clusters per second for an experimental hydraulic jump of $Fr = 6.51$ (Gualtieri and Chanson, 2010) at $x\text{-}x_{toe} = 4.17d$ (●), $8.33d$ (◆), $12.5d$ (■) and $16.7d$ (△).

4.5.3. Correlation between vorticity and entrained air

Some temporal cross-correlations between free surface elevation and void fraction have shown that highly aerated vortices traveling within the shear layer are responsible for free surface fluctuations (Wang and Chanson, 2013). Further evidence of this phenomenon is shown in Figure 4.22, where spatial cross-correlations between fluctuating total entrained air and both shear layer vorticity (left) and the free surface (right) indicate strong coupling at zero lag. Total entrained air is obtained by integrating the void fraction from the lower wall to the elevation where $\varphi = 0.5$. Both correlations display an oscillating pattern, with similar periodicity as the correlations of free surface and shear layer elevation observed in Sec. 4.4. The results indicate both vorticity and free surface fluctuations are strongly coupled to the underlying air concentrations, and that traveling vortices have the ability to organize air into spatially distinct regions.

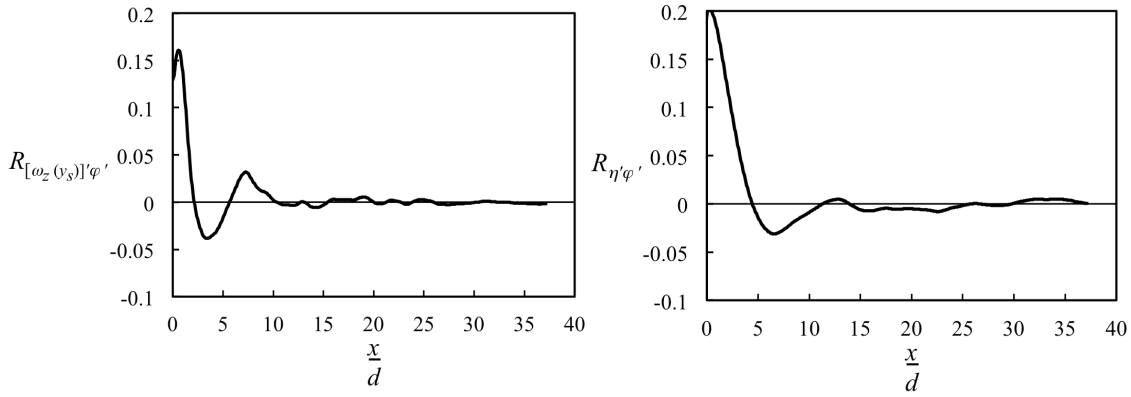

Figure 4.22. Normalized spatial cross-correlation analysis between the fluctuating components of total entrained air φ', shear layer vorticity $\omega_z(y_s')$, and free surface fluctuations, η'.

4.5.4. Bubble breakup

Bubble breakup has been proposed as a possible mechanism leading to the creation of bubble clusters (Chanson, 2010; Chachereau and Chanson, 2011b). Breakup of an air pocket in a turbulent field generally occurs when the local turbulent stresses overwhelm the restoring force of surface tension. A mother bubble will breakup into daughter bubbles with diameter dependent on initial bubble size and the fluid dynamics of the continuous phase (Hinze, 1955; Clift et al., 1978; Lasheras et al., 2002). A representative bubble size based on this formulation is given as (Hinze, 1955)

$$d_m = K_b \left(\frac{\sigma}{\rho}\right)^{3/5} \varepsilon^{-2/5} \tag{4.20}$$

where d_m is the maximum bubble size before breakup, or the bubble size larger than 95% of bubbles in the flow, and K_b is an empirical constant taken to be 1.4. Assuming isotropic turbulence, energy dissipation is related to turbulent velocity fluctuations on a bubble diameter scale. An increasing rate of energy dissipation should result in a smaller maximum bubble size.

When the maximum value of simulated ε at each horizontal location is used to compute d_m from Eq. 4.20, a much smaller bubble diameter is expected at the toe. A comparison with both simulation and experimental bubble diameter shows that larger bubble sizes are present at the toe of the jump (Figure 4.23). Within the jump, the maximum bubble size occurs near the point of entrainment, and experiences breakup in the turbulent shear region. The development of Eq. 4.20 assumes an isotropic turbulence, which is not present throughout most of the roller. The development of vertical structures at the toe with turbulent length scales larger than bubbles contributes to the transport of bubbles downstream, but maximum bubble size after breakup is not easily related to the underlying turbulent flow field.

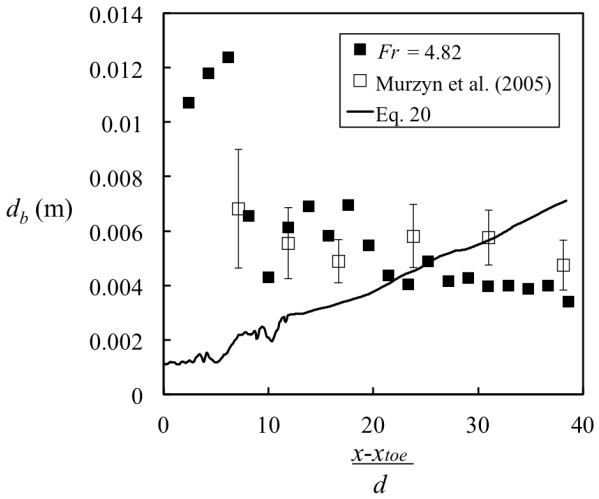

Figure 4.23. Comparison of simulated and experimental bubble diameter with Eq. 4.21.

Martinez-Bazán et al. (1999) showed that breakup also depends on bubble size. Above a critical diameter, the breakup frequency decreases with increasing bubble size. To apply this method to the simulated results, an estimate of bubble breakup is obtained by computing the total flux of all bubbles downstream over time, F_b, as (Martinez- Bazán et al., 1999)

$$F_b = \frac{N_t(x)\ \ \overline{u}_{bx}(x)}{L} \tag{4.21}$$

where $N_t(x)$ is the total number of bubbles in a measurement window of length L, held constant at $2.5d$ for all runs, and $u_{bx}(x)$ is the mean horizontal velocity of all bubbles in the measurement window. Window height is limited by the elevation of minimum positive velocity in order to remove any bubbles that may be recirculated by the roller. Assuming air entrainment at the toe is the primary source of bubbles convected downstream, conservation of mass dictates that bubble breakup is responsible for the increase in total bubble population downstream. The resulting flux of bubbles (Figure 4.24a) exhibits an increase from the toe to a point within the roller, indicating steady breakup in the turbulent shear region. At this point the peak levels off until it reaches the downstream end of the roller region, where a steady descent is observed, indicating detrainment through the free surface.

Breakup by size category for $Fr = 4.82$ (Figure 4.24b) shows that a range of bubble sizes are present at the toe. The initial breakup results in a high proportion of smaller bubbles and fewer large bubbles. Further breakup of the largest bubbles leads to a significant rise in the population of the smallest bubbles. Martinez-Bazán et al. (1999) postulated bubble breakup frequency was strongly dependent on energy dissipation, bubble diameter, and surface tension. In the limit of large bubbles, surface tension becomes less important and the theoretical breakup frequency is approximated as

$$g(\varepsilon,d_b) \approx \varepsilon^{1/3} d_b^{-2/3} \tag{4.22}$$

where $g(\varepsilon, d_b)$ is the breakup frequency. The breakup frequency of large bubbles ($d_b >$ 0.01m) in the simulation can be calculated from Eq. 4.21 as

$$g(\varepsilon,d_b) = -\frac{1}{N_t(x)}\frac{\partial F_b}{\partial x} \tag{4.23}$$

To compare theoretical and simulated breakup frequency, the mean energy dissipation from the first half of the roller ($0d$ – $12.5d$) and the largest bubble class, $d_b >$ 0.01m, are input into Eq. 4.22 and the breakup frequency from the bubble flux is

computed using Eq. 4.23. The comparison (Figure 4.24c) displays a strong correlation, indicating the simulated breakup frequency is dependent on both energy dissipation and bubble size. These breakup results may be correlated with clustering in certain regions of the jump. For example, the maximum bubble flux for each *Fr* jump (Figure 4.24a) coincides roughly with the regions of increased cluster density (Figure 4.20). The breakup of large air pockets at the toe may result in bubbles that tend to travel together in groups, and clustering appears to be more likely in the region where breakup ends.

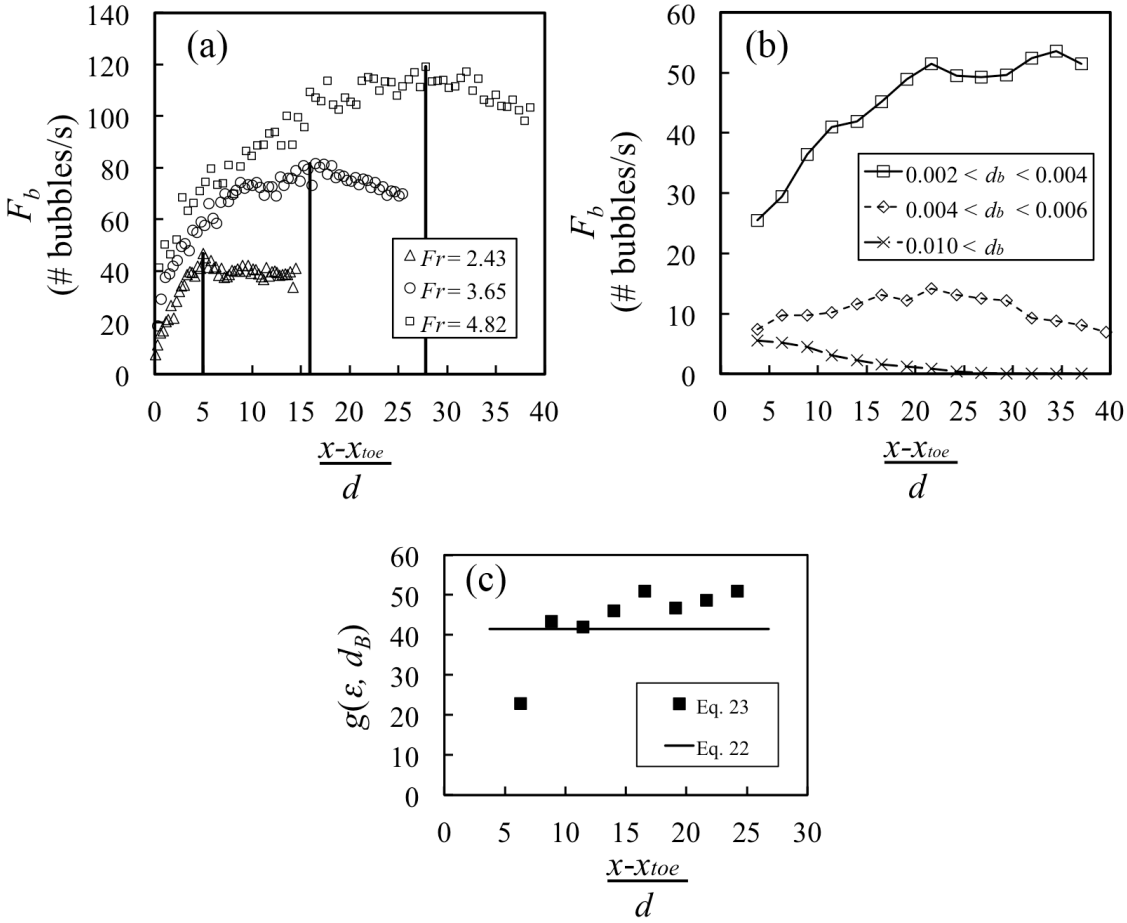

Figure 4.24. (a) Flux of bubbles downstream for all jumps. Solid black line indicates max F_b. (b) Flux of bubbles downstream by bubble size for $Fr = 4.82$. (c) Comparison of breakup frequency in the roller region for $Fr = 4.82$, $d_b > 0.01$m.

Further insight may be gained by analyzing the orientation of clustered bubbles. A bubble in a shear flow will exhibit a deformation angle θ_b, based on diameter and the rate of shear applied (Clift et al., 1978). As shear is increased, the bubble becomes elongated until the major axis is aligned horizontally with the flow, or $\theta_b = 0$ (Rust and Manga, 2002). Immediately after breakup, clustered bubbles would be expected to exhibit the orientation of elongation, or $0 < \theta_b < -\pi/4$. As a measure of cluster orientation, the center of each clustered neighbor bubble is displayed in relation to the primary bubble (x_n-x_p, y_n-y_p) for a range of bubble diameters (Figure 4.25). The corresponding separation angle, θ, is shown in relation to d_{bn}, and the solid line indicates the separation angle PDF. A clear trend in separation angle emerges independent of bubble size, with the peak of the PDF for each bubble group occurring very near $\theta = -0.14$. The peak is also independent of downstream location and elevation. A similar trend is observed for $Fr = 2.43$ and $Fr = 3.65$, which exhibit dominant separation angles of $\theta = -0.27$ and $\theta = -0.21$, respectively. As Fr is increased, the maximum probable separation angle is decreased, corresponding with an increase in shear. The separation angle is established initially near the toe in a region of high shear and maintained downstream, where shear is reduced and there is less migration of bubbles. Bubble clustering thus appears to be the remnant of bubble breakup, given the dominant separation angle is independent of downstream location and aligns closely with the direction of initial shear.

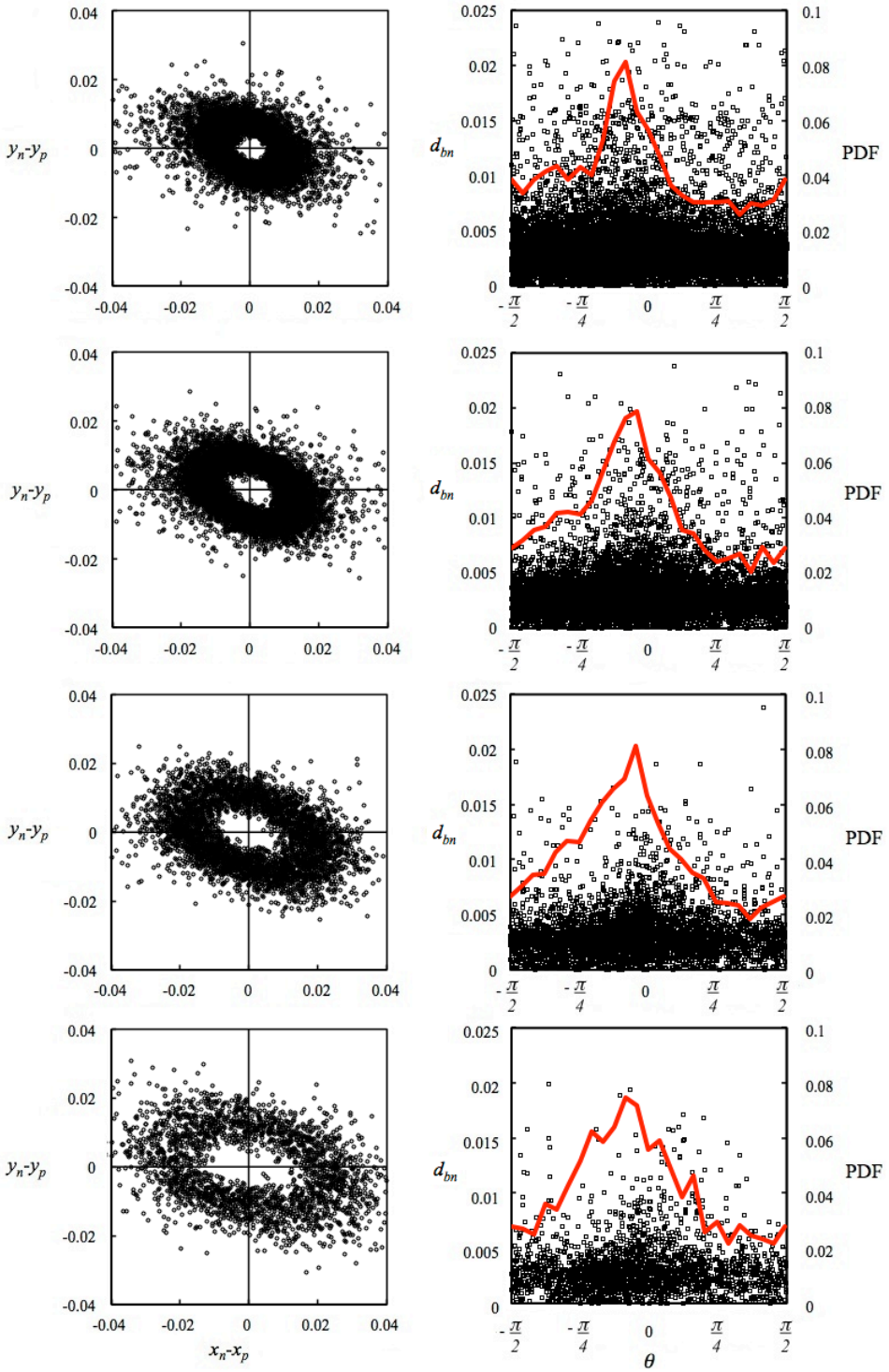

Figure 4.25. Relative location of clustered bubble (○) to primary bubble centered at (0,0) for Fr = 4.82 and (a) $0.002 < d_b < 0.004$; (b) $0.004 < d_b < 0.006$; (c) $0.006 < d_b < 0.008$; and (d) $0.008 < d_b < 0.01$ (left). Separation angle θ for each neighbor bubble (right). Solid red line indicates separation angle PDF.

4.6. Conclusions

In this work, numerical simulations are carried out to analyze the air-water characteristics of the hydraulic jump. The simulations capture air entrainment at the toe, and are used to analyze bubble dynamics and the instantaneous behavior of the shear layer. Shear layer instabilities produce vortices that periodically interact with the free surface. Over time the shear layer instability develops closer to the toe, eventually leading to a violent splash up and downstream fluctuation of the toe as vortices reach the free surface. The most energetic free surface fluctuations occur after a roll-up of elliptical vortices at the toe. A strong positive correlation is seen between the motion of the shear layer and the free surface, indicating the presence of vortices creates a rise in the free surface that persists throughout the jump. Vortices also interact with the lower wall boundary layer, which results in an ejection of non-bubbly fluid into the shear layer, creating distinct regions that lack bubbles. A cross-correlation analysis shows that traveling vortices can organize bubbles spatially, and higher free surface fluctuations are representative of greater underlying entrained air.

Bubble breakup is captured in the simulations, and breakup frequency is related to energy dissipation and bubble size. The breakup of an initial air pocket results in a significant population of small bubbles that display a characteristic cluster structure based on Froude number. Bubble cluster density maps indicate the roller region lacks clusters while the shear layer contains a significant density of clusters, particularly near the end of the roller region, where bubble breakup has ceased. A high cluster density is seen directly below the roller depth, though this region shifts lower into the shear layer and diffuses as Froude number is increased. Consequently, the mechanisms responsible for bubble clustering appear to be Froude number dependent. Clusters exhibit a separation angle independent of downstream location or elevation. The angle aligns with the direction of shear, indicating the initial breakup at the toe of a large bubble into smaller bubbles may be preserved to some extent downstream in the form of clusters that congregate near a stagnation point at the end of the roller.

5. Summary and future work

5.1. Summary

The hydraulic jump is a highly turbulent fluid phenomenon rich in flow physics. When the hydraulic jump is used to improve aeration at a hydraulic structure, the physical mechanisms controlling air entrainment must be modeled correctly in order to predict gas transfer accurately. In this dissertation, the air entraining characteristics of the hydraulic jump have been investigated in detail using analytical and numerical techniques, generating new understandings in the fields of gas transfer and multiphase flow modeling.

An important finding of this work is the significance of bubble physics in the development of gas transfer predictive equations at hydraulic jumps. Reduced order predictive models that do not incorporate mass transfer across a bubble interface will not capture the bulk flux of oxygen into the flow. The generation of bubbles is dependent on the strength of the hydraulic jump, which, at a prototype structure, is correlated with the depth of the jump in the stilling basin and, to a lesser extent, the difference between the static headwater and tailwater depths. When the jump is submerged and the hydraulic jump depth is large, bubble generation is minimal and transfer efficiency is small. When the jump becomes unsubmerged, the depth of the jump begins to decline while bubble generation and transfer efficiency increase. When the relevant dimensionless relationships are scaled using the depth of the hydraulic jump as a characteristic length scale, transfer efficiency predictions are improved.

Advances in numerical modeling and computational power allow for the simulation and analysis of a laboratory scale air entraining hydraulic jump. The initial entrainment of air at the toe, the shearing of air pockets to small bubbles, and the transport of bubbles in the turbulent shear layer are all captured in numerical simulations

without the use of an air entrainment subgrid model. Major findings are summarized as follows:

- An unsteady RANS formulation of the Navier-Stokes equations coupled with a Volume of Fluid treatment of the free surface and a realizable k-ε turbulence closure model can represent an air entraining laboratory scale hydraulic jump.

- The quantity of air entrained by a hydraulic jump in a 2D simulation is within 10% of experimental values when the largest bubbles in the flow are modeled with at least eight computational cells. At the same minimum grid size, computational time for the 2D simulation is 3 orders of magnitude less than a comparable 3D simulation, while the relative error in total entrained air is of the same order of magnitude.

- A 3D simulation produces improvement in void fraction and bubble size due to the resolution of 3D turbulent structures, which contribute to bubble transport and breakup.

- The motion of the toe is related to vortex structure of the hydraulic jump. When the toe is moving upstream, vortices tend to convect without interacting with the free surface and without merging. Downstream movement of the toe occurs when vortices merge and interact with the free surface. The roller becomes supply limited at the impingement point with the upstream jet when recirculation is interrupted.

- Counter-rotating vortex pairs are formed between spanwise vortices and contribute to breakup and transport of bubbles to the lower shear layer. These pairs also interact with the free surface and are responsible for splashing and ejections of fluid from the roller.

- Vertical motion of the shear layer is positively correlated with the vertical motion of the free surface, indicating vortices are responsible for surface perturbations throughout the jump. These vortices tend to contain a relatively large amount of air in relation to the mean flow.

- An increase in small bubbles and a decrease in large bubbles moving downstream from the toe shows breakup is captured in the simulations. Bubble breakup frequency is related to energy dissipation and bubble size.

- Bubble clusters are observed in spatially distinct regions of the jump. Bubble cluster density appears to be a function of Froude number. A characteristic separation angle is observed in all cluster structures independent of bubble size and location. The angle is related to the angle of maximum shear, and we suggest that clustering is the remnant of bubble breakup.

From a practical engineering design standpoint, additional steps are required to extend these simulations to prototype structures. Because the smallest scale bubbles are not resolved, bubble frequency is underrepresented. The impact of these smaller bubbles on the overall flow field is not thought to be significant, though their contribution to mass transfer may be important and would need to be quantified. Scale effects are observed in terms of bubble count rate and void fraction when Reynolds number is increased but Froude number similitude is maintained (Chanson, 2007a), and thus a 1:1 scale simulation of a prototype spillway is required to capture all relevant air-water characteristics. The typical prototype scale is much larger than experimental scale, and prohibitively large computational times would be required to model air entrainment in a stilling basin in 3D while maintaining the appropriate bubble diameter to grid ratio. However, 2D simulations may be implemented with much less computational effort at a comparable error in total entrained air. These simulations may be used to capture the

average void fraction in the stilling basin, reducing the uncertainty in an important inlet boundary condition.

5.2. Future work

5.2.1. Coupled experimental and numerical analysis

The initial entrainment of air at the toe may be investigated through a coupled experimental and numerical analysis. A recent work characterized air entrainment in plunging flows by tracking the entrainment frequency of large air pockets near the impingement of an angled jet into a quiescent pool (Deshpande et al., 2012a; Deshpande and Trujillo, 2013). This work coupled an experimental particle tracking velocimetry (PTV) approach with a numerical investigation using *interFoam* to show that total ingested air volume is distributed more noticeably in larger cavity sizes as impingement angle is decreased. The initial cavity creation was related to a nearly horizontal jet repeatedly impacting a liquid pool. The hydraulic jump and shallow plunging jet show a degree of similarity in that the initial entrainment at the impingement point is the source of air in the near field, and semi-periodic interactions between recirculating flow and the impinging jet control the void fraction distribution downstream. A similarity is also noted between the plunging jet and the hydraulic jump as it is described in Chapter 2. As the difference between the upstream jet depth and tailwater depth decreased, an increase in air entrainment was observed, hinting that larger cavity sizes may be entrained as the jump becomes increasingly unsubmerged. These similarities are sufficient to warrant further analysis.

Strategic placement of sensors and high-speed video cameras could capture the passing frequency of the initial pocket of entrained air in the hydraulic jump using PTV in an experimental flume with backlighting for bubble visualization. Though significant challenges persist in capturing accurate flow measurements in this highly turbulent, bubbly region, a recent experiment successfully used bubbles as tracer particles within a

hydraulic jump (Lin et al., 2012). Once validated, a numerical model could provide an estimate of the total volume of entrained air in each pocket. The model could be modified to test the relationship between air entrainment and inflow parameters. Both the volume of the pocket and the passing frequency could be related to the incoming Froude number, and possibly the Reynolds number. If a better understanding is gained as to the mechanisms governing the initial entrainment, extension of a theoretical air entrainment model to Reynolds numbers typical of prototype structures may be possible. These simulations could then provide practical engineering design and optimization guidance at low-head structures.

Further downstream, when the initial pocket has experienced significant breakup into smaller bubbles, the total quantity of entrained air could be related to the initial entrainment at the toe. Estimates of bubble breakup frequency could be made by comparing downstream size distributions to initial pocket size, and an estimate of interfacial area could be made based on downstream bubble size distributions. Careful analysis of sampling rates must be made, and a balance struck between experimental accuracy and computational expense. A difference in bubble frequency between experiments and simulations is expected when the sampling rate is under represented in the numerical model. However, if this difference is shown to be due mainly to small bubbles with no significant impact on the flow field, interfacial area from experiments may be well represented in simulations.

5.2.2. Mass transport in OpenFOAM

A second area of future study is the coupling of mass transport equations to the existing governing equations for multiphase flow in *interFoam*. The OpenFOAM library contains a robust collection of solvers and discretization schemes that are easily modified to solve for additional flow parameters. Considering the simulations outlined in this work, the addition of a passive scalar transport equation could account for mass flux from the gas phase to the liquid phase.

The governing equation for scalar mass transport is given as

$$\frac{\partial C}{\partial t}+\nabla(\boldsymbol{u}C) = \nabla(D\nabla C)+S\,, \tag{5.1}$$

where C is a scalar concentration, D is the molecular diffusion coefficient, and S is a source/sink term, which is equal to $k_La(C_S\text{-}C)$ for mass flux across a bubble interface. Coupling this equation to an unsteady RANS model requires the appropriate Reynolds averaging, resulting in

$$\frac{\partial \overline{c}}{\partial t}+\nabla\cdot(\overline{\boldsymbol{u}}\overline{c}) =\nabla\cdot j + S = \nabla\cdot(D\nabla\overline{c} - \overline{\boldsymbol{u}'c'}) + k_La(C_S-\overline{c}), \tag{5.2}$$

where the overbar indicates an average quantity, $\overline{\boldsymbol{u}'c'}$ is the turbulent mass transport, and j is the total concentration flux. In the bulk flow, the magnitude of turbulent fluctuations is much larger than molecular diffusion, and diffusive mass flux is considered insignificant. Very near the interface, turbulent velocity fluctuations tend towards zero and diffusive mass flux is the dominant transfer mechanism (Gulliver, 2007).

An open research question is the choice of an appropriate closure technique for the total concentration flux. Accurate numerical modeling of gas transfer from air to liquid requires adequate resolution of the concentration boundary layer in order to capture the transition from turbulent to molecular mass transport. However, the concentration boundary layer is several orders of magnitude smaller than the momentum boundary layer. With current computational abilities, full resolution of mass transfer across a bubble interface is only possible for a single bubble in a narrow domain (Marschall et al., 2012), meaning mass transfer across bubbles generated within the hydraulic jump would require a subgrid model.

One possible approach is to apply a limiter that modifies the concentration flux and source term in cells that contain an interface, similar to the MULES approach used to discretize the volume fraction transport equation in OpenFOAM (Rusche, 2002). The governing equation would be written as

(5.3)

$$\frac{\partial \overline{c}}{\partial t} + \nabla \cdot (\overline{\boldsymbol{u}}\overline{c}) = \lambda(\nabla \cdot j) + (1-\lambda)S\,,$$

where λ is a limiter, and a function of γ. In the bulk flow $\lambda = 1$, ensuring concentration transport is governed by turbulent and diffusive fluxes, in addition to the convective flux. At an interface $\lambda = 0$, the equivalent application of a subgrid model for interfacial mass flux. Mass transfer is attributed to the source term $S = k_L a(C_S - C)$. Both the interfacial area and liquid film coefficient could be calculated from the γ field and fluid variables.

This method would be highly sensitive to the parameters chosen for λ and k_L, and would require extensive calibration with experimental scale hydraulic jumps at multiple Froude numbers. The source term would need calibration to differentiate mass transfer across the upper free surface interface from mass transfer across an entrained bubble interface. Additionally, discretization of the convective mass transport term would need to be identical to the discretization of the convective volume fraction transport term (Eq. 3.2) to ensure the concentration interface tracks with the air-water interface.

Ideally, the most reliable estimate of mass transfer would account for the sum of the concentration flux across all bubbles within the flow. Though subgrid models are still required to represent the concentration boundary layer, numerical simulations that predict air entrainment and bubble size distributions provide a solid foundation for future work.

References

Abbaspour, A., Farsadizadeh, D., Dalir, A.H., Sadraddini, A.A., 2009. Numerical study of hydraulic jumps on corrugated beds using turbulence models. Turkish J. Eng. Env. Sci. 33, 61–72.

Apted, R.W., Novak, P., 1973. Oxygen uptake at weirs. Proc. 15th *IAHR Congress*, Vol. 2, B23, Istanbul, Turkey, 177-186.

Army Corps of Engineers, n.d. 'Tainter gate'. Management Measures Digital Library. Web. 3 Sept. 2014.

Avery, S.T., Novak, P., 1978. Oxygen transfer at hydraulic structures. J. Hydraulics Div., ASCE, 104(11), 1521–1540.

Azbel, D. (1981). Two phase flows in chemical engineering. Cambridge University Press, London.

Babb, A.F., Aus, H.C., 1981. Measurement of air in flowing water. J. Hydraulics Div. 107, 1615–1630.

Balachandar, S., Eaton, J.K., 2010. Turbulent dispersed multiphase flow. Ann. Review Fluid Mech., 42, 111-133.

Berberović, E., Van Hinsberg, N.P., Jakirlić, S., Roisman, I.V., Tropea, C., 2009. Drop impact onto a liquid layer of finite thickness: Dynamics of the cavity evolution. Phys. Rev. E 79, 036306.

Bernal, L., Roshko, A., 1986. Streamwise vortex structure in plane mixing layers. J. Fluid Mech. 170, 499–525.

Boyer, C., Duquenne, A-M., Wild, G., 2002. Measuring techniques in gas–liquid and gas–liquid–solid reactors. Chem. Eng. Sci. 57(16), 3185–3215.

Brackbill, J., Kothe, D.B., Zemach, C., 1992. A continuum method for modeling surface tension. J. Comput. Phys. 100, 335–354.

Brown, G.L., Roshko, A., 1974. On density effects and large structure in turbulent mixing layers. J. Fluid Mech. 64(4), 775–816.

Brücker, C., 1999. Structure and dynamics of the wake of bubbles and its relevance for bubble interaction. Phys. Fluids. 11(7), 1781-1796.

Bunner, B., Tryggvason, G., 2003. Effect of bubble deformation on the properties of bubbly flows. J. Fluid Mech., 495, 77-118.

Carvalho, R.F., Lemos, C.M., Ramos, C.M., 2008. Numerical computation of the flow in hydraulic jump stilling basins. J. Hydraulic Res. 46(6), 739–752.

Cerretelli, C., Williamson, C., 2003. The physical mechanism for vortex merging. J. Fluid Mech. 475, 41–77.

Chachereau, Y., Chanson, H., 2011a. Free-surface fluctuations and turbulence in hydraulic jumps. Exp. Thermal and Fluid Science, 35(6), 896-909.

Chachereau, Y., Chanson, H., 2011b. Bubbly flow measurements in hydraulic jumps with small inflow Froude numbers. Int. J. Multiphase Flow 37, 555–564.

Chanson, H., Brattberg, T., 2000. Experimental study of the air–water shear flow in a hydraulic jump. Int. J. Multiphase Flow 26(4), 583–607.

Chanson, H., Gualtieri, C., 2008. Similitude and scale effects of air entrainment in hydraulic jumps. J. Hydraulic Res. 46(1), 35–44.

Chanson, H., 1995. Air-water gas transfer at hydraulic jump with partially developed inflow. Water Res., 29(10), 2247-2254.

Chanson, H., 1996. Air bubble entrainment in free surface turbulent flows. Academic Press.

Chanson, H., 2007a. Air bubble entrainment in hydraulic jumps: Physical modeling and scale effects. Proc. 32nd IAHR Congress, Venice, Italy.

Chanson, H., 2007b. Bubbly flow structure in hydraulic jump. European J. Mechanics-B/Fluids 26(3), 367–384.

Chanson, H., 2007c. Dynamic similarity and scale effects affecting air bubble entrainment in hydraulic jumps. 6th Int. Conf. Multiphase Flow, S7_Mon_B_3, Leipzig, Germany.

Chanson, H., 2010. Convective transport of air bubbles in strong hydraulic jumps. Int. J. Multiphase Flow 36(10), 798-814.

Chanson, H., 2013. Hydraulics of aerated flows: qui pro quo? J. Hydraulic Res. 51(3), 223-243.

Cheng, X., Luo, L., Zhao, W., 2004. Study of aeration in the water flow over stepped spillway, in: Proceedings of the World Water Congress.

Cheng, X., Chen, X., 2011. Applying Improved Eulerian Model for Simulation of Air-Water Flow in a Hydraulic Jump. Proc. 2011 World Environmental and Water Resources Congress, Palm Springs, California.

Cheng, X., Chen, X., 2013. Numerical Simulation of Dissolved Oxygen Concentration in Water Flow over Stepped Spillways. Water Environment Res. 85, 434–446.

Chippada, S., Ramaswamy, B., Wheeler, M.F., 1994. Numerical simulation of hydraulic jump. Int. J. Numer. Meth. Eng. 37, 1381-1397.

Clemmens, A.J., Strelkoff, T.S., Replogle, J.A., 2003. Calibration of submerged radial gates. J. Hydraulic Eng., 129(9), 680-687.

Clift, R., Grace, J.R., Weber, M.E., 1978. Bubbles, drops, and particles. Courier Dover Publications.

Dabiri, D., Gharib, M., 1997. Experimental investigation of the vorticity generation within a spilling water wave. J. Fluid Mech. 330, 113–139.

Deshpande, S.S., Trujillo, M.F., Wu, X., Chahine, G., 2012a. Computational and experimental characterization of a liquid jet plunging into a quiescent pool at shallow inclination. Int. J. Heat and Fluid Flow, 34, 1-14.

Deshpande, S.S., Anumolu, L., Trujillo, M.F., 2012b. Evaluating the performance of the two-phase flow solver interFoam. Computational Science & Discovery 5, 014016.

Deshpande, S.S., Trujillo, M.F., 2013. Distinguishing features of shallow angle plunging jets. Phys. Fluids 25, 082103.

EPRI (Electric Power Research Institute), 1990. Assessment and guide to meeting dissolved oxygen water quality standards for hydroelectric plant discharges. EPRI GS-7001, Research Project 2694-8, Palo Alto, CA.

Figueroa-Espinoza, B., Zenit, R., 2005. Clustering in high Re monodispersed bubbly flows. Phys. Fluids, 17, 091701

Foree, E.G., 1976. Reaeration and velocity prediction for small streams. J. Env. Eng. Div., ASCE, 102(5), 937-952.

Gameson, A.L.H., 1957. Weirs and aeration of rivers. J. Inst. Wat. Eng., 11(5), 477-490.

Geldert, D., Gulliver, J., Wilhelms, S., 1998. Modeling dissolved gas supersaturation below spillway plunge pools. J. Hydraulic Eng., 124(5), 513-521.

Gonzalez, A., Bombardelli, F., 2005. Two-phase-flow theoretical and numerical models for hydraulic jumps, including air entrainment. Proc. 31st IAHR Congress, Seoul, Korea.

Gualtieri and Chanson, 2010. Effect of Froude number on bubble clustering in a hydraulic jump. J. Hydraulic Res., 48(4), 504-508.

Gulliver, J.S., Rindels, A.J., 1993. Measurement of air-water oxygen transfer at hydraulic structures. J. Hydraulic Eng. 119(3), 327-349.

Gulliver, J.S., Hibbs, D.E., McDonald, J.P., 1997. Measurement of effective saturation concentration for gas transfer. J. Hydraulic Eng., 123(2), 86-97.

Gulliver, J.S., Thene, J.R., Rindels, A.J., 1990. Indexing gas transfer in self-aerated flows. J. Env. Eng., 116(3), 503-523.

Gulliver, J.S., Wilhelms, S.C., and Parkhill, K.L., 1998. Predictive capabilities in oxygen transfer at hydraulic structures. J. Hydraulic Eng., 124(7), 664-671.

Gulliver, J.S., 2007. Introduction to chemical transport in the environment. Cambridge University Press, New York.

Hadjerioua, B., Wei, Y., Kao, S.-C., 2012. An assessment of energy potential at non-powered dams in the United States. ED 19 07 04 2, Oak Ridge National Laboratory, Oak Ridge, TN.

Hager, W.H., 1992. Energy dissipators and hydraulic jump. Springer.

Hettiarachchi, S.L., Gulliver, J.S., Hibbs, D.E., Howe, J., Miller, K.F., Kincaid, G.P., 1998. Gas transfer measurements at hydraulic structures on the Ohio River. Project Report No. 414, St. Anthony Falls Laboratory, Minneapolis, MN.

Hibbs, D.E., Gulliver, J.S., 1997. Prediction of effective saturation concentration at spillway plunge pools. J. Hydraulic Eng., 123(11), 940-949.

Hinze, J.O., 1955. Fundamentals of the hydrodynamic mechanism of splitting in dispersion processes. AIChE Journal, 1(3), 289-295.

Ho, C.-M., Huang, L.-S., 1982. Subharmonics and vortex merging in mixing layers. J. Fluid Mech. 119, 443–473.

Holler, A.G., 1971. The mechanism describing oxygen transfer from the atmosphere to discharge through hydraulic structures. Proc. 14th IAHR Congress, Vol. 1, A45, Paris, France, 373-382.

Hornung, H.G., Willert, C., Turner, S., 1995. The flow field downstream of a hydraulic jump. J. Fluid Mech. 287, 299–316.

Hoyt, J.W., Sellin, R., 1989. Hydraulic jump as "mixing layer". J. Hydraulic Eng. 115(12), 1607–1614.

Hussain, A., 1986. Coherent structures and turbulence. J.Fluid Mech. 173, 303-356.

Iafrati, A., 2009. Numerical study of the effects of the breaking intensity on wave breaking flows. J. Fluid Mech. 622, 371–411.

Ivanchenko, A.I. (1936). Discussion of 'The hydraulic jump in terms of dynamic similarity'. Trans. ASCE 101, 668-669.

Kim, S.-E., Choudhury, D., Patel, B., 1999. Computations of complex turbulent flows using the commercial code FLUENT. Modeling complex turbulent flows, Springer Netherlands, 259-276.

Krishna, R., van Baten, J.M., 1999. Rise characteristics of gas bubbles in a 2D rectangular column: VOF simulations vs experiments. Int. Comm. in Heat and Mass Transfer 26(7), 965–974.

Kucukali, S., Cokgor, S., 2009. Energy concept for predicting hydraulic jump aeration efficiency. J. Environmental Eng., 135(2), 105-107.

Lasheras, J.C., Eastwood, C., Martınez-Bazán, C., Montanes, J., 2002. A review of statistical models for the break-up of an immiscible fluid immersed into a fully developed turbulent flow. Int. J. Multiphase Flow, 28, 247-278.

Lennon, J.M., Hill, D.F., 2006. Particle image velocity measurements of undular and hydraulic jumps. J. Hydraulic Eng.132, 1283–1294.

Liao, Y., Lucas, D., 2009. A literature review of theoretical models for drop and bubble breakup in turbulent dispersions. Chem. Eng. Sci., 64, 3389-3406.

Library of Congress, n.d. 'How a river can light your home'. Web. 3 Sept. 2014.

Lin, J.C., Rockwell, D., 1995. Evolution of a quasi-steady breaking wave. J. Fluid Mech. 302, 29–44.

Lin, C., Hsieh, S., Lin, I., Chang, K., Raikar, R., 2012. Flow property and self similarity in steady hydraulic jumps. Exp. Fluids 53, 1591-1616.

Liu, M., Rajaratnam, N., Zhu, D.Z., 2004. Turbulence structure of hydraulic jumps of low Froude numbers. J. Hydraulic Eng. 130(6), 511–520.

Liu, Q., Drewes, U., 1994. Turbulence characteristics in free and forced hydraulic jumps. J. Hydraulic Res. 32(6), 877-898.

Long, D., Rajaratnam, N., Steffler, P.M., Smy, P.R., 1991. Structure of flow in hydraulic jumps. J. Hydraulic Res. 29(2), 207–218.

Lörstad, D., Fuchs, L., 2004. High-order surface tension VOF-model for 3D bubble flows with high density ratio. J. Comput. Phys. 200, 153–176.

Lubin, P., Vincent, S., Abadie, S., Caltagirone, J.-P., 2006. Three-dimensional large eddy simulation of air entrainment under plunging breaking waves. Coastal Engineering 53, 631–655.

Lubin, P., Glockner, S., Chanson, H., 2009. Numerical simulation of air entrainment and turbulence in a hydraulic jump. Presented at the Colloque SHF Modèles Physiques Hydrauliques: Outils Indispensables du XXIe Siècle, Société Hydrotechnique de France, 109–114.

Ma, J., Oberai, A., Lahey, Jr, R., Drew, D., 2011. Modeling air entrainment and transport in a hydraulic jump using two-fluid RANS and DES turbulence models. Heat Mass Transfer 47, 911-919.

Marschall, H., Hinterberger, K., Schüler, C., Habla, F., Hinrichsenn, O., 2012. Numerical simulation of species transfer across fluid interfaces in free-surface flows using OpenFOAM. Chem. Eng. Sci., 78, 111-127.

Martinez-Bazan, C., Montanes, J., Lasheras, J.C., 1999. On the breakup of an air bubble injected into a fully developed turbulent flow. Part 1. Breakup frequency. J. Fluid Mechanics, 401, 157-182.

Michalke, A., 1965. On spatially growing disturbances in an inviscid shear layer. J. Fluid Mech 23, 521–544.

Misra, S.K., Kirby, J.T., Brocchini, M., 2005. The turbulent dynamics of quasi-steady spilling breakers: theory and experiments. Research Report CACR-05-08, University of Delaware.

Misra, S., Kirby, J., Brocchini, M., Veron, F., Thomas, M., Kambhamettu, C., 2008. The mean and turbulent flow structure of a weak hydraulic jump. Phys. Fluids 20(3), 035106.

Mossa, M., Tolve, U., 1998. Flow visualization in bubbly two-phase hydraulic jump. J. Fluids Eng. 120, 160–165.

Murzyn, F., Mouaze, D., Chaplin, J.R., 2005. Optical fibre probe measurements of bubbly flow in hydraulic jumps. Int. J. Multiphase Flow 31, 141-154.

Murzyn, F., Chanson, H., 2007. Free surface, bubbly flow and turbulence measurement in hydraulic jumps. Research Report No. CH63/07, University of Queensland, Australia.

Murzyn, F., Chanson, H., 2008. Experimental assessment of scale effects affecting two-phase flow properties in hydraulic jumps. Exp. in Fluids, 45, 513-521.

Murzyn, F., Chanson, H., 2009. Free-surface fluctuations in hydraulic jumps: Experimental observations. Exp. Thermal and Fluid Science 33, 1055–1064.

Murzyn, F., 2013. Personal communication. Void fraction measurement request.

Noymer, P., 2000. The use of single-point measurements to characterize dynamic behavior in sprays. Exp. Fluids, 29, 228-237.

OpenFOAM User Guide, 2012. http://www.openfoam.org/docs/

Orlins, J.J., Gulliver, J.S., 2000. Dissolved gas supersaturation downstream of a spillway II: Computational model. J. Hydraulic Res. 38(2), 151–159.

Peregrine, D.H., Svendsen, I.A., 1978. Spilling breakers, bores, and hydraulic jumps. Coastal Engineering Proceedings 1, 540-550.

Peterson, M., Cada, G., Sale, M., Eddlemon, G., 2003. Regulatory approaches for addressing dissolved oxygen concerns at hydropower facilities. DOE/ID-11071, U.S. Department of Energy, Oak Ridge National Laboratory, Oak Ridge, TN.

Politano, M., Carrica, P., Turan, C., Weber, L., 2007. A multidimensional two-phase flow model for the total dissolved gas downstream of spillways. J. Hydraulic Res. 45, 165–177.

Politano, M., Carrica, P., Weber, L., 2009. A multiphase model for the hydrodynamics and total dissolved gas in tailraces. Int. J. Multiphase Flow, 35, 1036-1050.

Politano, M., Amado, S., Bickford, S., Murauskas, J., Hay, D., 2012. Evaluation of operational strategies to minimize gas supersaturation downstream of a dam. Computers and Fluids, 68, 168-185.

Preul, H.C., Holler, A.G., 1969. Reaeration through low dams in the Ohio River. Proc. Industrial Waste Conf., Purdue University, South Bend, Indiana, 1249-1270.

Progress Energy, 2005. Intensive temperature and dissolved oxygen study of the Pee Dee River below the Tillery and Blewett Falls hydroelectric plants, Water Resources Group, Issues No. 7 and 8.

Qian, Z., Hu, X., Huai, W., Amador, A., 2009. Numerical simulation and analysis of water flow over stepped spillways. Sci. China Ser. E-Technol. Sci. 52, 1958–1965.

Railsback, S.F., G.F. Cada, C.H. Petrich, M.J. Sale, J.A. Shaakir-Ali, J.A. Watts, and J.W. Webb, 1991. Environmental impacts of increased hydroelectric development at existing dams. ORNL/TM-11673, Oak Ridge National Laboratory, Oak Ridge, TN. 46 p.

Rajaratnam, N., 1962. An experimental study of air entrainment characteristics of the hydraulic jump. J. Inst. Eng. India 42(7), 247-273.

Rajaratnam, N., 1965. The hydraulic jump as a wall jet. J. Hydraulics Div. 91(5), 107–132.

Rajaratnam, N., 1967. Hydraulic jumps. In advances in Hydroscience, Ed. V.T. Chow, Academic Press, New York, USA, Vol. 4, 197-280.

Resch, F.J., Leutheusser, H.J., 1972. Reynolds stress measurements in hydraulic jumps. J. Hydraulic Res. 10(4), 409–430.

Rindels, A.J., Gulliver, J.S., 1991. Oxygen transfer at spillways. *Air water mass transfer,* Proc. 2nd Int. Symposium on Gas Transfer at Water Surfaces, Minneapolis, 524-533, S. Wilhelms and J. Gulliver, eds. New York, New York.

Resch, F.J., Leutheusser, H.J., Alemu, S., 1974. Bubbly two-phase flow in hydraulic jump. J. Hydraulics Div. 100 (1), 137-149.

Rodríguez-Rodríguez, J., Marugán-Cruz, C., Aliseda, A., Lasheras, J.C., 2011. Dynamics of large turbulent structures in a steady breaker. Exp. Thermal and Fluid Science 35, 301–310.

Rusche, H. 2002. Computational fluid dynamics of dispersed two-phase flows at high phase fractions. Ph.D. Thesis, Imperial College of Science, Technology and Medicine, London.

Rust, A., Manga, M., 2002. Bubble shapes and orientations in low Re simple shear flow. J. Colloid and Interface Science, 249, 476-480.

Sale, M.J., G.F. Cada, L.H. Chang, S.W. Christensen, S F. Railsback, J.E. Francfort, B.N. Rinehart, and G.L. Sommers, 1991. Environmental mitigation at hydroelectric projects, Volume 1. Current practices for instream flow needs, dissolved oxygen, and fish passage. DOE/ID-10360, U.S. Department of Energy, Idaho Field Office, Idaho Falls, ID.

Sene, K., Hunt, J., Thomas, N., 1994. The role of coherent structures in bubble transport by turbulent shear flows. J. Fluid Mech., 259, 219-240.

Shih, T-H., Liou, W.W., Shabbir, A., Yang, Z., Zhu, J., 1995. A new k-ϵ eddy viscosity model for high Reynolds number turbulent flows. Computers & Fluids 24, 227–238.

Souders, D.T., Hirt, C., 2004. Modeling entrainment of air at turbulent free surfaces. Proc. World Water and Environmental Resources Congress, pp. 1–10.

Stewart, C., 1995. Bubble interaction in low-viscosity liquids. Int. J. Multiphase Flow, 21(6), 1037-1046.

Straub, L.G., A. G. Anderson, 1958. Experiments on self-aerated flow in open channels. J. Hydraulics Div. ASCE, 84(7), 1-35.

Sun, S., Chanson, H., 2013. Characteristics of clustered particles in skimming flows on a stepped spillway. Environ. Fluid Mech., 13, 73-87.

Svendsen, I.A., Veeramony, J., Bakunin, J., Kirby, J., 2000. The flow in weak turbulent hydraulic jumps. J. Fluid Mech. 418, 25–57.

Taeibi-Rahni, M., Loth, E., Tryggvason, G., 1994. Flow modulation of a planar free shear layer with large bubbles – direct numerical simulations. Int. J. Multiphase Flow 20(6), 1109–1128.

Tamburrino, A., Gulliver, J.S., 2002. Free-surface turbulence and mass transfer in a channel flow. AIChE Journal, 48(12), 2732-2743.

Tennessee Valley Authority, n.d. 'Hydroelectric power'. Web. 3 Sept. 2014.

Tio, K.-K., Liñán, A., Lasheras, J.C., Gañán-Calvo, A.M., 1993. On the dynamics of buoyant and heavy particles in a periodic Stuart vortex flow. J. Fluid Mech., 254, 671-699.

Tomiyama, A., Sou, A., Minagawa, H., Sakaguchi, T., 1993. Numerical analysis of a single bubble by VOF method. JSME Int. J. Ser. B. 36, 51–56.

Tsivoglou, E.C., Wallace, J.R., 1972. Characterization of stream reaeration capacity. *U.S. EPA Report R3-72-012,* U.S. Environmental Protection Agency, Washington, D.C.

Urban, A.L., Hettiarachchi, S.L., Miller, K.F., Kincaid, G.P., Gulliver, J.S., 2001. Field experiments to determine gas transfer at gated sills. *J. Hydraulic Eng.,* 127(10), 848-859.

Urban, A., Gulliver, J., Johnson, D., 2008. Modeling total dissolved gas concentration downstream of spillways. J. Hydraulic Eng. 134, 550–561.

Wang, H., Chanson, H., 2013. Free-surface deformation and two-phase flow measurements in hydraulic jumps. Research Report No. CH91/13, University of Queensland, Australia.

Waniewski, T.A., Hunter, C., Brennen, C.E., 2001. Bubble measurements downstream of hydraulic jumps. Int. J. Multiphase Flow 27(7), 1271–1284.

Weber, L., Huang, H., Lai, Y., McCoy, A., 2004. Modeling total dissolved gas production and transport downstream of spillways: Three-dimensional development and applications. Int. J.River Basin Mgmt. 2, 157–167.

Wilhelms, S.C., Clark, L., Wallace, J.R., Smith, D.R., 1981. Gas transfer in hydraulic jumps. U.S. Army Engineer Waterways Experiment Station, Technical Report E-81-10, Vicksburg, Mississippi.

Wilhelms, S.C., 1988. Reaeration at low-head gated structures; preliminary results. Information Exchange Bulletin E-88-1, U.S. Army Corps of Engineers Waterways Experiment Station, Vicksburg, Mississippi.

Wilhelms, S.C., Gulliver, J.S., 2005. Gas transfer, cavitation and bulking in self-aerated spillway flow. J. Hydraulic Res. 43(5), 532-539.

Witt, A., Gulliver, J., Shen, L. 2014. Simulating air entrainment and vortex dynamics in a hydraulic jump. In review, Int. J. Multiphase Flow.

Zhang, G., Wang, H., Chanson, H., 2012. Turbulence and aeration in hydraulic jumps: free-surface fluctuation and integral turbulent scale measurements. Environ Fluid Mech. 13(2), 189-204.

Zhao, Q., Misra, S.K., Svendsen, I.A., Kirby, J.T. 2004. Numerical study of a turbulent hydraulic jump. Proc. 17th Eng. Mech. Div. Conf. ASCE, Newark, USA.

Zhu, J., Shih, T-H., 1994. Computation of confined coflow jets with 3 turbulence models. Int. J. Numer. Methods Fluids 19, 939–956.

Zidouni, K.F., Bousbia, S.A., Mataoui, A., 2010. Assessment of three turbulence model performances in predicting water jet flow plunging into a liquid pool. Nuclear Technology and Radiation Protection 25(1), 13–22.